UNIVERSITY OF CALIFORNIA SAN DIEGO

Transport and Electrodynamics of Electronic Condensates

A dissertation submitted in partial satisfaction of the
requirements for the degree
Doctor of Philosophy

in

Physics

by

Chao Xu

Committee in charge:

Professor Michael Fogler, Chair
Professor Leonid Butov
Professor Michael Galperin
Professor Congjun Wu
Professor Joel Yuen-Zhou

2021

The dissertation of Chao Xu is approved, and it is acceptable in quality and form for publication on microfilm and electronically.

University of California San Diego

2021

DEDICATION

To my parents.

TABLE OF CONTENTS

LIST OF FIGURES

ACKNOWLEDGEMENTS

I want to first thank Prof. Michael Fogler, my PhD advisor, who shows me how to be a great physicist. Misha can always explain physical problems intuitively with simple language, which also becomes my goal that one day I could also explain physical problems to others like him. Misha also provides me the access to the research related to actual experiments, which helps me to know how to communicate with experimentalists, which is definitely beneficial to my future academic career. Misha offers me RA position all the time, and I know this is not very common in a theoretical group, so I am very grateful for his support.

Secondly, I want to thank Prof. Congjun Wu. When I just came to UCSD, Prof. Wu offered a series of courses related to condensed matter physics, which is my first touch to this subject. At the first several years, I worked with Prof. Wu on unconventional superconductivity, and I have to say that it is a good practice for me to hands on real problems.

Then I want to thank Prof. Leonid Butov for letting me explain the beautiful experiment done in his group. The experiment gives me a platform to study realistic bosonic many-body systems, and I learned a lot from studying and explaining the experiments.

I also want to thank my fellow classmates. I discuss with Dr. Wang Yang for countless hours, and the discussion has not stopped even after his graduation. We discuss superconductivity, bosonization, Luttinger liquid, bethe ansatz, and etc. I am lucky that I can find someone like Wang who has similar interests as me, so we can discuss many different subjects. I want to thank Dr. Zhiyuan Sun as well for the time that he spent to explain his research to me. Hope Wang and Zhiyuan will find their ideal positions soon.

Chapter 1, in full, is a reprint with permission from 'C. Xu, J. Leonard, C. Dorow, L. Butov, M. Fogler, D. Nikonov, and I. Young, **Exciton gas transport through nanoconstrictions**. *Nano Lett.* **19**, 5373-5379 (2019)'. Copyright 2019 American Chemical Society. The dissertation author was the primary investigator and author of this paper.

Chapter 2, in part, contains material being prepared for submission for publication, 'C.

Xu and M. Fogler, **Nonlinear diffraction of Bose gas through single and multiple slits**'. The dissertation author was the primary investigator and author of this paper.

Chapter 3, in part, contains material being prepared for submission for publication, 'C. Xu and M. Fogler, **Hypernetted chain study of coupled exciton liquids in electron-hole quadrilayers**'. The dissertation author was the primary investigator and author of this paper.

Chapter 4 is a reprint of the following preprint being prepared for submission for publication: 'C. Xu, W. Yang, and C. Wu, **Superconducting junction with tri-component pairing gap functions**. *arXiv:2010.05362*'. The dissertation author was the primary investigator and author of this paper.

Chapter 5 is a reprint of the following preprint being prepared for submission for publication: 'C. Xu and W. Yang, **Axion electrodynamics in p+is superconductors**. *arXiv: 2009.12998*'. The dissertation author was the primary investigator and author of this paper.

VITA

2015	B. S. in Physics, University of Science and Technology of China
2015-2021	Graduate Teaching/Research Assistant, University of California San Diego
2021	Ph. D. in Physics, University of California San Diego

PUBLICATIONS

C. Xu, J. Wu, and C. Wu, **Quantized interlevel character in quantum systems**. *Phys. Rev. A* **97**, 032124 (2018).

C. Xu, J. R. Leonard, C. J. Dorow, L. V. Butov, M. M. Fogler, D. E. Nikonov, and I. A. Young, **Exciton gas transport through nanoconstrictions**. *Nano Lett.* **19**, 5373-5379 (2019).

W. Yang, C. Xu, and C. Wu, **Single branch of chiral Majorana modes from doubly degenerate Fermi surfaces**. *Phys. Rev. Research* **2**, 042047 (2020).

D. J. Choksy, C. Xu, M. M. Fogler, L. V. Butov, J. Norman, and A. C. Gossard, **Attractive and repulsive dipolar interaction in bilayers of indirect excitons**. *Phys. Rev. B* **103**, 045126 (2021).

C. Xu and W. Yang, **Axion electrodynamics in p+is superconductors**. *arXiv: 2009.12998*.

C. Xu, W. Yang, and C. Wu, **Superconducting junction with tri-component pairing gap functions**. *arXiv:2010.05362*.

C. Xu and M. Fogler, **Hypernetted chain study of coupled exciton liquids in electron-hole quadrilayers**. (paper in preparation)

C. Xu and M. Fogler, **Nonlinear diffraction of Bose Gas through single and multiple slits**. (paper in preparation)

C. Xu, J. Li, T. Abdelzaher, H. Ji, B.K. Szymanski, and J. Dellaverson **The paradox of information access: on modeling social-media-induced polarization**. *arXiv:2004.01106*.

T. Abdelzaher, H. Ji, J. Li, C. Yang, J. Dellaverson, L. Zhang, C. Xu, and B. Szymanski, **The paradox of information access: growing isolation in the age of sharing**, *arXiv:2004.01967*. (submitted to IEEE Computer)

ABSTRACT OF THE DISSERTATION

Transport and Electrodynamics of Electronic Condensates

by

Chao Xu

Doctor of Philosophy in Physics

University of California San Diego, 2021

Professor Michael Fogler, Chair

Superfluidity and superconductivity are similar and can be considered as the counterpart of each other in various systems. In this dissertation, I will examine my works on both superfluidity and superconductivity, which are two subjects that I mainly studied. The platform of bosonic systems that I worked on is indirect exciton, and as for superconductivity I mainly focused on the unconventional $p-$wave one.

Indirect excitons, or interlayer excitons are bound states of electrons and holes, where electrons and holes live in separate layers. Indirect excitons can interact with photon at infrared and visible wavelength. We first study the transport properties of one layer of exctions going through a single quantum point contact, and discuss the conductance behavior of such bosonic

quasiparticles, where we neglect the interaction between excitons. Then we include the interacting effect by the Gross-Pitaevskii equation, and study the non-linear diffraction and interference of interacting condensates, transporting through nanoconstrictions. Using the classical inverse scattering method, we can map the interference problem to a one dimensional scattering problem to solve the the interference pattern. Instead of the properties of one layer of excitons, we also study the properties of two layers of excitons, electron-hole quadrilayers. If two electron-hole bilayer is well separated, we can treat this quadrilayer system as two layers of excitons, that have dipolar interaction between each other. We calculate ground state energies, static structural factors, and collective modes (sound excitations) for various of densities of these two exciton layers. If the densities of excitons in two layers are equal (balanced), the system may evolve into a biexciton phase, where exciton pairs up with another exciton in another layer, when the density is dilute enough. In the limit of strong imbalance, we can treat the exciton in the dilute layer as a polaron interacting with sound modes of the other layer.

The $p-$wave superconducting pairing can be of two types, that are the counterparts of ^{3}He-A and ^{3}He-B phases. In a ^{3}He-A type superconductor, which is also referred as $p_x + ip_y$ (or simply $p+ip$) superconductor, the pairing is quasi two dimensional. We study a junction between a conventional $s-$wave superconductor and a $p+ip$ superconductor. Using Ginzburg-Landau free energy analysis, we can determine the symmetry breaking patterns of superconducting orders. In addition, we find that the symmetry breaking pattern at junction implies the existence of a magnetoelectric effect, and a finite spin polarization at the edge of the junction. If the ^{3}He-B type pairing and $s-$wave superconducting pairing coexist, they may prefer to have a $\pi/2$ phase difference, and it is called $p+is$ superconductor. We perform a systematic study of the electrodynamics in $p+is$ superconductors, where we calculate the effective action for the external fields, which proves to be similar to the axion action. We will show how to define the axion angle in a $p+is$ superconductor, and we point out some differences between our effective action and the axion action, which corresponds to the relativistic case.

Chapter 1

Exciton Gas Transport Through Nanoconstrictions

1.1 Introduction

Indirect excitons (IXs) in coupled quantum wells have emerged as a new platform for investigating quantum transport. The IXs have long lifetime, [1] long propagation distance, [2, 3, 4, 5, 6, 7, 8, 9] and long coherence length at temperatures T below the temperature T_0 of quantum degeneracy [Eq. (1.7)].blue [10] Although an IX is overall charge neutral, it can couple to an electric field via its static dipole moment ed, where d is the distance between the electron and hole layers [Fig. 1.1(a)]. These properties enable experimentalists to study transport of quasi-equilibrium IX systems subject to artificial potentials controlled by external electrodes [Fig. 1.1(b)].

In this chapter, we examine theoretically the transport of IXs through nano-constrictions [Fig. 1.1(c-e)]. [11] Historically, studies of transmission of particles through narrow constrictions have led to many important discoveries. In particular, investigations of electron transport through so called quantum-point contacts (QPCs) have revealed that at low T the conductance of smooth,

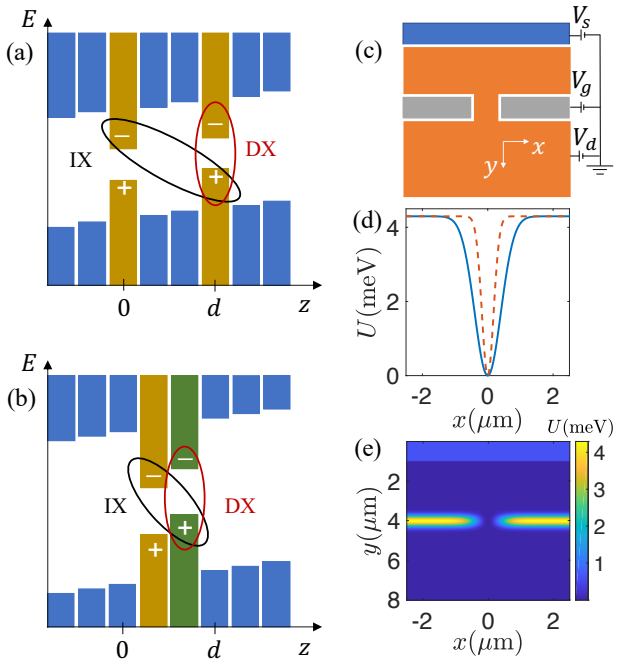

Figure 1.1: (a) Schematic energy band diagrams of an atomically thin electron-hole bilayer subject to an external electric field. The direct exciton (DX) is indicated by the red oval, the indirect exciton (IX) by the black one. The bars represent atomic planes. (b) Same as (a) for a spacer-free type II heterostructure. Various combinations of 2D materials can be used, examples include: for GaAs structures, GaAs (green), AlAs (yellow), AlGaAs (blue); for TMD type I structures, MoS_2 (yellow), hBN (blue); for TMD type II structures, WSe_2 (green), $MoSe_2$ (yellow), hBN (blue) (c) Schematic of an IX QPC device. Voltage V_s (V_d) controls the electrochemical potential of the source (drain); V_g creates a potential constraining IXs from the sides. (d) Variation of the IX potential along the line $y = y_0$ across the QPC for $a_x = 180$ and $400nm$ (dashed and solid trace, respectively) with other parameters as follows: $A = 4.30meV$, $C = 1$, $a_y = 200nm$, $U_{\mathrm{sd}} = 1.0meV$, $y_0 = 4.0\,\mu$m, $y_1 = 1.0\,\mu$m, see Eq. (1.1). (e) False color map of $U(x,y)$ for the larger a_x in (d) .

electrostatically defined QPCs exhibits step-like behavior as a function of their width. [12, 13] The steps appear in integer multiples of Ne^2/h (except for the anomalous first one [14]) because the electron spectrum in the constriction region is quantized into one-dimensional (1D) subbands [Fig. 1.2(e)]. Here N is the spin-valley degeneracy. Associated with such subbands are current density profiles analogous to the diffraction patterns of light passing through a narrow slit. These patterns have been observed by nanoimaging of the electron flow. [15] The conductance quantization has also been observed in another tunable fermionic system, a cold gas of ^{6}Li atoms. [16]

For the transport of bosonic IXs, we have in mind a conventional in solid-state physics setup where the QPC is connected to the source and drain reservoirs of unequal electrochemical potentials, ζ_s and ζ_d [Fig. 1.2(a-c)]. The difference $\zeta_s - \zeta_d > 0$ is analogous to the source-drain voltage in electronic devices. Whereas electrons are fermions, IXs behave as bosons. This makes our transport problem unlike the electronic one. The problem is also different from the slit diffraction of photons or other bosons, such as phonons, considered so far. Indeed, one cannot apply a source-drain voltage to photons or phonons in any usual sense. [However, quantized *heat* transport of phonons [17, 18, 19] has been studied.]

To highlight the qualitative features, we do our numerical calculations for the case where the drain side is empty, $\zeta_d = -\infty$. The conductance of the QPC can be described by the bosonic variant of the standard Landauer-Büttiker theory. [20] It predicts that the contribution of a given subband to the total conductance can exceed N/h if its Bose-Einstein occupation factor is larger than unity. [21] To the best of our knowledge, there have been no direct experimental probes of this prediction in bosonic systems. The closest related experiment is probably the study of ^{6}Li atoms passing through a QPC in the regime of enhanced attractive interaction. [22] That experiment has demonstrated the conductance exceeding N/h and the theory [23, 24, 25] has attributed this excess to the virtual pairing of fermionic atoms into bosonic molecules by quantum fluctuations.

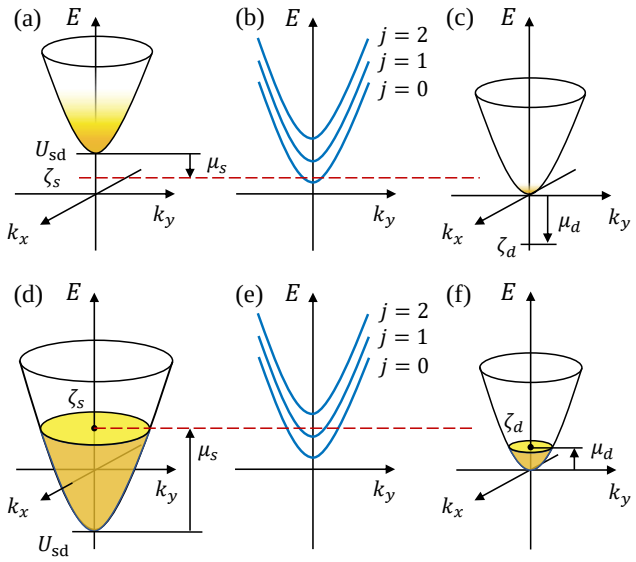

Figure 1.2: Energy spectra at the source (a, d), the QPC (b, e), and the drain (c, f). The electrochemical potential of the source is indicated by the horizontal dashed line. The shading represents the occupation factor. Panels (a-c) are for bosonic particles, such as IXs. Panels (d-f) are for fermions, e.g., electrons.

Below we present our theoretical results for the IX transport through single, double, and multiple QPCs. We ignore exciton-exciton interaction but comment on possible interaction effects at the end of the chapter.

1.2 Model of a QPC

In the absence of external fields, the IXs are free to move in a two-dimensional (2D) x–y plane. When an external electric field $E_z = E_z(x,y)$ is applied in the z-direction [Fig. 1.1(a)], an IX experiences the energy shift $U = -eE_z d$. This property makes it possible to create desired external potentials $U(x,y)$ acting on the IXs. To engineer a QPC, $U(x,y)$ needs to have a saddle-point shape. Such a potential can be created using a configuration of electrodes: a global bottom gate plus a few local gates on top of the device. As depicted in Fig. 1.1(b), two of such top electrodes (gray) can provide the lateral confinement and another two (blue and orange) can control the

potential at the source and the drain. More electrodes can be added if needed. Following previous work, [11] in our numerical simulations we use a simple model for $U(x,y)$:

$$\begin{aligned} U(x,y) = A\left(1 - Ce^{-x^2/2a_x^2}\right) e^{-(y-y_0)^2/2a_y^2} \\ + U_{\rm sd} f_F\left(\frac{y-y_1}{s}\right), \end{aligned} \tag{1.1}$$

where $f_F(x) = (e^x+1)^{-1}$ is the Fermi function. The width parameters a_x and a_y and the coefficients A and C on the first line of Eq. (1.1) are tunable by the gate voltage V_g [Fig. 1.1(b)]. The second line in Eq. (1.1) represents a gradual potential drop of magnitude $U_{\rm sd}$, central coordinate y_1, and a characteristic width s in the y-direction. These parameters are controlled by voltages V_s and V_d. Examples of $U(x,y)$ are shown in Fig. 1.1(c,d).

For qualitative discussions, we also consider the model of a quasi-1D channel of a long length L_c and a parabolic confining potential. The corresponding $U(x,y)$ is obtained by replacing the top line of Eq. (1.1) with

$$f_F\left(\frac{y_0 - L_c - y}{s}\right) f_F\left(\frac{y-y_0}{s}\right)\left(U_0 + \frac{1}{2}U_{xx}x^2\right), \tag{1.2}$$

where $U_{xx} = AC/a_x^2$. The energy subbands [Fig. 1.2(b)] in such a channel are

$$E_j(k_y) = U_0 + \hbar\omega_x\left(j + \frac{1}{2}\right) + \frac{\hbar^2 k_y^2}{2m}, \quad j = 0, 1, \ldots \tag{1.3}$$

The associated eigenstates are the products of the plane waves $e^{ik_y y}$ and the harmonic oscillator wavefunctions

$$\chi_j(x) = H_j\left(\sqrt{2}x/w_0\right)\exp\left(-x^2/w_0^2\right), \tag{1.4}$$

where $H_j(x)$ is the Hermite polynomial of degree j. The length w_0 and frequency ω_x are given by

$$w_0 = \sqrt{\frac{2\hbar}{m\omega_x}}, \quad \omega_x = \sqrt{\frac{U_{xx}}{m}}. \tag{1.5}$$

The subband energy spacing $\hbar\omega_x$ can be estimated as

$$\hbar\omega_x \simeq 8.8meV \left(\frac{m_0}{m}\right)^{1/2} \left(\frac{AC}{\text{meV}}\right)^{1/2} \left(\frac{\text{nm}}{a_x}\right), \tag{1.6}$$

which is approximately $0.1meV$ for devices made of transition metal dichalcogenides (TMDs), where exciton effective mass $m = 1.0m_0$ and $a_x = 180nm$. Hence, the onset of quantization occurs at $T \sim 1K$. The same characteristic energy scales in GaAs quantum well devices, [11] can be obtained in a wider QPC, $a_x = 400nm$, taking advantage of the lighter mass, $m = 0.2m_0$, cf. solid and dashed lines in Fig. 1.1(d). In both examples $\hbar\omega_x$ is much smaller than the IX binding energy ($\sim 300meV$ in TMDs [26] and $\sim 4meV$ in GaAs [27, 28]). Therefore, we consider the approximation ignoring internal dynamics of the IXs as they pass through the QPC [29] and treat them as point-like particles. Incidentally, we do not expect any significant reduction of the exciton binding energy due to many-body screening in the considered low-carrier-density regime in semiconductors with a sizable gap and no extrinsic doping. (At high carrier densities, the screening effect can be substantial.[30])

1.3 Conductance of a QPC

As with usual electronic devices, we imagine that our QPC is connected to semi-infinite source and drain leads (labeled by $l = s, d$). Inside the leads the IX potential energy $U(x,y)$ tends to asymptotic values U_l. Without loss of generality, we can take $U_d = 0$, as in Eq. (1.1). The difference $U_{\text{sd}} = U_s - U_d = \alpha(eV_s - eV_d)$ is a linear function of the control voltages V_s, V_d [Fig. 1.1(b)]. The coefficient of proportionality can be estimated as $\alpha \sim d/d_g$, where d_g is the

vertical distance between the top and bottom electrodes. The IX energy dispersions at the source and the drain are parabolic and are shifted by $U_{\rm sd}$ with respect to one another, see Fig. 1.2(a, c). In the experiment, the IX density of the reservoirs can be controlled by photoexcitation power. For example, the IX density n_s can be generated on the source side only, [11] while the drain side can be left practically empty, $n_d \ll n_s$. This is the case we focus on below. The chemical potentials μ_l are related to the densities n_l via [31, 32]

$$\mu_l = T \ln\left(1 - e^{-T_0/T}\right), \quad T_0 \equiv \frac{2\pi\hbar^2 n_l}{mN}. \tag{1.7}$$

Note that we count the chemical potentials from the minima of the appropriate energy spectra and that we use the units system $k_B \equiv 1$. In turn, the electrochemical potentials are given by

$$\zeta_l = \mu_l + U_l, \tag{1.8}$$

which implies

$$U_{\rm sd} = (\zeta_s - \zeta_d) - (\mu_s - \mu_d). \tag{1.9}$$

In the terminology of electron devices, the first term in Eq. (1.9) is related to the source-drain voltage $V_{\rm sd}$, viz., $\zeta_s - \zeta_d \equiv -eV_{\rm sd}$. The second term in Eq. (1.9) is referred to as the built-in potential, which is said to originate from charge redistribution in the leads.

If the particle densities n_l are fixed, variations of $\zeta_s - \zeta_d$ rigidly track those of $U_{\rm sd}$. The differential conductance can be computed by taking the derivative of the source-drain particle current I with respect to $U_{\rm sd}$:

$$G = (\partial I/\partial U_{\rm sd})_{n_s, n_d}. \tag{1.10}$$

G has dimension of $1/h$ and its natural quantum unit is N/h. (The spin-valley degeneracy is $N = 4$ in both TMDs and GaAs.)

For the long-channel model [Eq. (1.2)], G can be calculated analytically because the

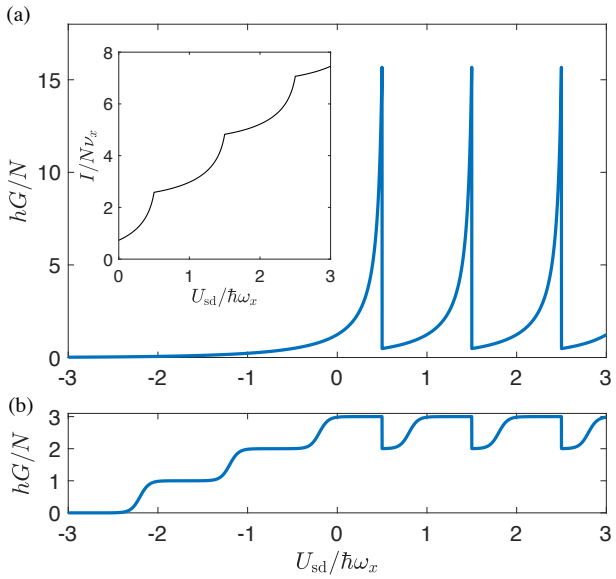

Figure 1.3: (a) Conductance of a bosonic QPC vs. $U_{\rm sd}$ from the adiabatic approximation [Eq. (1.12)] for $T = 0.8\hbar\omega_x$, $\mu_s = -0.05\hbar\omega_x$. Inset: total current as a function of $U_{\rm sd}$. The notation used on the y-axis is $\nu_x \equiv \omega_x/2\pi$. (b) Conductance of a fermionic QPC for $T = 0.05\hbar\omega_x$, $\mu_s = 2.7\hbar\omega_x$. Note that the number of conductance steps occurring at $U_{\rm sd} < E_0^0 = \frac{1}{2}\hbar\omega_x$ is equal to $\mu_s/\hbar\omega_x$ rounded up to the nearest integer.

single-particle transmission coefficients through the QPC have the form $t_j(E) = \theta\big(E - E_j^0\big)$, i.e., they take values of either 0 or 1. Here $E_j^0 \equiv E_j(0)$ and $\theta(x)$ is the Heaviside step-function. Adopting the standard Landauer-Büttiker theory for fermions [20] to the present case of bosons (see also [21]), we find the total current to be $I = \sum_j (I_{s,j} - I_{d,j})$ where the partial currents are

$$I_{a,j} = \frac{N}{h}\int_{U_a}^{\infty} f_B\left(\frac{E-\zeta_a}{T}\right) t_j(E)\,dE \tag{1.11}$$

and $f_B(x) = (e^x - 1)^{-1}$ is the Bose function. In turn, the conductance is

$$G = \frac{N}{h}\sum_j \theta\big(E_j^0 - U_{\rm sd}\big) f_B\left(\frac{E_j^0 - U_{\rm sd} - \mu_s}{T}\right). \tag{1.12}$$

The dependence of G on $U_{\rm sd}$ is illustrated in Fig. 1.3(a). The conductance exhibits asymmetric peaks. Each peak signals the activation of a new conduction channel whenever $U_{\rm sd}$

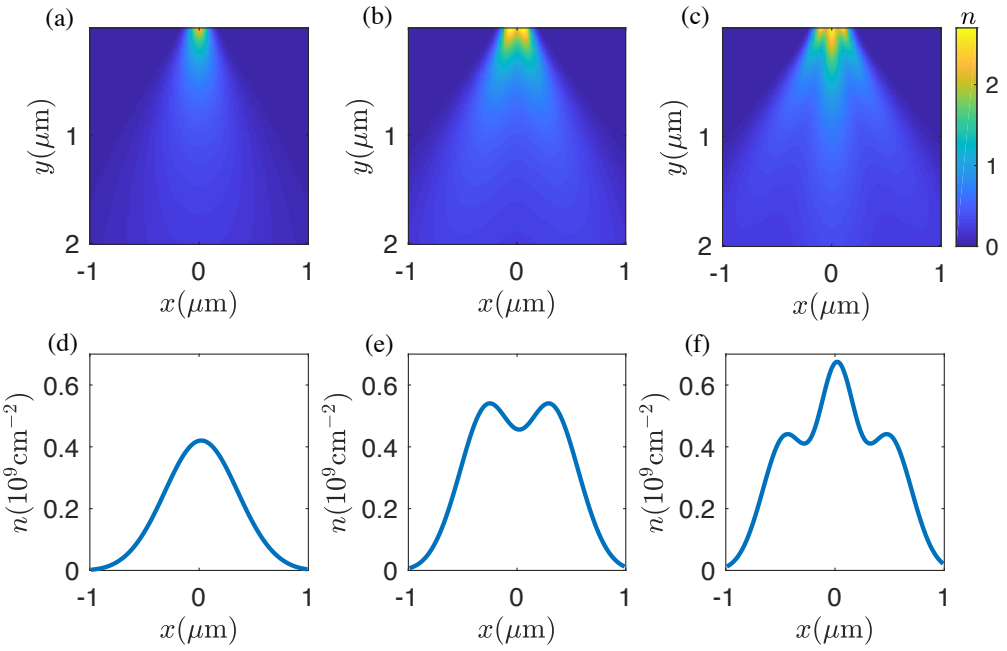

Figure 1.4: The IX density distribution in a QPC for three different U_{sd}. Panels (a-c) depict the density distribution n in the x–y plane in units of $10^9 cm^{-2}$. Panels (d-f) show the profiles of n along the midline, $y = 1\,\mu$m, of the region plotted directly above. Values of U_{sd} are adjusted to highlight the contributions of particular subbands: (a, d) $j = 0$ for $U_{\mathrm{sd}} = 0.52$, (b, e) $j = 1$ for $U_{\mathrm{sd}} = 1.52$, (c, f) $j = 2$ for $U_{\mathrm{sd}} = 2.52$, all in units of $\hbar\omega_x = 0.10meV$; $T = 1.0K$ everywhere.

approaches the bottom of a particular 1D subband. All the peaks have the same shape, which is the mirror-reflected Bose function with a sharp cutoff. As T decreases, the width of the peaks $\Delta \sim \min(T, -\mu_s)$ decreases. The magnitude of the peaks $G_{\max} = (N/h) f_B(-\mu_s/T)$ can be presented in the form

$$G_{\max} = \frac{N}{h} f_{\max}\,, \tag{1.13}$$

where $f_{\max}$ is the occupation of the lowest energy state at the source. For fermions, $f_{\max}$ is limited by 1. For 2D bosons, $f_{\max} = e^{T_0/T} - 1$ exceeds 1 and, in turn, $G_{\max}$ exceeds N/h at $T < T_0/\ln 2$.

The sudden drops of G at $U_{\mathrm{sd}} = E_j^0$ [Fig. 1.3(a)] occur because the current carried by each subband saturates as soon as it becomes accessible to all the IXs injected from the source, down to the lowest energy U_{sd}. These constant terms do not affect the differential conductance G. The total current as a function of U_{sd} is plotted in the inset of of Fig. 1.3(a).

It is again instructive to compare these results with the more familiar ones for fermions, which are obtained replacing the Bose function f_B with the Fermi function f_F in Eq. (1.12). In the regime where $U_{\rm sd}$ is large and negative, the Heaviside functions in Eq. (1.12) play no role, so that G traces the expected quantized staircase shown in Fig. 1.3(b). The conductance steps occur whenever $U_{\rm sd} = E_j^0 - \mu_s$. Once $U_{\rm sd}$ approaches $E_0^0 = \hbar\omega_x/2$, a different behavior is found: the conductance displays additional sudden drops at $U_{\rm sd} = E_j^0$, which causes it to oscillate between two quantized values. These drops appear for the same reason as in the bosonic case: current saturation for each subband that satisfies the condition $E_j^0 < U_{\rm sd}$.

The adiabatic QPC model considered above is often a good approximation [13, 12] for more realistic models, such as Eq. (1.1). The latter cannot be treated analytically but we were able to compute G numerically, using the transfer matrix method [33] (see below). The results are presented in the Supporting Information. The main difference from the adiabatic case is that the conductance peaks are reduced in magnitude and broadened.

1.4 Density distribution in a QPC

In analogy to experiments with electronic QPCs, [15] it would be interesting to study quantized conduction channels by optical imaging of IX flow. Unlike electrons, IXs can recombine and emit light, so that the IX photoluminescence can be used for measuring their current paths. This motivates us to model the density distribution $n(x,y)$ of IXs in the QPC. We begin with analytical considerations and then present our numerical results, Fig. 1.4.

The calculation of the $n(x,y)$ involves two steps. First, we solve the Schrödinger equation for the single-particle energies $E = \hbar^2 k'^2/(2m)$ and the wavefunctions $\psi(x,y)$ of IXs subject to the potential $U(x,y)$. The boundary conditions for the $\psi(x,y)$ is to approach linear combinations of plane waves of momenta $\mathbf{k}' = (k'_x, \pm k'_y)$ at $y \to -\infty$ but contain no waves of momenta $\mathbf{k}'' = (k''_x, k''_y)$ with $\mathrm{Re}\, k''_y < 0$ at $y \to +\infty$. Such states correspond to waves incident from the source. Second, we

sum the products $f_B(E-\zeta_s)|\psi(x,y)|^2$ to obtain the $n(x,y)$. We choose not to multiply the result by N, so that our $n(x,y)$ is the IX density per spin per valley.

For a qualitative discussion, let us concentrate on the simplest case of large k_y', i.e., fast particles. As the incident wave propagates from the source lead, it first meets the smooth potential drop $U_{\rm sd}$ at $y=y_1$. Assuming $k_y's \gg 1$, the over-the-barrier reflection at $y=y_1$ can be neglected. Therefore, the y-momentum increases to the value k_y dictated by the energy conservation,

$$k_y^2 = k_y'^2 + (2m/\hbar^2)U_{\rm sd}\,, \tag{1.14}$$

while the x-momentum k_x' remains the same. Subsequently, the incident wave impinges on the QPC at $y=y_0$. Typically, this causes a strong reflection back to the source. However, certain eigenstates have a nonnegligible transmission. After passing the QPC, their wavefunctions expand laterally with the characteristic angular divergence of $1/(k_y w_0) \ll 1$. Such wavefunctions can be factorized $\psi(x,y) = e^{ik_y y}\chi(x,y)$, where the slowly varying amplitude $\chi(x,y)$ obeys the eikonal (or paraxial) equation

$$\left(-i\hbar v_y \partial_y - \frac{\hbar^2}{2m}\partial_x^2 + U\right)\chi = 0\,, \quad v_y \equiv \frac{\hbar k_y}{m}\,. \tag{1.15}$$

If the model of the long constriction [Eq. (1.2)] is a good approximation, the solution is as follows. Inside the QPC, $\chi(\mathbf{r})$ is proportional to a particular oscillator wavefunction $\chi_j(x)$ [Eq. (1.4)]. Outside the QPC, it behaves as a Hermite-Gaussian beam whose probability density can be written in the scaling form

$$|\chi(x,y)|^2 = \frac{1}{b(y)}\chi_j^2\left(\frac{x}{b(y)}\right), \tag{1.16}$$

$$b(y) = \sqrt{1+\frac{(y-y_0)^2}{w_y^2}}\,, \tag{1.17}$$

$$w_y = \frac{1}{2}k_y w_0^2\,. \tag{1.18}$$

This representation has been used in the study of a Bose-Einstein condensate (BEC) expansion from a harmonic trap. [34, 35] Our problem of the steady-state 2D transport through the QPC maps to the noninteracting limit of this problem in $1+1$D, with $t=(y-y_0)/v_y$ playing the role of time. In other words, the IX current emerging from the QPC is mathematically similar to a freely expanding BEC. This mapping is accurate if the characteristic width of the energy distribution of the IX injected into the QPC from the source is small enough, $\Delta \ll \hbar\omega$. Dimensionless function $b(y)$ has the meaning of the expansion factor. A salient feature of the eigenfunctions are the nodal lines $\chi(x,y)=0$. The lowest subband $j=0$ has no such lines whereas the higher subbands have exactly $j=1,2,\ldots$ of them.

For a quantitative modeling, we carried out simulations using the transfer matrix [33] method. This method gives a numerical solution of the Schrödinger equation discretized on a finite-size real-space grid for a given energy E and the boundary conditions described above. To obtain the total particle density, we summed the contributions of individual states, making sure to include enough E's to achieve convergence. In all our calculations the chemical potential μ_s was fixed to produce the density (per spin per valley) $n_s = 1.0\times 10^{10} cm^{-2}$ at the source. Examples of such calculations for temperature $T = 1.0K$ are shown in Fig. 1.4. Since the partial densities $|\psi(x,y)|^2$ are weighted with the Bose-Einstein factor $f_B(E-\zeta_s)$, the lowest-energy $j=0$ subband typically dominates the total density, making it look like a nodeless Gaussian beam [Fig. 1.4(a,d)]. However, if $U_{\rm sd}$ is tuned slightly above the bottom of the $j=1$ subband, the contribution of this subband is greatly enhanced by the van Hove singularity of the 1D density of states $N/(\pi\hbar v_y) \propto \left(E-E_j^0\right)^{-1/2}$ inside the QPC. As a result, $n(x,y)$ develops a valley line (local minimum) at $x=0$, which is the nodal line of function $\chi_1(x/b,y)$ [Fig. 1.4(b,e)]. A similar phenomenon occurs when we tune $U_{\rm sd}$ to slightly above the bottom of $j=2$ subband. Here the density exhibits two valley lines, which approximately follow the nodal lines of function $\chi_2(x/b,y)$ [Fig. 1.4(c,f)]. These theoretical predictions may be tested by imaging IX emission with high enough optical resolution. Note that these van Hove singularities do not enhance the

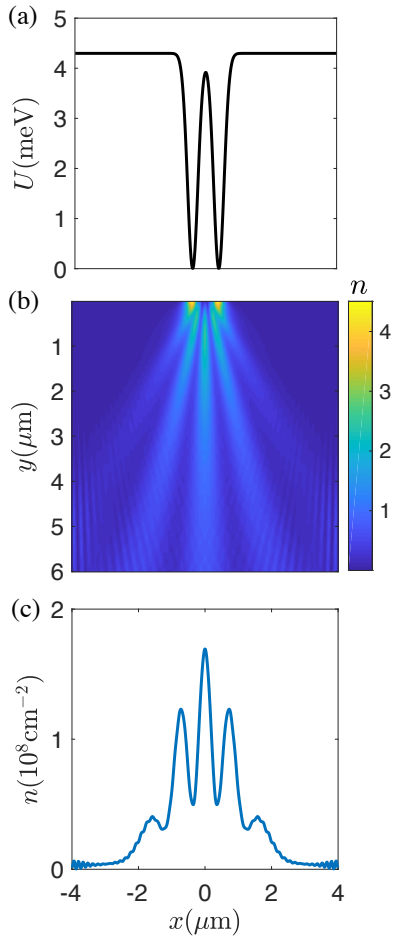

Figure 1.5: Double-QPC IX device. (a) The profile of the IX potential across the two constrictions. (b) The IX density in units of $10^8\,\mathrm{cm}^{-2}$. (c) The IX density along the line $y = 2\,\mu$m in (b). The ripples at the flanks of the fringes are finite-size artifacts.

differential conductivity G because of the cancellation between the density of states and the particle velocity v_y. As explained above, this leads to current saturation and thus negligible contribution of jth subband to G at $U_{\mathrm{sd}} > E_j^0$.

1.5 Double and multiple QPC devices

We have next explored the exciton analog of the Young double-slit interference. A short distance downstream from the first QPC ($1.0\,\mu$m along y), we added another potential barrier

constructed from two copies of the single-QPC potential [Eq. (1.1)] shifted laterally in x. As in Young's classical setup, the first QPC plays the role of a coherent source for the double-QPC. An example of the latter with the center-to-center separation of $800nm$ is shown in Fig. 1.5(a). We computed the IX density distribution in this system for $U_{\rm sd}$ at which the IXs fluxes through all the QPCs are dominated by the $j = 0$ subband. The IXs transmitted through the double-QPC create distinct interference fringes, Fig. 1.5(b,c).

Finally, we considered a four-QPC array. To show the results more clearly, we simulated the zero-temperature limit, where a single energy E contributes. As illustrated by Fig. 1.6(a), the interference pattern begins to resemble that of a diffraction grating. Near the QPCs, it exhibits the periodic refocusing known as the Talbot effect. The repeat distance for the complete refocusing is [36]

$$y_T = \frac{\lambda}{1 - \sqrt{1 - \frac{\lambda^2}{a^2}}}, \tag{1.19}$$

where $\lambda = 2\pi/k_y$ is the de Broglie wavelength of the IXs and a is the distance between the QPCs. For $\lambda = 100nm$ and $a = 1000nm$, this distance $y_T \simeq 20\,\mu$m is beyond the range plotted in Fig. 1.6(a). Therefore, only the so-called fractional Talbot effect is seen in that Figure. Although too fine for conventional imaging, these features may in principle be resolved by near-field optical techniques. Note that for a grating with N_s slits the crossover to the far-field diffraction occurs at the distance $\sim N_s y_T$, which is prohibitively large for the transfer matrix simulations. For a qualitative illustration of this crossover, we computed the interference pattern simply by adding a number of Gaussian beams, see Fig. 1.6(b,c).

1.6 Discussion and outlook

In this chapter, we considered a few prototypical examples of mesoscopic IX phenomena. We analyzed the subband quantization of IX transport through a single QPC, the double-slit interference from two QPCs, and the Talbot effect in multiple QPCs. As for electrons, these

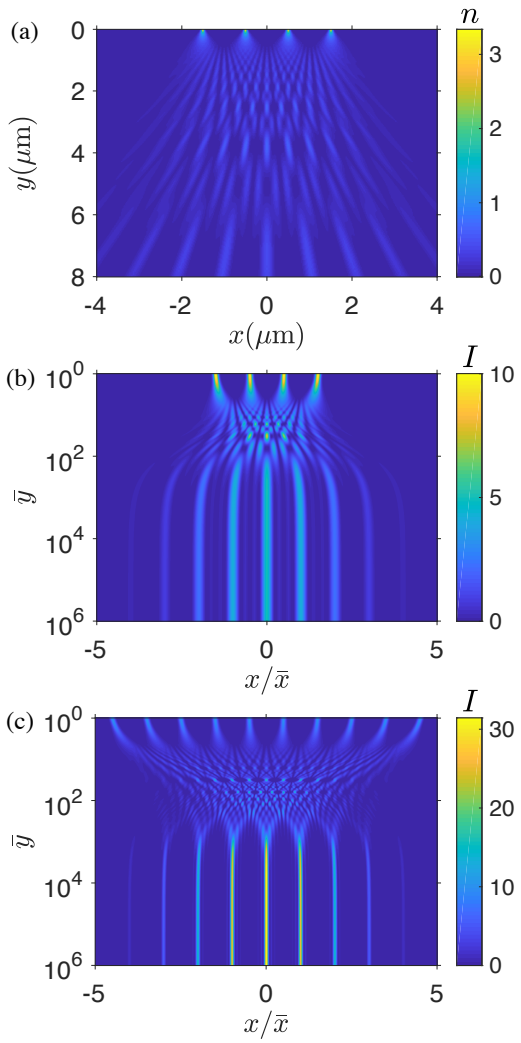

Figure 1.6: False color maps illustrating IX density in multiple QPC systems. (a) Talbot-like interference in a four-QPC device. The incident beam consists of a single plane wave, corresponding to the $T = 0$ limit. $U_{\mathrm{sd}} = 0.10meV$. (b) Rescaled intensity $I \equiv |\psi(\mathrm{r})|^2 \bar{x}$ of the interference pattern of $N_s = 4$ Gaussian beams. Following an example in the literature, [37] the horizontal axis is normalized by $\bar{x} = (\lambda y/a) + a$ with $a = 1\,\mu$m. The vertical axis represents $\bar{y} = (y/w_y) + 1$. (c) Same as (b) for $N_s = 10$.

phenomena should be experimentally observable at low enough temperatures. The present theory may be straightforwardly expanded to more complicated potential landscapes and structures.

In the present work we neglected IX interactions. This interaction is dipolar, which in 2D is classified as short-range, parametrized by a certain interaction constant g. As mentioned above, the problem of the IX transport through a QPC is closely related to the problem of a BEC expansion from a harmonic trap. Following the studies of the latter, [34] interaction can be included at the mean-field level by using the Gross-Pitaevskii equation instead of the Schrödinger one. For the single-QPC case, we expect the GPE solution to show a faster lateral expansion of the exciton "jet", i.e., a more rapid growth of function $b(y)$. For the double- and multi-QPC cases, we expect repulsive interaction to suppress the interference fringes, similar to what is observed in experiments with cold atoms. [38] The lineshape and amplitude (visibility) of the fringes remain to be investigated.

Applications of our theory to real semiconductor systems would also require taking into account spin and valley degrees of freedom of IXs. It would be interesting to study spin transport of IXs [5, 10, 9] through nano-constrictions and associated spin textures. This could be an alternative pathway to probing spin conductance of quasi-1D channels. [39]

The field of mesoscopic exciton systems is currently in its infancy but it is positioned to grow, extending the phenomena studied in voltage-controllable electron systems to bosons. More importantly, it has the potential to reveal brand new phenomena. There are many intriguing subjects for future work.

This chapter, in full, is a reprint with permission from 'C. Xu, J. Leonard, C. Dorow, L. Butov, M. Fogler, D. Nikonov, and I. Young, **Exciton gas transport through nanoconstrictions**. *Nano Lett.* **19**, 5373-5379 (2019)' [40]. The dissertation author was the primary investigator and author of this paper.

Chapter 2

Nonlinear Diffraction of a Bose Gas through Single and Multiple Slits

2.1 Introduction

The ballistic transport of variety of particles (photons, phonons, electrons, atoms, and etc.) through quantum point contact or narrow constrictions has been studied both theoretically and experimentally to investigate the quantum effects of transport. As for 2D electronic systems, due to the narrow constriction, the spectrum inside the constriction is effectively 1D and quantized into subbands, so that there is a quantization of conductance for ballistic electronic system when the temperature is low enough. The conductance is step like with integer multiple of Ne^2/h as a function of the background chemical potential or the width of the constriction [12, 13], where N is the degeneracy of the electrons (spin and valley). The outgoing density patterns of diffraction from a constriction are also associated with quantization conductance [41], and with the help of nanoimaging technique, these patterns of electron can be experimentally observed [15]. Not only the electronic system, the quantization of conductance through quantum point contact is also observed in other fermionic systems such as neutral ^{6}Li atoms [16].

The transport of bosonic particles through narrow constrictions has also been studied such as heat transport [17, 18, 19]. Different from fermionic systems, the conductance of bosonic particles through a quantum point contact can exceed the limit of N/h [21, 40], due to the nature of occupation distribution for bosonic particles, predicted by Landauer-Büttiker theory [20]. 2D bosonic systems for quasi-particles such as indirect excitons (IXs) emerges as a platform for studying bosonic quantum transport. Due to its long life-time [1], long coherence length [10], and high mobility [2, 3, 4, 5, 6, 7, 8, 9], IX approaches the ballistic regime in the excitonic devices, where the quasi-particles' scattering dominates other than the background disorder. IX is coupled to the external electric field, due to its dipole moment, and the recent experiment [11] of the split-gate devices for IXs in the coupled double quantum wells demonstrates the setup of quantum point contact for IXs.

It has been shown that at the ballistic regime, the conductance of electronic systems through constrictions does not heavily affected by the interaction between particles, however the interaction effects may become considerable at non-ballistic systems (e.g. viscosity dominant regime). In our previous works, we have studied the transport of IXs at its diffusive [11] and the ideal Bose gas limits [40]. In this chapter, we will mainly focus on the interacting effect to the transport and dynamics of bosonic particles through constrictions at mean-field level.

Since the realizations of alkali cold atoms BEC [42, 43, 44], Gross-Pitaevskii Equation (GPE) [45, 46] has been used to study static properties of such systems, when the interaction is short-range (the scattering length much smaller than particle average distance) as a mean-field treatment. GPE can be also applied to study the dynamics of condensates such as when the external potential is time-dependent or quench process. [34, 35, 47, 48]. Since IXs have a effective short-range dipole-dipole interaction, GPE should be capable to describe such a system at low enough temperature. Similar formalism also appears in other systems such as non-linear optics, cold-atoms, polaritons, optical lattices, and etc. Particularly in 1D, GPE is integrable and associated with the inverse scattering transform (IST) method [49, 50]. Although the time

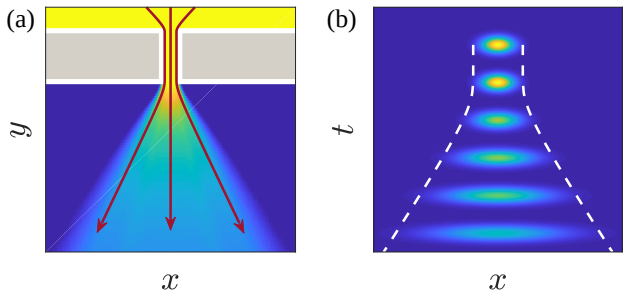

Figure 2.1: figures (a) and (b) demonstrate two possible setups of laterally expanding condensate. (a) shows the setup that the 2D condensate is constricted in a long but narrow channel in x-direction, so approximately the expansion only happens in x-direction as indicated by the two white arrows. (b) demonstrates another setup that the condensate is initially moving fast in a narrow channel, and then suddenly runs into the area without constriction, so that the condensate will continue to propagate and expands laterally at the same time. In such a setup y/v_y plays the role of time.

evolution of the system is hard to obtain, IST method allows us to study the long time behavior [51, 52, 53, 54, 55] (self-similar asymptotic solution) for certain setups [51, 56].

In this chapter we will mainly discuss the nonlinear effects to the diffraction from a slit and the interference from multiple slits. Related problems have been discussed before, and we will discuss these problems in more details analytically and numerically. The schematic plot of the setup are shown in Fig. 2.1 (b), where the white arrows indicate the follow of the condensate out from a constriction. At the paraxial limit, that is when the velocity of the propagation (v_y) is large, the direction of the propagation behaves like time coordinate (time of flight: y/v_y), so that it shares the same formalism with a 1D laterally expanding problem as demonstrated in Fig. 2.1 (a). The arrangement of this chapter is as following. First we will discuss the diffraction from a single slit of a condensate (1D laterally expansion of a condensate) for non-interacting and strongly interacting limits in section 2.2. These results will be reexamined by using the IST in section 2.3, and the condensate expansion for intermediate interacting strength will also be discussed. With the help of IST, we can also study interacting effects to the double slits interference analytically, where the corresponding physics coincides with Fabry-Pérot interferometry. The multiple slits interference will also be discussed. The corresponding 1D problems would be the interference

between two laterally expanding condensates or multiple condensates, which are also similar to the setup of a sudden released potential in optical lattice system.

2.2 Single constriction expansion in 1D

In this section we will study the diffraction of a condensate running out from a single slit with a high velocity of propagation v_y as shown in Fig. 2.1 (b). At the paraxial limit, this diffraction problem is an effectively 1D problem, where $y-$direction behaves as the time coordinate ($t = y/v_y$). The corresponding 1D dynamical problem is that the condensate is initially constricted to a single quantum well trap in 1D and then trap is released, so that the condensate starts to expand as time evolves (as the condensate propagates in $y-$direction). To describe such a system, we use GPE:

$$i\hbar\,\partial_t u = -\frac{\hbar^2}{2m}\,\partial_x^2 u + V(x,t)\,u + g|u|^2\,u\,, \tag{2.1}$$

where u is the condensate order parameter and g indicates the onsite interaction strength. As described before, $V(x,t) = m\omega^2(t)x^2/2$, where $\omega(t) = \omega_0$ when $t \leq 0$, and $\omega(t) = 0$ when the trap is released ($t > 0$). The paraxial limit is then taken as $\frac{m}{2}v_y^2 \gg \hbar\omega_0$. An illustration of the dynamics of such process is shown in Fig. 2.2, in which $L_0 = \sqrt{\hbar/m\omega_0}$ is defined from the natural length scale of a harmonic trap. The right column of the figures in Fig. 2.2 show the expansion of the interacting condensate while the left ones show the non-interacting cases, and one can directly observe that the interacting condensate expands more rapidly. The lower row of figures demonstrate the expansion of first excited mode from a trap which can be initially prepared by phase imprinting technique [57].

In certain limits, the expansion of the condensate from a trap can be exactly solved. If the condensate is nearly non-interacting, the dynamics of the condensate is identical to a Gaussian beam, such that at time zero, the density profile $n(x,0) = |u(x,0)|^2$ is a Hermitian Gaussian, and

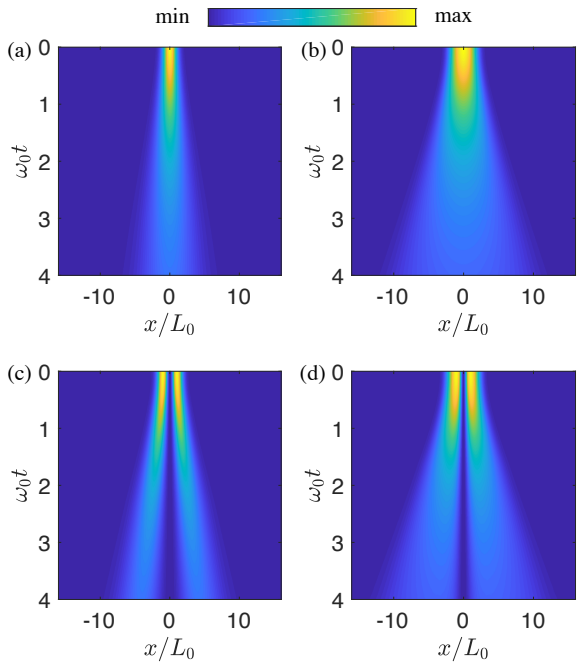

Figure 2.2: numerical simulation of density evolution of expanding condensates. (a) and (c) show the expansion of the non-interacting condensate with different initial static state at time zero, where initial state in (a) is the ground state in the trap, while the initial state in (c) is the first excited one (with a dark soliton in the middle). Similarly (b) and (d) demonstrate the expansion of interacting condensate for taking ground state and first excited state in a trap as initial state respectively.

it remains self similar afterwards. At any time $t > 0$,

$$n(x,t) = \frac{1}{b(t)} n(x/b(t),0)\,, \tag{2.2}$$

with

$$b(t) = \sqrt{1+\omega_0^2 t^2}\,, \tag{2.3}$$

where $b(t)$ is introduced as a dimensionless scaling factor that tells how the wave-function will scale with time. Different from the free expansion in 2D [34], in the case of 1D expansion, the scaling factor b for the interacting case is different from non-interacting one. The strength of the interaction can be measured by $\gamma = gn_0/\hbar\omega$, with n_0 being the central density in the harmonic trap. In the strongly interacting limit ($\gamma \gg 1$), we can use hydrodynamical equations to describe the dynamics of the condensate, by treating the interacting condensate as a compressible fluid with adiabatic index $C_p/C_v = 2$:

$$\partial_x(nv) + \partial_t n = 0\,; \tag{2.4}$$

$$\partial_t(nv) + \partial_x(\frac{1}{2}nv^2 + gn^2/2m) = 0\,, \tag{2.5}$$

which are continuity and Euler equations respectively. Assuming the the density profile is also self similar as shown in Eq.(2.2) for the strongly interacting case, the local velocity

$$v = x\frac{\partial_t b}{b} \tag{2.6}$$

can be obtained from the continuity equation. Insert this equation of velocity into the Euler equation, we obtain the equation of motion of $b(t)$

$$x\frac{\partial_t^2 b}{b} + \frac{g}{b^2 m}\partial_x n(x/b,0) = 0\,. \tag{2.7}$$

When the condensate is strongly interacting ($\gamma \gg 1$), using the Thomas-Fermi approximation, $\partial_x(n(x,0)) = xm\omega_0^2/g$, so that

$$\partial_t^2 b = \omega_0^2 b^3 \tag{2.8}$$

for the free expansion of strongly interacting condensate released from a harmonic trap. The boundary condition of $b(t)$ requires $b(t) = 1$ when $t \leq 0$, then the solution of b is

$$t_{\mathrm{SI}} = \frac{1}{\sqrt{2}\omega_0}\{\sqrt{b}\sqrt{b-1} + \ln(\sqrt{b} + \sqrt{b-1})\}, \tag{2.9}$$

while

$$t_{\mathrm{NI}} = \frac{1}{\omega_0}\sqrt{b^2-1}, \tag{2.10}$$

where SI and NI indicates strongly interacting and non-interacting respectively. Asymptotically $b(t)$ tends to be linear in time t, and $b(t) \sim \omega_0 t$ for the non-interacting case while $b(t) \sim \sqrt{2}\omega_0 t$ for the strongly interacting case.

Another case can be exactly solved is the case that the system is initially in a harmonic external potential as before, and then system suddenly change into a different harmonic trap. Here we will examine the case that the system suddenly change into a wider harmonic trap, that is $\omega(t) = \omega_1 < \omega_0$ when $t \geq 0$ as an example. As expected, the system will "breath" with certain amplitude and period, which are affected by the interaction unlike the case in 2D expansion. Starting from $t = 0$ the system will expand firstly, so that $b(t)$ will increase at beginning, then reaches it maximum, and the solutions of the maximum of b are

$$b_{\mathrm{max,NI}} = \omega_0/\omega_1 \tag{2.11}$$

$$b_{\mathrm{max,SI}} = \sqrt{1/4 + 2\omega_0^2/\omega_1^2} - 1/2\,. \tag{2.12}$$

When there is no interaction, the period of such an oscillation is $\Lambda_{\mathrm{NI}} = \pi/\omega_1$, while in the strongly

interacting regime, the period becomes

$$\Lambda_{\mathrm{SI}} = 2 \int_{1}^{b_{\max,\mathrm{SI}}} \frac{db}{\sqrt{2\omega_0^2 + \omega_1^2 - 2\omega_0^2/b + \omega_1^2 b^2}} \tag{2.13}$$

(All the details can be found in the Appendix).

2.3 Inverse scattering method and the interference between condensates

In this section we will study the problem of 1D expansion by the inverse scattering theory (IST), which allow us to study not only the single constriction expansion, but also the interference of double-constriction expansion. We need to write GPE in a dimensionless coordinates to take IST and numerical simulation. To write GPE in dimensionless coordinates (ξ and η), an extra parameter L with a dimension of length is introduced, then x and t are substituted by $\xi = x/L$ and $\eta = t/(mL^2/\hbar)$. Since we are studying the expansion from a harmonic trap, L is taken as $L = L_0$ for the following of the this article. After the substitution, the GPE becomes

$$i\,\partial_\eta u = -\frac{1}{2}\,\partial_\xi^2 u + \tilde{g}|u|^2 u\,, \tag{2.14}$$

with $\tilde{g}$ being $g/(\hbar^2/mL^2)$, so that $\tilde{g}|u|^2$ is dimensionless. The inverse problem of GPE is a Dirac scattering problem of an auxiliary field $\phi(\xi,\eta)$:

$$\hat{L}\begin{pmatrix}\phi_1\\ \phi_2\end{pmatrix} = \begin{bmatrix} i\partial_\xi & \sqrt{\tilde{g}}u \\ \sqrt{\tilde{g}}u^* & -i\partial_\xi \end{bmatrix}\begin{pmatrix}\phi_1\\ \phi_2\end{pmatrix} = \frac{\lambda}{2}\begin{pmatrix}\phi_1\\ \phi_2\end{pmatrix}, \tag{2.15}$$

with λ as an eigenvalue that is time independent. The boundary conditions for ϕ field are set to be $\phi_1(\xi) = e^{i\lambda\xi/2}$; $\phi_2(\xi) = R(\lambda)e^{-i\lambda\xi/2}$ as $\xi \to -\infty$, whereas $\phi_1(\xi) = T(\lambda)e^{i\lambda\xi/2}$; $\phi_2 = 0$ as

$\xi \to \infty$. There is also an equivalent Schrödinger equation for the auxiliary field, which reads $-\partial_\xi^2\psi + U\psi = \frac{\lambda^2}{4}\psi$, with $\psi = \phi_1 - i\phi_2$ and $U = \tilde{g}|u|^2 - \sqrt{\tilde{g}}\partial_\xi u$, which is known as Riccati equation.

The inverse scattering method allow us to connect the scattering spectrum of the auxiliary field and the asymptotic ($\eta \to \infty$) density distribution as

$$u(\xi,\eta) = \sqrt{\frac{2}{\tilde{g}\eta}}\alpha(\lambda)\exp\{i\lambda^2\eta/2 - i2|\alpha(\lambda)|^2\ln\eta\}\,, \tag{2.16}$$

in which $\lambda = \xi/\eta = x/t \cdot mL/\hbar$, and

$$|\alpha(\lambda)|^2 = -\frac{1}{4\pi}\ln|T(\lambda)|^2\,. \tag{2.17}$$

Except the exactly solvable Dirac potentials', the transmission spectrum $t(\lambda)$ for a general λ and a general u is hard to obtain, but the the scattering for zero-momentum ($\lambda = 0$) and u with constant phase factor (the velocity field is zero) can be exactly obtained. To solve for the transmission coefficient at zero momentum, one can rewrite the Dirac equation in Eq. (2.15) as (here we take $u = u(0,\xi)$ to be uniform in phase, so we take it as real for simplicity)

$$i\partial_\xi \begin{pmatrix}\phi_1\\ \phi_2\end{pmatrix} = \begin{bmatrix} & -\sqrt{\tilde{g}}u\\ \sqrt{\tilde{g}}u & \end{bmatrix}\begin{pmatrix}\phi_1\\ \phi_2\end{pmatrix}\,. \tag{2.18}$$

Therefore

$$\begin{pmatrix}T(0)\\ 0\end{pmatrix} = \begin{bmatrix}\cosh\theta & i\sinh\theta\\ -i\sinh\theta & \cosh\theta\end{bmatrix}\begin{pmatrix}1\\ R(0)\end{pmatrix}\,, \tag{2.19}$$

where

$$\theta = \int_{-\infty}^{\infty}\sqrt{\tilde{g}}u(0,\xi)d\xi = \int_{-\infty}^{\infty}\sqrt{\frac{m}{\hbar^2}}\sqrt{g}u(0,x)dx \tag{2.20}$$

then the transmission coefficient at zero momentum is given by $T(0) = 1/\cosh\theta$, and asymptoti-

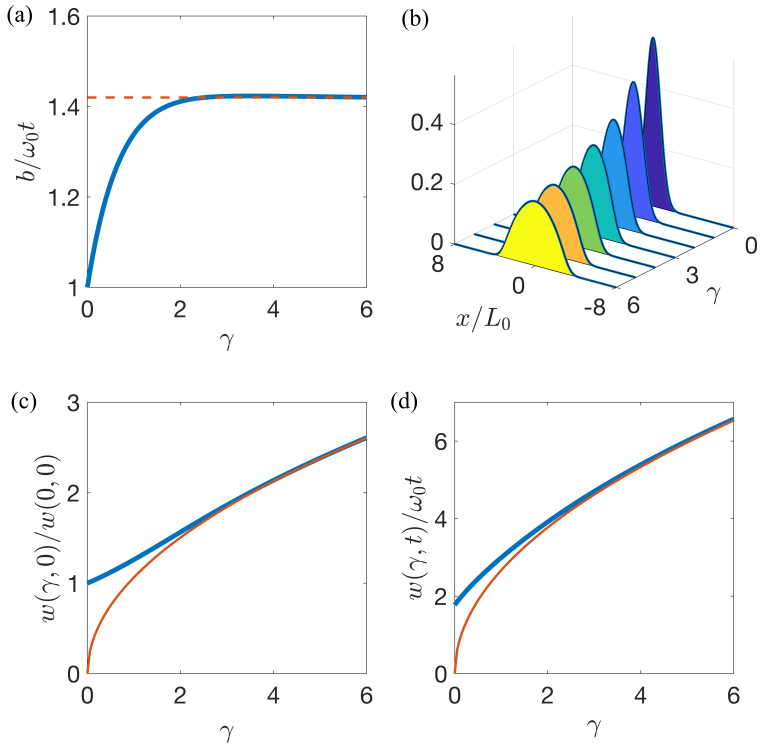

Figure 2.3: (a): Blue line indicates the relationship between b and γ. As we predicted, at long time limit, $b(t) \simeq \sqrt{2}\omega t$. (b): numerical result of the density distribution of condensate in a harmonic trap with different γ with total number of particles $N = 1$. (c): blue line shows ratio between the initial width of the condensate in the harmonic trap and non-interacting one. The red line plots the function $\frac{4\sqrt{2}}{3\sqrt{\pi}}\sqrt{\gamma}$. (d): the width of the condensate asymptotically compared with $\omega_0 t$. The red line plots the function $\frac{8}{3}\sqrt{\gamma}$.

cally

$$n(0,t) = \frac{\hbar}{\pi g t} \ln(\cosh\theta)\,. \tag{2.21}$$

To characterize the expansion of condensates, we defined the width of a condensate by $w = n_t/n(0,t)L_0$, where n_t is the total number of particles, then one way to specify how the system will scale could be defined by using the the central density as

$$b(t) = n(0,0)/n(0,t) = \frac{g n_0}{\hbar \ln(\cosh\theta)}\pi t. \tag{2.22}$$

If the system is initially in a harmonic trap $V = m\omega^2 x^2/2$, and nearly non-interacting, the initial wave-function and the θ with certain central density n_0 is given by

$$u = \sqrt{n_0}\exp\{-m\omega x^2/2\hbar\}\,;\ \theta = \sqrt{2\pi\gamma} \ll 1\,, \tag{2.23}$$

then $n(0,t) \simeq \hbar\theta^2/2\pi g t = n_0/\omega t$, so that $b(t) = \omega t$ asymptotically for nearly non-interacting case. If the system is initially strongly interacting ($\gamma \gg 1$), then the initial wave-function is approximately (Thomas-Fermi limit):

$$u = (n_0 - m\omega^2 x^2/2g)^{1/2} \tag{2.24}$$

for $|x| < (2gn_0/m\omega^2)^{1/2}$ and is zero elsewhere. The corresponding $\theta = (1/\sqrt{2})(\pi\gamma) \gg 1$, and $n(0,t) \simeq \hbar\theta/\pi g t = n_0\sqrt{2}\omega t$, therefore $b(t) \sim \sqrt{2}\omega t$ for strongly interacting case. The results of $b(t)$ at long time limit as γ increasing is shown in Fig. 2.3(a). The result of the initial width of the condensate as a function is illustrated in Fig. 2.3(c), and asymptotically the width of the condensate as a function of γ is shown in Fig. 2.3(d).

The inverse scattering method also helps us to calculate the interference between two condensates. Assuming that the system is initially constricted to two spatially separate harmonic trap, which are located at $x = \pm d/2$ with potentials $V = \frac{1}{2}m\omega^2(x \mp d/2)^2$. For the weakly interacting case ($\gamma \ll 1$), the initial wave-function is two spatially separated Gaussian packets with distance d, then using the Born approximation, one can obtain that asymptotically

$$n(x,t) \propto \cos\left(\frac{md}{2\hbar}\frac{x}{t}\right)\exp\{-\frac{m}{\hbar\omega}\frac{x^2}{t^2}\}\,, \tag{2.25}$$

which matches the exact solution of the non-interacting case.

Another case would be when the interaction effect can not be treated as a perturbation ($\gamma \gtrsim 1$), then the potential U of the corresponding Schrödinger problem for the auxiliary field is

consisted with two relative tall barriers compared with $\lambda^2/4$. The interference patterns or the minima are determined by the perfect transmission of these two identical barriers in series, which is a consequence of resonate scattering by the mechanism of the Fabry-Pérot interferometry. Then the total transmission is

$$|T(\lambda)| = \left| \frac{T_0^2(\lambda)}{1 + |R_0(\lambda)|^2 e^{-i\lambda d/L + 2\delta(\lambda)}} \right|, \tag{2.26}$$

with $T_0(\lambda)$ and $R_0(\lambda)$ is the transmission and reflection coefficients of a single barrier; $\delta(\lambda)$ is the phase shift at momentum λ and is an odd function of λ. In the interacting case, we can see that the visibility of the fringes is not affected, but the width of the interference minima. Locally around a interference minimum, the density profile has the shape of the logarithmic of a Lorentzian distribution. In the interacting case, the effective separation of two potential barriers would be estimated as. $d^* = d - 2\sqrt{2\mu/m\omega^2}$. At strongly interacting limit, the transmission coefficient of a single barrier with a shape of invert parabola can be calculated by the W. K. B. method for the under barrier scattering, which is given by a fermi function:

$$|T_0(\lambda)|^2 \simeq \frac{1}{e^{2\pi(\mu - \frac{\hbar^2\lambda^2}{4mL^2})/\sqrt{2}\hbar\omega} + 1} \tag{2.27}$$

The reason that we consider the under barrier scattering is that, asymptotically density almost vanishes compared with the central density as $\lambda \geq 2\sqrt{\mu m}L/\hbar$, which is already the case of over barrier scattering.

The numerical simulation of the time evolution of the interference of two separated condensates is shown in Fig. 2.4(a), where we take $B = \sqrt{1 + \eta^2/A^2}$ with $A = 16$, and $\rho' = \xi/AB$; $\eta = A\sinh\tau/A$. The numerical result we obtained at long time limit ($\tau = 80$) is shown in Fig. 2.4(b), and the analytical result of the asymptotic density profile calculated from Fabry-Pérot formula is shown in Fig. 2.4(c). As a comparison, the far field solution of the non-interacting case is illustrated in Fig. 2.4(d). The simulation is taken under parameter $\mu \simeq \hbar\omega_0$, and $d^* \simeq 17L_0$.

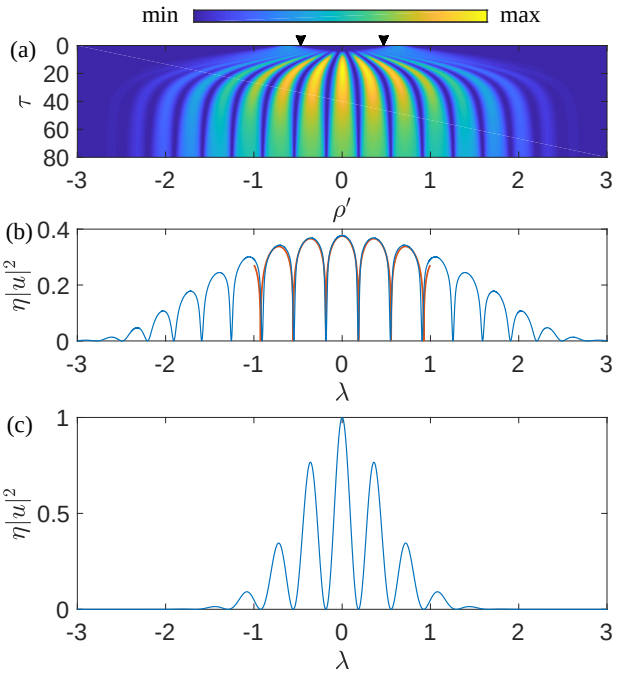

Figure 2.4: the interference pattern of two initially separated packets of condensates. (a) shows the time evolution of a scaled density profile $|u|^2\sqrt{1+\eta^2}$. Two black arrows indicate the starting positions of two separated condensates. (b) shows the numerical result of the density profile at long time limit. (c) shows the analytical result obtained from the Farbry-Pérot transmission formula. From (b) and (c) we can see that the visibility of the fringes are not affected by the interaction but the width of the "dark" lines. (d) shows the result of non-interacting limit as a comparison to the interacting case.

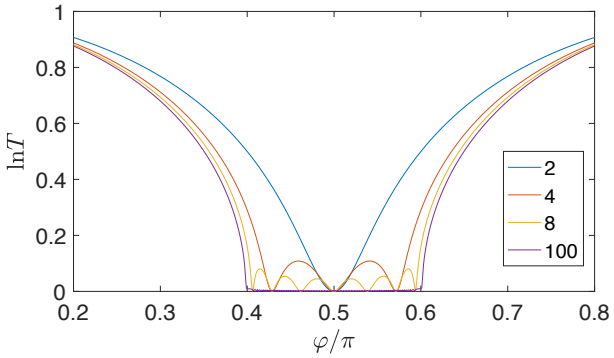

Figure 2.5: comparison of density profile with different number of barriers ($N = 2$, 4, 8 and 100).

2.4 Diffraction from a many-slit array

In this section we examine the scattering problem with N identical barriers separated by equal distances. The double slits interference we discussed in the last section corresponds to $N = 2$. The transfer matrix for a single barrier can be generally written as

$$S_0(\lambda) = \begin{bmatrix} 1/T_0^* & -R_0^*/T_0^* \\ -R_0/T_0 & 1/T_0 \end{bmatrix}, \tag{2.28}$$

where $T_0(\lambda)$ and $R_0(\lambda)$ are the transmission and reflection coefficients for a single barrier respectively, and satisfy $|T_0|^2 + |R_0|^2 = 1$. The free propagation between adjacent barrier is given by the free transfer matrix:

$$S_f(\lambda) = \begin{bmatrix} \exp\{-i\lambda d/2\} & 0 \\ 0 & \exp\{i\lambda d/2\} \end{bmatrix}, \tag{2.29}$$

then the total transfer matrix S_t for N barriers is

$$S_N = (S_f S_0)^N = (S_1)^N, \tag{2.30}$$

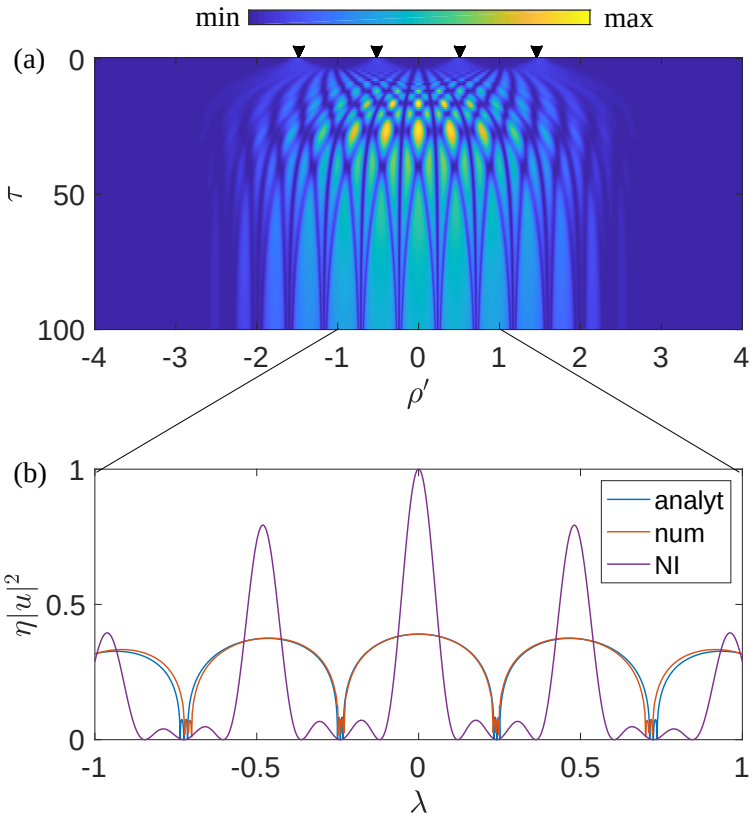

Figure 2.6: (a): time evolution of $|u|^2\sqrt{1+\eta^2}$ for 4 slits diffraction. ρ' and τ is defined same as before. (b): comparison between the analytical predicts and the numerical results of the long time asymptotic density distribution. Numerical results is taken at $\tau = 400$.

where the S_1 can be considered as the effective transfer matrix for a barrier-spacing unit. From Cayley-Hamilton theorem, S_1 satisfies

$$S_1^2 = 2\,\mathrm{Re}\left(\frac{e^{-i\lambda d/2}}{T_0^*}\right) S_1 - 1 = 2\cos\beta S_1 - 1, \tag{2.31}$$

which allows us to calculate the Nth power of S_1. Assuming

$$S_1^{K+1} = U_K S_1 + U_{K-1}\,, \tag{2.32}$$

then the recursive relation of U_K is obtained:

$$U_{K+1} = 2\cos\beta U_K - U_{K-1}, \tag{2.33}$$

which is exactly the recursive relation of 2nd kind Chebyshev polynomial, therefore $U_{K-1} = \sin K\beta/\sin\beta$. With the help of Chebyshev polynomial, the total transmission T_N of N barriers is obtained:

$$|1/T_N|^2 = \left(\frac{1}{|T_0|^2} - 1\right)\frac{\sin^2 N\beta}{\sin^2\beta} + 1. \tag{2.34}$$

Logarithmic of the transmission coefficient gives the shape the asymptotic density distribution, so the knowledge of general property of T_N is needed. β is real when $|\cos\beta| < 1$, and is complex ortherwise. $|T_0| \ll 1$ when the single barrier is relatively high ($\gamma \gg \lambda$), and the phase shift of it is varying much slowly than $\varphi = \lambda d/2$. Therefore within a half period, e.g. φ from 0 to π, $\cos\beta \simeq \cos\varphi/|T_0|$. When $\varphi = 0$, $\beta = i\cosh^{-1}(1/|T_0|) = i\beta_0$ is pure imaginary, and keeps pure imaginary until $\varphi = \cos^{-1}|T_0| \simeq \pi/2 - |T_0|$, and $\beta = 0$. As φ increases from $\cos^{-1}|T_0|$ to $\cos^{-1} -|T_0| \simeq \pi/2 + |T_0|$, β evolves from 0 to π. Finally while φ gradually increase to π, β becomes complex and gradually evolves from π to $\pi + i\beta_0$. There is only a small window that while φ approximately goes from $\pi/2 - |T_0|$ to $\pi/2 - |T_0|$, β is real and increases from zero to π. Within this small window the transmission coefficient oscillates with $N-1$ minima ($N-1$

times of perfect transmissions) as shown in Fig. 2.5, which shows the renormalized density profile (renormalized $\ln T$) as a function of φ for different numbers of barriers. To show the fine structure of the oscillations within the small window that β is real, a relatively large $|T_0| = 0.1\pi$ is taken. Therefore the density profile oscillates approximately from $\pi/2 - |T_0|$ to $\pi/2 + |T_0|$, with $N-1$ minima, and tends to be flat in such region when $N \gg 1$. The long time asymptotic solution can be obtained by the IST method by using the scattering spectrum. The comparison between the numerical and analytical result is shown in Fig. 2.6, where demonstrates an example for $N = 4$.

2.5 Conclusions and outlook

In this chapter, we discuss the possible dynamics of 2D condensates with short range interaction, e.g. IXs, out from different types constrictions at high speed limit (hypersonic). Due to the short range interaction of IXs, we can use the GPE to describe such systems at clean sample limit (ballistic limit) when the temperature is low enough. By applying the paraxial approximation, the 2D problem becomes a quasi 1D problem, and the GPE at 1D is tackled by IST method, which allows us to analytically study the long time behavior of such systems with given initial condition. In particular, we study the dynamics of condensates outgoing from a single constriction, and compare the dynamics at non-interacting and strongly interacting limits. Then the interference of condensates outgoing from two constrictions is also discussed, and the far field patterns of the interference are examined both analytically and numerically. Finally we consider the case the condensates come from an array of N identical constrictions.

In the present work, we mainly focus on the paraxial limit, while the possible physics in the opposite limit where a slowly-moving condensate spreads away from a constriction in the form of a wide-angle "jet" is also rich and can be investigated in the future. When there is a finite density (chemical potential) bias at two sides of a constriction, the transport should exhibit ac Josephson effect.

This chapter, in part, contains material being prepared for submission for publication, 'C. Xu and M. Fogler, **Nonlinear diffraction of Bose gas through single and multiple slits**'. The dissertation author was the primary investigator and author of this paper.

Chapter 3

Model of Bilayer Indirect Excitons

3.1 Introduction

Indirect exciton (IX) is a bosonic quasi-particle consisted with an electron and a hole, which can be created and trapped in a coupled quantum well (CQW) formed by the semiconductor heterostructures, where electrons and holes are living in one of the wells respectively as shown in Fig. 3.2. IXs are charge neutral, while they have dipole moments controlled by the separation of the CQW, so they experience an effective dipole-dipole interaction in a 2D system, which has similar interaction as dipolar systems. Due to their long lifetime [1, 58], high mobility [59] , and long moving distance [2, 3, 4, 5, 6, 7, 8, 9], experimentally IX becomes a platform to study the interacting effects and transport properties of many-body bosonic systems with dipolar interactions.

The study of 2D dipolar interacting systems with numerical simulations attracts much attention recently. Dipolar systems may experience a phase transition from liquid to solid phase [60, 61], when the density or dipole moment increases. The melting of dipolar solids [62] is also studied and proposed to be a first order phase transition. Scattering length instability [63] is also discussed, which results in the mechanism of Bose-Einstein condensation of dipoles, such

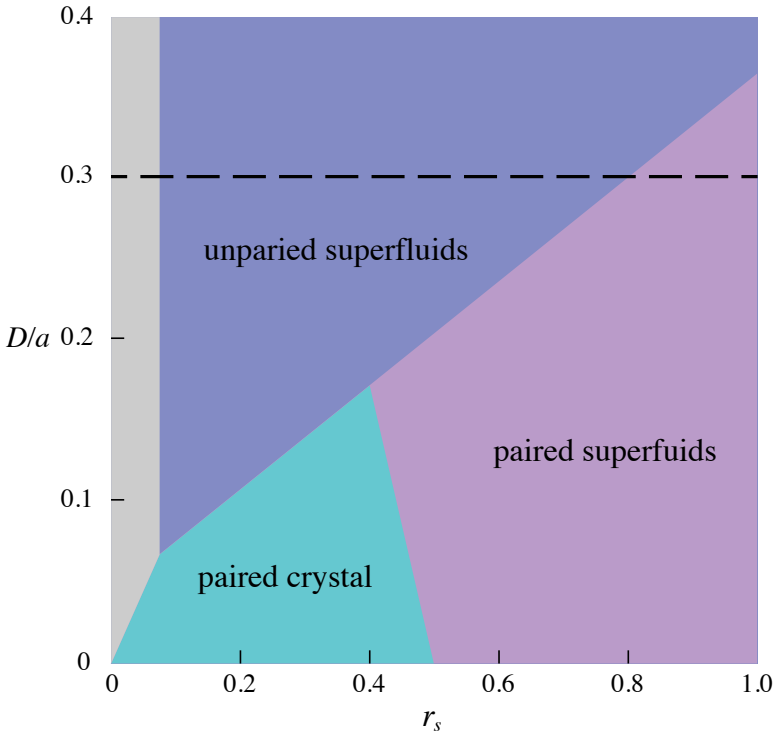

Figure 3.1: schematic plot of the phase diagram of equal density bilayer dipoles.

that verifies the validity of Gross-Pitaevskii description of 2D dipolar systems. The numerical results of ground state energies are summarized in [64], while the excitation property, such as roton property [60, 65, 66] is also studied. By tuning the direction of the dipole moment, there could be a density stripe phase [67, 68] in such inhomogeneous systems. The formation IXs are studied and discussed in the symmetric electron-hole bilayer [69, 70, 71, 72], by the Monte Carlo (MC) simulations for interacting fermions.

In recent experiments [73, 74], two independent CQWs are manufactured in a single semiconductor heterostructure, which makes it possible to investigate the interaction and correlation of interlayer IXs. The interlayer interaction between IXs is attractive when they are close, but repulsive far away. Symmetric bilayer magnetic dipoles, e.g. same interactions, same IXs, and same densities, in stead of having the liquid-solid phase transition, there also could be a dimmerization transition [75, 76, 77], where IXs from two different layers are paired up and form bound states (biexcitons), when the system is dilute enough. The schematic plot of the phase

diagram of symmetric bilayer dipoles with density n and interlayer distance D is shown in Fig. 3.1. In this schematic plot $a = d^2/a_b$, with d and a_b being the dipole moment and Bohr radius, and $r_s = 1/\sqrt{na^2}$. When inter-particle distance is relatively large, the interlayer dimmerization is expected, so the paired phases are favored, while when the interlayer distance D is relatively large, the dipoles in different layer are tend to be uncoupled, so the unpaired phases are expected. The grey region in this plot is a phase of uncoupled bilayer crystal, which is a finite temperature effect. The dashed line indicates the estimated interlayer distance for the actual physical problem we will consider in this article. Density wave instability [78] is also proposed in such system by RPA calculation. Dipolar systems with external fields are also studied, e.g. each layer is constricted by a harmonic trap in the out of plane direction [79] and two types of dipoles in the same layer but has an in plane harmonic trap for both dipoles [80]. The formation of bound states between interlayer dipoles are studied explicitly for few particles (less than 3 particles in each layer) [81]. In reality, IXs do not have exactly the same interaction as magnetic dipoles, and the IXs in each layer do not have to be the same, e.g. IXs may have different dipole moments and densities in each layer, which encourages us to study the physical property of asymmetric setup of IXs bilayer system. We will use Hypernetted chain (HNC) formalism, which is proved to be successful in helium-4 system.

This article is organized as follows. In section 3.2, we will explain the setup of our system, and the simplified model of such setup. The comparison between MC and HNC result of a single layer dipoles will also be presented. Then in section 3.3, we will show the numerical result of ground state energies for various densities in each layer. The low energy excitation properties, which can be characterized by the sound speed will be examined. In the dilute limit of such system, the possible optical branch of the sound mode is also discussed. In section 3.4, we study the scenario where one layer of the IXs is dilute while the other layer is not. In this case, polaron theory can be used, and dilute particles are coupled to the sound mode of a monolayer IXs. We will compare the results between HNC formalism and polaron theory.

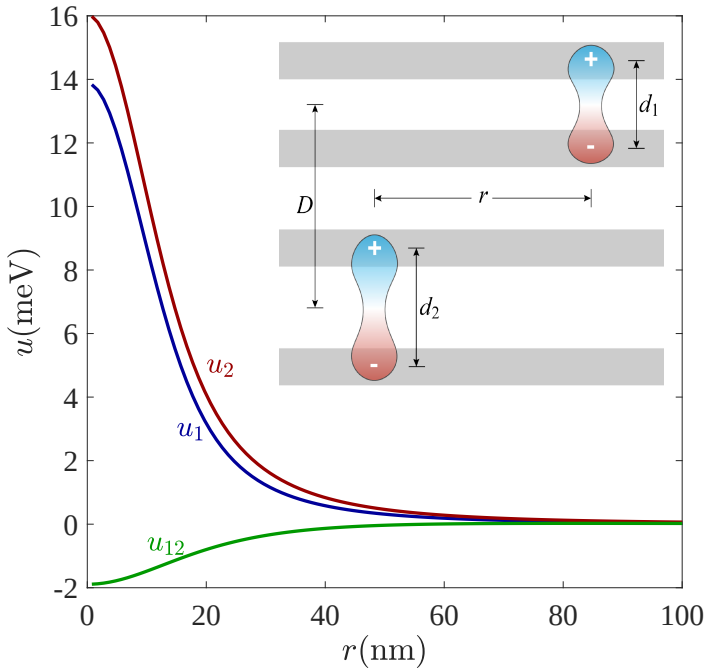

Figure 3.2: Modelled intra- and inter-layer interacting potentials: $u_{1/2}$ are self-interacting potential of IX_1 and IX_2, while u_{12} is the inter-layer interacting potential. Inset figures shows a schematic plot of heterostructure of the system that we consider in this chapter.

3.2 Setup of the IX bilayer system

The system that we will focus on in this chapter is the IXs in a AlAs\AlGaAs sandwich heterostructure as shown in Fig. 3.2, where grey and white layers are AlAs and AlGaAs respectively. Electrons and holes live in the quantum wells, that are the AlAs layers, and such system is a quadrolayer system of electrons and holes. d_1 is the average distance between the top pair of electron-hole layers, while d_2 is the bottom one as shown in Fig. 3.2. If d_1 and d_2 are sufficiently narrow, such that we can treat the top and the bottom electron-hole bilayers as two separated CQWs, and each CQW forms a single layer of IXs with different dipole moments, and the center to center out-plane distance between these two species of IXs is denoted by D. In the following of this chapter, we denote IX_1 and IX_2 as the top and the bottom IX, with n_1 and n_2 being their densities respectively.

The IXs in such heterostructure cannot be treated as a zero-size particle, so we model the inter- and intra-layer interactions between IXs by assuming that the wave-function for each electron and hole is an isotropic Gaussian, e.g.

$$\psi^2(z,r) = \frac{1}{(a\sqrt{2\pi})^3} e^{-\frac{z^2+r^2}{2a^2}}, \tag{3.1}$$

where r and z are the in-plane and out-plane distances from the center of the wave-function, with a as a controlling parameter. The corresponding form-factor of the charge density distribution in the $k-$space is also a Gaussian: $F(k) = e^{-\frac{1}{2}a^2k^2}$. The estimated self-interactions of $IX_{1/2}$ as a in-plane displacement are (Gauss unit)

$$u_{1/2}(r) = -\int \frac{d^3k}{(2\pi)^3} \frac{4\pi e^2}{\varepsilon k^2} F^2(k) 4\cos^2\left(\frac{k_z d_{1/2}}{2}\right) e^{ik_\perp r} \tag{3.2}$$

$$\begin{aligned} &= -2\frac{e^2}{\varepsilon\sqrt{(d_{1/2})^2+r^2}} \mathrm{erf}\left(\frac{\sqrt{(d_{1/2})^2+r^2}}{2a}\right) \\ &\quad + 2\frac{e^2}{\varepsilon r}\mathrm{erf}\left(\frac{r}{2a}\right). \end{aligned} \tag{3.3}$$

Similarly the inter-layer interaction is estimated as

$$\begin{aligned} u_{12}(r) = &\sum_{\sigma\theta} \frac{-\sigma e^2}{\varepsilon\sqrt{(D+\theta\frac{d_1+\sigma d_2}{2})^2+r^2}} \\ &\times \mathrm{erf}\left(\frac{\sqrt{(D+\theta\frac{d_1+\sigma d_2}{2})^2+r^2}}{2a}\right), \end{aligned} \tag{3.4}$$

where σ, $\theta = \pm 1$. Interacting potentials are plotted in Fig. 3.2 under parameters $d_1 = 20$nm, $d_2 = 25$nm, $D = 43$nm, $a = 5$nm, and $\varepsilon = 13$.

IXs are excited by the external lasers, so that the density of IXs can be controlled by tuning the laser output power. Since we do not have identical IX layers, and IX_1 and IX_2 require different photon energy to excite, we can control the output power of two lasers with different

wavelength to obtain the desired n_1 and n_2 independently. The masses of IX_1 and IX_2 are taken to be identical, that are the sum of the effective mass of the electron and hole band in AlAs, which is approximately $m = \frac{1}{5}m_e$. The effective hamiltonian we finally consider is

$$H = H_1 + H_2 + H_{12}\,, \tag{3.5}$$

where

$$H_{1/2} = \sum_{i=1}^{N_{1/2}} -\frac{\hbar^2}{2m}\nabla_i^2 + \sum_{i<j}^{N_{1/2}} u_{1/2}(|\vec{r}_i - \vec{r}_j|) \tag{3.6}$$

$$H_{12} = \sum_{\substack{i=1,N_1 \\ j=1,N_2}} u_{12}(|\vec{r}_i - \vec{r}_j|)\,. \tag{3.7}$$

3.3 Numerical results

To study the interacting effect of the bilayer IX system described above, we use zero-temperature HNC Euler-Lagrange formalism based on binary mixture Jastrow-Feenberg bosonic many-body wave function

$$\Psi = \prod_{i<j}^{N_1} f_1(|\vec{r}_i - \vec{r}_j|) \prod_{i<j}^{N_2} f_2(|\vec{r}_i - \vec{r}_j|) \prod_{\substack{i=1,N_1 \\ j=1,N_2}} f_{12}(|\vec{r}_i - \vec{r}_j|)\,. \tag{3.8}$$

HNC is less accurate but a more computation resource friendly method compared with MC based methods. A comparison of energy and pair correlation function (PCF) is shown Fig. 3.3, for 2D bosons with dipolar interaction (diffusion MC data from Astrakharchik et al.). 2D dipolar systems would be same after simple scaling if they have same $\gamma = na_0^2$, where $a_0 = me^2d^2/\varepsilon\hbar^2$, and n is the density. γ is dimensionless and characterizes the interacting strength of the system. In Fig. 3.3, the mean-field reference of the energy per particle $\Sigma_0 = \frac{n}{2}\frac{4\pi e^2 d}{\varepsilon}$, is defined through capacitor model. From Fig. 3.3, we can see that HNC method provides comparable results for

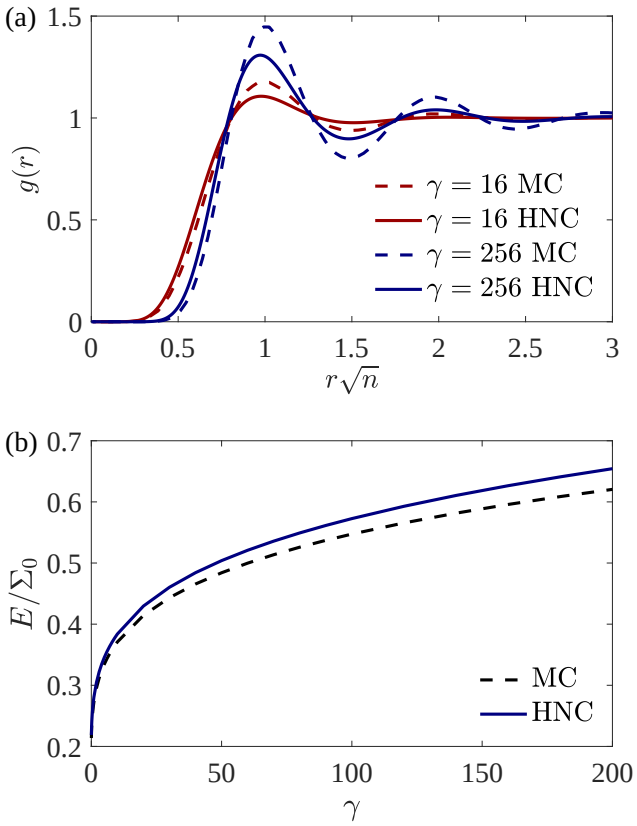

Figure 3.3: (a): comparison of PCF between HNC and MC results with different γ's. (b): comparison of energy per particle, obtained through HNC and MC simulation, with a reference energy Σ_0 from capacitor model.

both energy and PCF when γ is not very large. Typical density of IX system in GaAs\AlGaAs is around 1.0e10cm^{-2}, and typical dipole constant is around 20nm, which results in a $\gamma \sim 1$ in a single layer.

We further perform the HNC calculation for bilayer IXs with various densities of n_1 and n_2, ranging from 0.5e10cm^{-2} to 3.0e10cm^{-2}. The result of energy density is shown in Fig. 3.4(a), where the continuous data is obtained from polynomial fitting. The self-interaction in each layer and the correlation between layers can be reflected by the excitation in such IXs bilayer system. Using Bijl-Feynman theorem for multiple species, the elementary excitation can be estimated from the PCFs calculated by HNC. In our binary mixture system of IXs, there are three distinct PCFs, that are $g_{11}(r)$, $g_{22}(r)$, and $g_{12}(r)$, where their meanings are indicated by the subscriptions. The structural factors is defined through $S_{\alpha\beta} = \delta_{\alpha\beta} + \sqrt{n_1 n_2}\ \mathrm{FT}\{g_{\alpha\beta} - 1\}$. The excitation spectrum can be characterized into two branches,

$$E_{\pm}(k) = \frac{\hbar^2 k^2}{2m\lambda_{\pm}(k)}, \tag{3.9}$$

where

$$\lambda_{\pm} = \frac{1}{2}\left(S_{11} + S_{22} \pm \sqrt{(S_{11} - S_{22})^2 + 4S_{12}^2}\right)$$

are the eigenvalues of the S-matrix (S-matrix is a 2×2 matrix where each element is the structural factor with corresponding indices). In Fig. 3.4 (b) and (c) we present the result of the speed of sound, which is obtained through $v = \lim_{k\to 0} \frac{E(k)}{\hbar k}$. As expected, when n_1 and n_2 both become higher, the correlation between them become weaker (g_{12} become more close to 1), so that the two branches of sound eventually evolves to be the sound excitation of two independent species.

When n_1 and n_2 both become smaller, biexciton bound state between IX_1 and IX_2 may appear, and the system evolves into a paired superfluids phase, while HNC has its own difficulties to study this kind of case when bound sates are present. However in the dilute limit, e.g. the average inter-particle distance is much larger than the radius of the biexciton, we can assume that

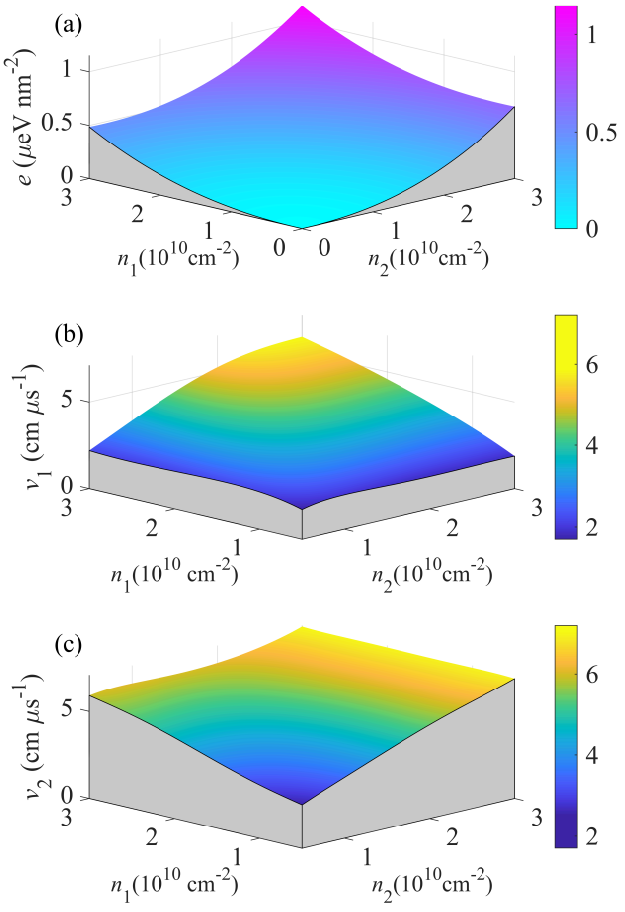

Figure 3.4: (a) the energy density given by HNC. (b) and (c) show the two branches of the speed of sound of the bilayer system obtained from Bijl-Feynman theorem. All figures are plotted by polynomial fitting.

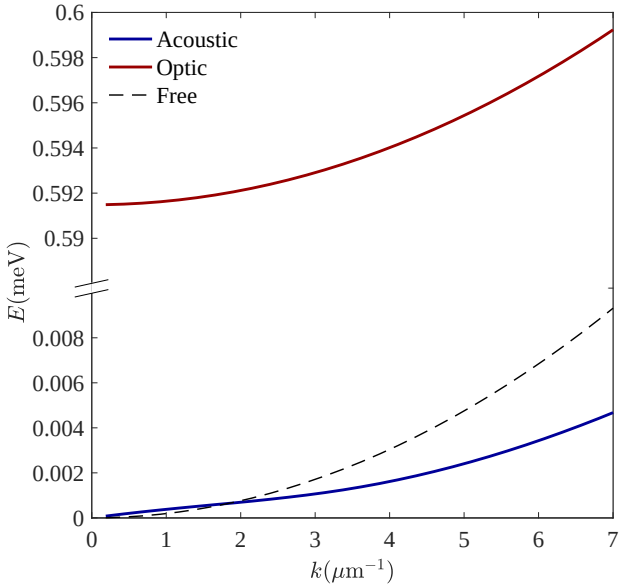

Figure 3.5: the estimated excitation spectrum in the dilute limit when $n_1 = n_2$. A noticeable gap in the excitation can be expected, which results in an optical branch. The dashed curve is non-interacting spectrum, $\hbar^2 k^2/2m$, which is plotted as a reference.

all the excitons will form biexcitons, when $n_1 = n_2 = n_0$. In this limit, the bilayer system can be treated as a monolayer system with interaction $u \simeq u_1 + u_2 + 2u_{12}$, where the PCF g_0 can be calculated by HNC easily for this single component system. Then the PCFs in this limit can be estimated as $g_{11} = g_{22} = g_0$, and $g_{12} = \psi_0^2/n_0 + g_0$, where ψ_0 is the biexciton bound state wave function which can be solved from Schrodinger equation numerically. The inter-layer structural factor becomes

$$S_{12}(k) = \mathrm{FT}\{\psi_0^2\} - 1 + S_0(k)\,, \tag{3.10}$$

where $S_0 = 1 + n_0 \mathrm{FT}\{g_0 - 1\} = S_{11} = S_{22}$. If $\mathrm{FT}\{\psi_0^2\} \simeq 1 - \eta k^2$, at small momentum k, one of the S-matrix eigenvalues $\lambda_- \simeq \eta k^2$, then $E_-(0) = \hbar^2/2m\eta$ becomes finite. Therefore an optic branch may emerge for dilute system, and the other one is still acoustic. As an example, we show the spectrum result in Fig. 3.5 for $n_0 \simeq 3.91\mathrm{e}7$ cm^{-2} (inter-particle distance is 1600nm) by using the approximation described above.

3.4 Imbalanced case

In this section, we will focus on the case that IX_1 is much more dilute than IX_2, such that IX_1 can be treat as an impurity in a background of IX_2 bosonic layer. This problem can be also viewed as a polaron problem, that a single IX_1 particle interacts with IX_2 particles and couple to the sound mode of IX_2. Using polaron theory, the spectrum bottom of IX_1 E_0 can be calculated, which can be also viewed as the chemical potential of IX_1. The second quantization description of the inter-layer interaction can be written as

$$\hat{H}_{\text{int}} = \sum_{p,k,q} v_{12}(q)\psi_1^\dagger(p+q)\psi_2^\dagger(k-q)\psi_1(p)\psi_2(k) \tag{3.11}$$

$$\simeq \sum_{p,q} \frac{\sqrt{N_2 S_{22}(q)}}{L^2} v_{12}(q)\psi_1^\dagger(p+q)\psi_1(p)(\rho_q + \rho_{-q}^\dagger)\,, \tag{3.12}$$

where ψ_1 and ψ_2 are the annihilation operators of IX_1 and IX_2 respectively, and L^2 is the area of the system. ρ_q is the density operator with momentum q for IX_2. The corresponding Frohlich hamiltonian for a single IX_1 is then

$$\begin{aligned} H_F =& \frac{p^2}{2m} + \sum_q \frac{\hbar^2 q^2}{2mS_{22}(q)}\rho_q^\dagger \rho_q + \frac{N_2}{L^2} v_{12}(0) \\ &+ \sum_q \frac{1}{L^2} v_{12}(q)\sqrt{N_2 S_{22}(q)} e^{iq\cdot r}(\rho_q + \rho_{-q}^\dagger)\,. \end{aligned} \tag{3.13}$$

The bottom of the single particle spectrum is then given by

$$\begin{aligned} E_0 &= -N_2 \frac{1}{L^4} \sum_q \frac{(v_{12}(q)S_{22}(q))^2}{\frac{\hbar^2 q^2}{2m}(1+S_{22}(q))} + \frac{N_2}{L^2} v_{12}(0) \\ &= -n_2 \int \frac{d^2 q}{(2\pi)^2} \frac{v_{12}(q)^2}{\frac{\hbar^2 q^2}{2m}} \frac{S_{22}(q)^2}{1+S_{22}(q)} + n_2 v_{12}(0)\,. \end{aligned} \tag{3.14}$$

The result of E_0 the polaron theory is shown in Fig 3.6, with structural factor S_{22} calculated by HNC.

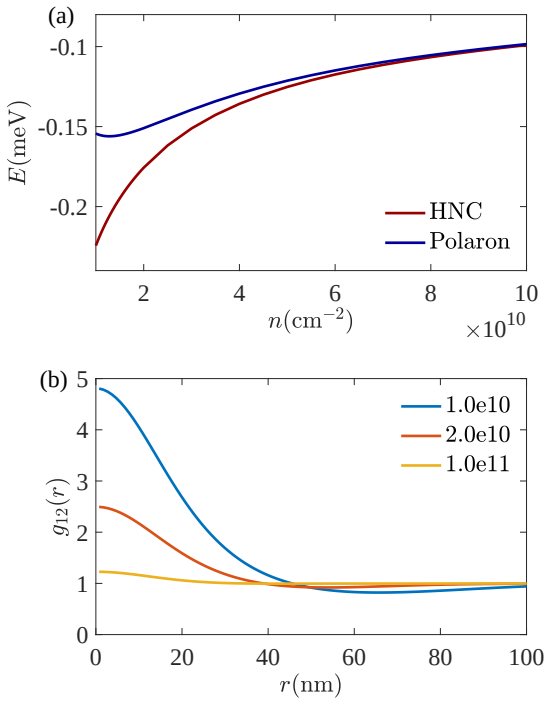

Figure 3.6: (a): comparison of the single particle energy between polaron theory and HNC. (b): the inter-layer PCFs given by HNC for various densities in the unit of cm^{-2}.

Alternatively, we can calculate the correlation between IX_1 and IX_2 directly by HNC in the dilute limit of IX_1. The Euler-Lagrange equation for g_{22} is same as the single component one, while the equation for g_{12} is

$$\left(-\frac{\hbar^2\nabla^2}{m}+v_{12}(r)+W_{12}(r)\right)g_{12}^{1/2}(r)=0\,, \tag{3.15}$$

where $\mathrm{FT}\{W_{12}\}=-\frac{\hbar^2k^2}{4mn_2}S_{12}(S_{22}-1)(2S_{22}+1)/S_{22}^2$ (here S_{12} is calculated by $n_2\mathrm{FT}\{g_{12}-1\}$). The results of the PCF and energy obtained from HNC is shown in Fig. 3.6. One can see that polaron theory agrees with HNC at relatively high density, while the speed of sound is relatively large, so that IX_1 finds it hard to couple with sound mode with high momentum, which result in a more linear response regime. In this regime, S_{22} can be roughly estimated as

$$S_{22}(k)\simeq\frac{\hbar^2k}{2m\sqrt{\frac{\hbar^2n_2}{2m}v_{22}(k)}}\,, \tag{3.16}$$

where $\sqrt{\frac{\hbar^2n_2}{2m}v_{22}(k)}=c(k)$ is approximately the speed of sound. Therefore at large n_2 limit, E_0 in (3.14) can be evaluated as

$$E_0\simeq-\int\frac{d^2q}{(2\pi)^2}\frac{v_{12}^2(q)}{v_{22}(q)}+n_2v_{12}(0)\,. \tag{3.17}$$

This result agrees with the linear response result, since in this regime,

$$n_2\mathrm{FT}\{g_{12}-1\}\simeq-v_{12}(q)/v_{22}(q)\,.$$

3.5 Conclusions and outlook

In this chapter, we specifically modeled an asymmetric bilayer excitonic system in GaAs\AlGaAs heterostructures with physical allowed parameters, where excitons have dipolar

interaction. First, we compare the results of a single layer of dipoles between diffusion Monte Carlo and HNC, and show the agreement of these two numerical methods. Using multiple species HNC formalism, we then calculate several zero-temperature properties of such system with different densities in each layer, including energy densities and PCFs.

We further estimate the elementary excitations of such bilayer system, two branches of sounds, with various densities in each layer as shown in Fig. 3.4 (b) and (c). In addition, we discuss and calculate the optical branch of spectrum in the dilute limit (equal density in two layers), due to the formation of bound state (biexcitons), and the result is shown in Fig. 3.5. Finally, we examine the scenario that only one layer is dilute, and compare the results of single particle energy in the dilute layer between HNC and Polaron theory (see Fig. 3.6). These two methods agree with each other in the high density limit (linear response regime) as expected.

The excitation spectra can be detected by the angle-resolved spectroscopy technique, and a sound type dispersion has been observed in an interacting polariton system[82]. As for a bilayer excitonic system, similar experiments can be done, and two branches of sound excitations are expected, which can be compared to our prediction of sound velocities. Based on the results of the sound velocities v, The resonant vibrating (breathing) modes can be estimated. The actual shape of trapped exciton liquids can be controlled by the external electric gates[83, 84, 85]. Assume the exciton trap is in an elongated shape with length L, then the resonant frequency $f \sim \frac{1}{2}\frac{v}{L}$. If we take $L \sim 50\mu$m and $v \sim 5$ cm$/\mu$s, $f \sim 5$GHz, which is the regime of fast spectroscopy. More detailed calculation of oscillating modes can be carried out based on the details of the trap shape and the density distribution of excitons in a shaped trap.

3.A HNC equations

HNC approximation allows us to solve the self-consistent equations [86] of PCFs directly, if the densities of components and interactions between them is given. The equations for PCFs

for a mixture of two equal-mass components are given by

$$\left(-\frac{\hbar^2\nabla^2}{m}+v_{\alpha\beta}(r)+W_{\alpha\beta}(r)\right)g_{\alpha\beta}^{1/2}(r)=0\,, \tag{3.18}$$

where $W_{\alpha\beta}$ are the the induced potentials, and the Fourier transform of these potentials FT$\{W\}$ are

$$w_{\alpha\alpha}=-\frac{\hbar^2k^2}{4n_\alpha m}\left(2S_{\alpha\alpha}-3+\frac{S_{\beta\beta}^2+S_{\alpha\beta}^2}{D^2}\right) \tag{3.19}$$

$$w_{\alpha\beta}=-\frac{\hbar^2k^2}{4\sqrt{n_\alpha n_\beta}m}\left(2S_{\alpha\beta}-S_{\alpha\beta}\frac{S_{\alpha\alpha}+S_{\beta\beta}}{D^2}\right), \tag{3.20}$$

with D being $S_{11}S_{22}-S_{12}^2$, and in above equations $\alpha\neq\beta$. Using the S-matrix, we can organize these equations in a more compact form

$$w_{\alpha\beta}=-\frac{\hbar^2k^2}{4m\sqrt{n_\alpha n_\beta}}(2S_{\alpha\beta}-3\delta_{\alpha\beta}+\left[(S^{-1})^2\right]_{\alpha\beta})\,, \tag{3.21}$$

which also holds for systems with more than two components. The HNC we use in the section 3.4 for impurity case is obtained by setting $S_{11}=1$, and only solve for g_{22} and g_{12}. After solving the PCFs, the energy of a binary mixture is then

$$E=\frac{1}{2}\int d^2r\left(n_1^2g_{11}v_{11}+n_2^2g_{22}v_{11}+2n_1n_2g_{12}v_{12}\right) \tag{3.22}$$

$$+\frac{\hbar^2}{2m}\int d^2r\left(n_1^2(\nabla\sqrt{g_{11}})^2+n_2^2(\nabla\sqrt{g_{22}})^2+2n_1n_2(\nabla\sqrt{g_{12}})^2\right) \tag{3.23}$$

$$+\frac{\hbar^2}{8m}\int\frac{d^2k}{(2\pi)^2}k^2(-6+S_{11}(3-S_{11})+S_{22}(3-S_{22})-2S_{12}^2+\frac{S_{22}+S_{11}}{D})\,. \tag{3.24}$$

This chapter, in part, contains material being prepared for submission for publication, 'C. Xu and M. Fogler, **Hypernetted chain study of coupled exciton liquids in electron-hole quadrilayers**'. The dissertation author was the primary investigator and author of this paper.

Chapter 4

Superconducting Junction with Tri-Component Gap Functions

4.1 Introduction

Chiral superconductors constitute a class of superconducting states of matter characterized by unconventional gap functions, spontaneous time-reversal symmetry breaking, and nontrivial topological properties [87]. The topological structure in the pairing wavefunctions leads to exotic phenomena, including the emergence of Majorana zero modes in vortex cores [88, 89, 90, 91, 92] and chiral Majorana fermions on the boundary of the system [93, 94, 95], which can be useful in realizing topological quantum computations [96, 97, 98, 99, 100]. The superconducting Sr_2RuO_4 [101, 102, 103, 104] and UPt_3 materials [105, 106, 107, 108] have been proposed to host chiral superconductivity with p- and f-wave pairing gap functions, respectively, though there are still debates over the pairing nature of these materials [103, 109, 110, 111] despite intensive theoretical and experimental studies [112, 113, 114, 115, 116, 117, 118, 119, 120].

In general, when instabilities in several pairing channels coexist, the system may develop a superposition of gap function symmetries which spontaneously breaks time-reversal symmetry. A

typical pattern of time-reversal symmetry breaking is that a relative $\pm\frac{\pi}{2}$ phase difference develops between two different pairing channels with different symmetries, which has been studied in various systems including the ^{3}He-A superfluid phase [121, 122], and superconductors with p_x+ip_y [123, 124, 98, 125, 126, 90, 127, 128], and $d_{x^2-y^2}$+id_{xy}[129, 130, 131, 132, 133, 134, 135, 136, 137, 138, 139, 140, 141, 142, 143] gap function symmetries. The mixing between the s-wave and p-wave gap function symmetries with a relative phase difference $\pm\frac{\pi}{2}$ was first proposed by one of the author and Hirsch in the context of superfluid instability of dipolar fermions [144], and was later generalized to other systems [145, 146, 147]. Mixed gap function symmetries breaking time-reversal symmetry have also been proposed in the iron-based superconductors [148, 149] and other related systems, such as s+id[148, 150, 151, 152, 153, 154, 155], s+is[156, 157, 158, 159, 160, 161, 162, 155, 149]. On the other hand, the interplays among three or more different superconducting order parameters remain less explored [163, 164, 165].

In this article, we study the superconductor-superconductor junction with one side characterized by a chiral p-wave gap function symmetry and the other side the conventional s-wave one, respectively, as illustrated in Fig. 4.1. In the junction region, three gap function symmetries coexist due to the proximity effect. The linear Josephson coupling is not allowed due to their different symmetries, and any two of them can only be coupled via the quadratic Josephson term at the lowest order. Any two of them favor a relative phase of $\pm\frac{\pi}{2}$, however, the system is frustrated since a simultaneous mutual $\pm\frac{\pi}{2}$ phase difference is impossible among three order parameters. This frustration is different from that of the antiferromagnetism defined in the triangular lattice in which the bilinear Heisenberg coupling is analogous to the linear Josephson coupling. To determine the frustrated pattern of the gap functions, a Ginzburg-Landau free-energy analysis is performed. The gap function structure in the junction region is solved to exhibit an exotic form $s+i\eta_1(e^{i\eta_2\varphi/2}p_x+\eta_3 e^{-i\eta_2\varphi/2}p_y)$ as shown in Fig. 4.2, where φ is the phase difference between the p_x- and p_y-pairing order parameters, and $\eta_j=\pm1$ ($j=1,2,3$). By fixing the chirality deep in the p-wave layer as the boundary condition, the time-reversal and reflection symmetries are

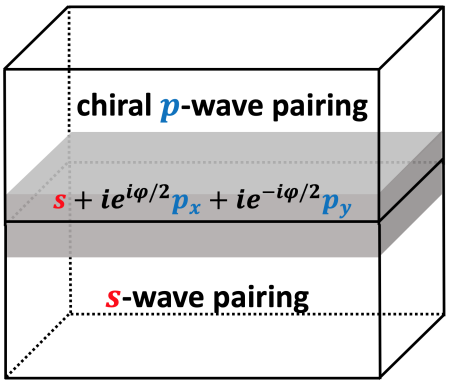

Figure 4.1: The heterojunction formed by a chiral p-wave superconductor in the upper space and an s-wave superconductor in the lower space. A mixed tri-component gap function develops near the interface of the heterojunction induced by the proximity effect. The z-direction is chosen along the crystalline c-axis as pointing upwards.

explicitly broken. The frustration spontaneously breaks the C_4 symmetry and can be viewed as a frustration induced nematic superconductivity. In the junction region, the tri-component pairing further breaks the residual C_4 symmetry, and the four degenerate configurations satisfy $\eta_2\eta_3 = -\eta_c$ ($\eta_c = \pm 1$) when the boundary condition is chosen as $p_x + i\eta_c p_y$.

Furthermore, we find that the system exhibits an anisotropic magnetoelectric effect around the edge of the junction, consistent with the C_4 symmetry breaking. The magnetoelectric effect also manifests itself as the emergence of an anisotropic spin magnetization on the edge of the junction, which can be analyzed through the splitting of the two spin-polarized chiral Majorana edge modes.

The rest part of this article is organized as follows. In Sect. II, the Ginzburg-Landau free energy analysis is performed, and the origin of frustration among gap functions is illustrated. The anisotropic magneto-electric effect and the edge magnetization are studied in Sect. III. The relation between the edge magnetization and the gap function mixing is presented in Sect. IV. Conclusions are given in Sect. V.

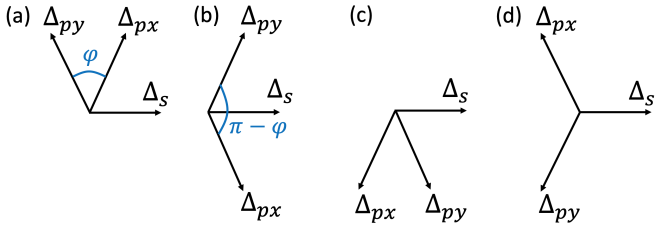

Figure 4.2: Plots of the four tri-component pairing configurations with the positive chirality, i.e., $s+i\eta_1(e^{i\eta_2\varphi/2}p_x+\eta_3 e^{-i\eta_2\varphi/2}p_y)$ where $\eta_2\eta_3=-1$. In (*a-d*), $|\Delta_{px}|=|\Delta_{py}|$, and the phase of the s-wave pairing is fixed to be zero. The configurations in (*b*), (*c*), and (*d*) can be obtained by performing the C_4 rotations at the angles of $\pi/2$, π, and $3\pi/2$ on the configuration of (*a*), respectively. We note that the rotations are performed in the orbital space not on the phase configurations of the gap functions illustrated in Figures (*a-d*). Hence, the rotation of $\pi/2$ keeps Δ_s unchanged, and $\Delta_{px}\to\Delta_{py}$ and $\Delta_{py}\to-\Delta_{px}$.

4.2 Ginzburg-Landau free energy analysis

4.2.1 Brief review of the $p_x\pm ip_y$ pairing

We first briefly review the Ginzburg-Landau free energy analysis for the chiral p-wave superconductor with the $p_x\pm ip_y$ pairing. The point group symmetry is assumed to be the D_{4h} group, which applies to a tetrahedral lattice system. The most general Ginzburg-Landau free energy respecting the U(1) gauge, the time reversal, and the D_{4h} point group symmetries up to quartic order is

$$\begin{aligned} f_1 &= \alpha_p(|\Delta_{px}|^2+|\Delta_{py}|^2)-g_{pp}|\Delta_{px}^*\Delta_{py}-\Delta_{py}^*\Delta_{px}|^2 \\ &\quad +\beta_p(|\Delta_{px}|^2+|\Delta_{py}|^2)^2+\beta_p'(|\Delta_{px}|^4+|\Delta_{py}|^4), \end{aligned} \tag{4.1}$$

in which Δ_{px}, Δ_{py} are the order parameters of the p_x- and p_y-wave pairing gap functions, respectively; $\alpha_p<0$ in the superconducting state; $\beta_p>0$ is the coefficient of the corresponding rotationally invariant phase-non-sensitive quartic term; the β_p' term breaks the SO(2) rotational symmetry down to C_4; $g_{pp}>0$ is the coefficient of the term which contains the quadratic Josephson coupling $(\Delta_{px}^*\Delta_{py})^2+\text{h.c.}$; and only the uniform parts of the free energy are kept while the

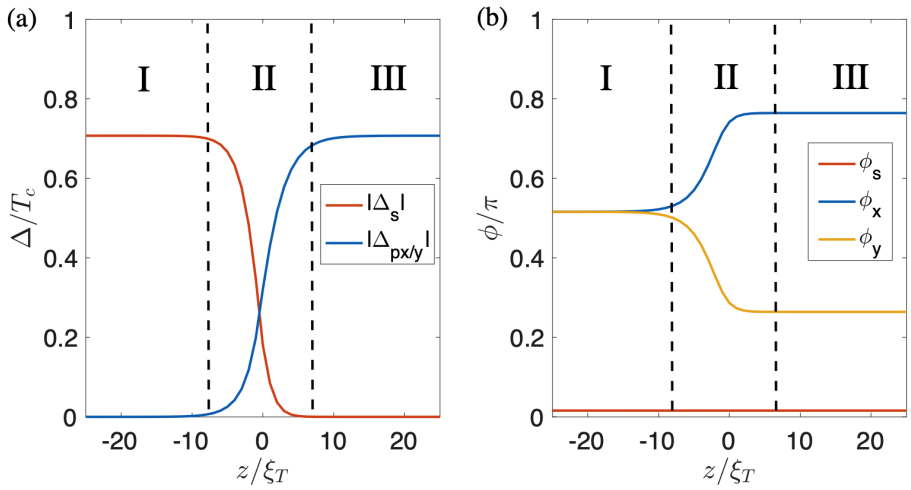

Figure 4.3: Magnitudes of the gap function $|\Delta_s|$ (red curve) and $|\Delta_{px}| = |\Delta_{py}|$ (blue curve) as functions of z in (*a*); and their phases ϕ_s (red curve), ϕ_x (blue curve) and ϕ_y (yellow curve) as functions of z in (*b*). The intervals of z marked by "I, II, III" represent the regions where *s*-wave dominates, *s*- and *p*-wave coexist, and *p*-wave dominates, respectively. The units for $|\Delta_\lambda|$ ($\lambda = s, p_x, p_y$) and the spatial coordinate z are the transition temperature T_c and the coherence length $\xi_T = v_F/T_c$, respectively, where v_F is the Fermi velocity. The parameters in the numerical calculations are chosen as $K_s = K_p = 10N_F\xi_T^2$, $\alpha_s = 2\mathrm{sgn}(z)N_F$, $\alpha_p = -\mathrm{sgn}(z)N_F$, $\beta_s = 2N_F/T_c^2$, $\beta_p = 3.75N_F/T_c^2$, $\beta_p' = 0.5N_F/T_c^2$, $g_{sp} = 3.5N_F/T_c^2$, $g_{pp} = 3.5N_F/T_c^2$, $\gamma = 10N_F/T_c^2$, where N_F is the density of states at the Fermi level, and T_c is the superconducting transition temperature.

gradient terms are neglected.

Since g_{pp} is generically positive, the energy of the quadratic Josephson term is lowered if a $\pm\pi/2$ phase difference is developed between Δ_{px} and Δ_{py}. As a result, the $p_x \pm ip_y$ pairing is favored which spontaneously breaks the time-reversal symmetry. Though the $p_x \pm ip_y$ pairing breaks both U(1) gauge and C_4 rotational symmetries, it is invariant under $GR(\hat{z}, \pi/2)$, where $R(\hat{z}, \pi/2)$ is the $\pi/2$ rotation around z-axis in the orbital space and G is the gauge transformation by $\pm\pi/4$ of the electrons (i.e., $\pm\pi/2$ phase rotation of the Cooper pairs). In particular, $L_z + \frac{1}{2}N$ remains to be a conserved quantity when $\beta_p' = 0$.

4.2.2 Minimization of the free energy for the junction

Next we proceed to discuss the tri-component pairing gap function as a consequence of the competition among three pairing order parameters. The system under consideration is a heterojunction formed by a chiral p-wave superconductor in the upper space and an s-wave superconductor in the lower space, as shown in Fig. 4.1. The pairing Hamiltonians deep in the upper and lower spaces in Fig. 4.1 are given by

$$\begin{aligned} \hat{\Delta}_p &= \sum_{\vec{k}\alpha\beta} \frac{1}{k_f}(|\Delta_{px}|k_x + i|\Delta_{py}|k_y)(\sigma^z i\sigma^y)_{\alpha\beta} c^\dagger_{\vec{k}\alpha} c^\dagger_{-\vec{k}\beta}, \\ \hat{\Delta}_s &= |\Delta_s| \sum_{\vec{k}} c^\dagger_{\vec{k}\uparrow} c^\dagger_{-\vec{k}\downarrow}, \end{aligned} \tag{4.2}$$

in which $\alpha, \beta = \uparrow, \downarrow$ are the spin indices; $c^\dagger_{\vec{k}\alpha}$ is the electron creation operator with momentum $\vec{k}$ and spin α.

On the other hand, due to the proximity effect, there is a mixture of p-wave (Δ_{px}, Δ_{py}) and s-wave (Δ_s) superconducting order parameters in the junction region. To study the pattern of the mixture, we take a Ginzburg-Landau free energy analysis. Because of the heterostructure, the point group symmetry becomes the planar C_{4v} group, which contains the C_4 rotations and four reflections. Assuming $U(1)$ gauge, time reversal, and C_{4v} symmetries, the free energy density up to quartic order takes the form

$$f = f_p + f_s + f_{sp} + f'_{sp}, \tag{4.3}$$

in which

$$\begin{aligned} f_s &= K_s|\nabla_z\Delta_s|^2+\alpha_s|\Delta_s|^2+\beta_s|\Delta_s|^4 \\ f_p &= K_p(|\nabla_z\Delta_{px}|^2+|\nabla_z\Delta_{py}|^2)+f_1 \\ f_{sp} &= g_{sp}[\Delta_s^{*2}(\Delta_{px}^2+\Delta_{py}^2)+\text{c.c.}] \\ f'_{sp} &= \gamma(|\Delta_{px}|^2+|\Delta_{py}|^2)|\Delta_s|^2, \end{aligned} \tag{4.4}$$

where f_1 within f_p is given by Eq. (4.1) and "c.c." is "complex conjugates" for short. The coefficient of each term up to tree level can be determined by a diagrammatic calculation as discussed in detail in Appendix 4.A.

To mimic the junction structure close to the $z=0$ interface, we set

$$\begin{aligned} &\alpha_p(z)<0, \alpha_s(z)>0, \text{ for } z>0, \\ &\alpha_p(z)>0, \alpha_s(z)<0, \text{ for } z<0, \end{aligned} \tag{4.5}$$

so that the p_x+ip_y pairing dominates deep in the upper space, whereas the s-wave pairing dominates deep in the lower space. Due to the gradient terms led by K_p and K_s, the pairing gap function cannot exhibit a sudden change. Therefore we expect that the p_x-, p_y- and s-wave pairing symmetries should coexist close to the $z=0$ interface.

To obtain an intuitive understanding, we take a quick look at the phase sensitive terms in the free energy. The phase sensitive g_{sp} and g_{pp} terms are

$$g_{sp}[\Delta_s^{*2}(\Delta_{px}^2+\Delta_{py}^2)+\text{c.c.}]-g_{pp}|\Delta_{px}^*\Delta_{py}-\Delta_{py}^*\Delta_{px}|^2, \tag{4.6}$$

which can be evaluated as

$$2g_{sp}|\Delta_s|^2|\Delta_p|^2[\cos(2\phi_x-2\phi_s)+\cos(2\phi_y-2\phi_s)] \\ +2g_{pp}[\cos(2\phi_x-2\phi_y)-1], \tag{4.7}$$

where $\Delta_s=|\Delta_s|e^{i\phi_s}$, $\Delta_{px}=|\Delta_p|e^{i\phi_x}$, and $\Delta_{py}=|\Delta_p|e^{i\phi_y}$. Each term in Eq. (4.7) is minimized if ϕ_x, ϕ_y and ϕ_s mutually differ by $\pm\pi/2$. However, Eq. (4.7) is frustrated since a simultaneous mutual $\pi/2$ difference among three phases is impossible. Therefore, there will be a competition between the phases of the superconducting order parameters in the coexisting region.

To determine the pattern arising from the competition, we apply an iterative numerical method to obtain the solution of the pairing gap function by minimizing the free energy. The numerical results for the magnitudes and phases of the superconducting order parameters are displayed in Fig. 4.3 (a) and (b), respectively. It is found that the solutions of the magnitudes $|\Delta_{px}|$ and $|\Delta_{py}|$ are equal as shown in Fig. 4.3 (a). As can be seen from Fig. 4.3 (a), the system can be clearly divided into three regions: the region marked with "I" where the s-wave pairing dominates (deep inside the s-wave bulk); region "II" between the two vertical dashed lines where all the three pairing symmetries coexist; and region "III" where the p_x, p_y-wave pairings dominate (deep inside the bulk of the chiral p-wave superconductor). In the numerical calculations, the phase ϕ_s of the s-wave pairing is chosen to be zero for $z<0$ and $|z/\xi_w|\gg 1$ where $\xi_w=\sqrt{|K_s/\alpha_s|}$ represents the width of the coexisting region. Then ϕ_s is solved to remain at zero in the entire junction as indicated by the red line in Fig. 4.3 (b).

As can be seen from Fig. 4.3 (b), deep inside the p-wave bulk, Δ_{px} and Δ_{py} have a relative $\pi/2$ phase difference, and the magnitude of Δ_s is nearly negligible. When approaching the junction from the p-wave side, the magnitudes of Δ_{px} and Δ_{py} start shrinking and so does the phase φ between them, whereas the magnitude of Δ_s keeps growing. Eventually when leaving the coexisting region and entering the s-wave bulk, Δ_s is much larger than Δ_{px} and Δ_{py} in magnitude.

We note that the three phases ϕ_x, ϕ_y and ϕ_s exhibit the following pattern throughout the whole space,

$$\begin{aligned} \phi_x - \phi_y &= \varphi \\ \frac{\phi_x + \phi_y}{2} - \phi_s &= \frac{\pi}{2}. \end{aligned} \tag{4.8}$$

As a result, the tri-component pairing gap function in the coexisting region can be written as $s + i(p_x e^{i\varphi/2} + p_y e^{-i\varphi/2})$ as shown in Fig. 4.2 (a), in which φ decreases from $\pi/2$ down to 0 as the junction is traversed from $z > 0$ to $z < 0$.

4.2.3 Symmetry breaking pattern

In closing this section, we discuss the symmetry breaking pattern in the junction region. Clearly, all symmetry transformations $T, C_4, M_x, M_y, M_{x-y}, M_{x+y}$ are spontaneously broken, where $M_{f(x,y)}$ represents the spin-orbit coupled reflection with respect to the $f(x,y) = 0$ plane. In particular, $L_z + \frac{1}{2}N$ is not conserved when $\beta_p' = 0$. However, the tri-component pairing $s + i(p_x e^{i\varphi/2} + p_y e^{-i\varphi/2})$ is invariant under TM_{x-y}. Hence, the unbroken symmetry group is $\langle TM_{x-y} \rangle \simeq \mathbb{Z}_2$, in which $\langle \cdots \rangle$ represents a group generated by the operations inside the bracket. As a result, the symmetry breaking pattern for the tri-component pairing is $C_{4v} \times \mathbb{Z}_2^T \to \mathbb{Z}_2$, in which $\mathbb{Z}_2^T$ on the left side of the arrow represents $\langle T \rangle$, i.e., the group generated by the time reversal operation. Since $|C_{4v} \times \mathbb{Z}_2^T| / |\mathbb{Z}_2| = 8$, there are eight degenerate solutions of the pairing configurations given by

$$s + i\eta_1 (e^{i\eta_2 \varphi/2} p_x + \eta_3 e^{-i\eta_2 \varphi/2} p_y), \tag{4.9}$$

in which $\eta_j = \pm 1$ $(j = 1, 2, 3)$.

On the other hand, the boundary condition deep in the p-wave bulk needs to be specified

when minimizing the free energy, which amounts to fixing the chirality (i.e., $p_x + ip_y$ or $p_x - ip_y$) deep in the upper space. The choice of the boundary condition explicitly breaks the time reversal and reflection symmetries since they both flip the chirality. By putting the s- and chiral p-wave superconducting layers in contact with each other, the junction structure further breaks the residual C_4 symmetry, [1] where the action of the C_4 rotational operation on the chiral p-wave pairing is defined up to a gauge transformation. The corresponding four degenerate tri-component pairing configurations among the eight ones in Eq. (4.9) satisfy $\eta_2\eta_3 = -\eta_c$, when the boundary condition is chosen as $p_x + i\eta_c p_y$ where $\eta_c = \pm 1$. Fig. 4.2 (a-d) display the configurations for the positive chirality case (i.e., $p_x + ip_y$), and the other four negative chirality configurations can be obtained from those in Fig. 4.2 by switching Δ_{px} and Δ_{py}.

4.3 Anisotropic magnetoelectric effect and edge magnetization

In this section, we discuss a novel type of anisotropic magnetoelectric effect in the tri-component pairing heterojunction. Using a linear response approach, we show that a spatial variation of the electric potential can induce spin magnetizations along z-direction with a strength dependent on the direction of the electric field. Since an edge corresponds to a change of the electric potential, we conclude that the edge of the heterojunction carries anisotropic spin magnetization if the potential change in the vicinity of the edge is slow enough such that the linear response approximation applies. In the next section, we make a complimentary analysis on the opposite limit where the electric potential changes abruptly at the edge. The anisotropic edge magnetization is shown to emerge as the consequence of the splitting between the two

[1] Here we note that strictly speaking, the residual symmetry group is not just C_4. The full residual symmetries of the $p_x + ip_y$ pairing are $\{1, r, r^2, r^3, TM_x, G'TM_y, GTM_{x-y}, G^{-1}TM_{x+y}\}$ which is isomorphic to C_{4v}, where $r = GR(\hat{z}, \pi/2)$; $M_{f(x,y)}$ represents the spin-orbit coupled reflection with respect to the $f(x,y) = 0$ plane; G is the gauge transformation by $\pi/4$; and G' is the gauge transformation by $\pi/2$. If we remove the time reversal operation, then the symmetry group becomes C_4.

branches of chiral Majorana edge modes. Therefore, the "soft" and "hard" edge pictures on the edge magnetization are fully consistent with each other.

Before proceeding on, we first note that there is no spin magnetization along z-direction for a uniform system. This can be directly seen by noticing that in the tri-component pairing $s + i\eta_1(e^{i\eta_2\varphi/2}p_x + \eta_3 e^{-i\eta_2\varphi/2}p_y)$, the Cooper pairings always occur between up and down electrons, thereby carry no spin angular momentum S^z.

Next, we study the induced magnetization in the presence of a spatially varying electrical potential. In the linear response theory, this is captured by the response of the spin magnetization density $S^z(\vec{r})$ to an applied electric potential $V(\vec{r})$, as shown by the bubble diagram in Fig. 4.4. Assuming $V(\vec{r})$ to be slowly varying, we will only calculate the results up to linear order in the wavevector $\vec{q}$. The solid lines in Fig. 4.4 represent the fermionic Green's functions $G(i\omega_n, \vec{k})$ in the superconducting state where $\omega_n = (2n+1)\pi T$ ($n \in \mathbb{Z}$) is the fermionic Matsubara frequency, and the dashed lines are the bosonic fields $S^z(\vec{r})$ or $V(\vec{r})$. In the following, we assume that $\vec{r}$ represents the two-dimensional spatial coordinates within the junction interface.

In the momentum space within the BdG formalism, the pairing $\hat{\Delta}(\vec{k})$, the spin density $\hat{S}_z(\vec{q})$, and the particle number density $\hat{\rho}(\vec{q})$ can be represented as

$$\begin{aligned}
\hat{S}^z(\vec{q}) &= \psi^\dagger(\vec{k}+\vec{q})S^z(\vec{q})\psi(\vec{k}), \\
\hat{\rho}^x(\vec{q}) &= \psi^\dagger(\vec{k}+\vec{q})\rho(\vec{q})\psi(\vec{k}), \\
\hat{\Delta}(\vec{k}) &= \psi^\dagger(\vec{k})\Delta(\vec{k})\psi^{\dagger,T}(\vec{k}),
\end{aligned} \tag{4.10}$$

in which $\psi(\vec{k}) = (c_\uparrow(\vec{k}), c_\downarrow(\vec{k}), c_\uparrow^\dagger(-\vec{k}), c_\downarrow^\dagger(-\vec{k}))^T$, and the 4×4 matrix kernels are

$$\begin{aligned}
S^z(\vec{q}) &= \frac{1}{4}\sigma^z\tau^z, \;\; \rho(\vec{q}) = \frac{1}{2}\tau^z, \\
\Delta(\vec{k}) &= -|\Delta_s|\sigma^y\tau^y - \frac{|\Delta_p|}{k_f}\big[(k_x+k_y)\sigma^x\tau^y\cos\frac{\varphi}{2} \\
&\quad +(k_x-k_y)\sigma^x\tau^x\sin\frac{\varphi}{2}\big],
\end{aligned} \tag{4.11}$$

in which τ^j ($j = x, y, z$) are the Pauli matrices in the Nambu space, and the tri-component structure $s + i(e^{i\frac{\varphi}{2}} p_x + e^{-i\frac{\varphi}{2}} p_y)$ is assumed. For simplicity, we take a rotationally invariant band dispersion $\xi(\vec{k}) = \frac{\hbar^2}{2m}(k^2 - k_f^2)$. Using the Green's function

$$G(i\omega_n, \vec{k}) = \frac{1}{i\omega_n - \xi(\vec{k})\tau^z - \Delta(\vec{k})}, \tag{4.12}$$

the diagram in Fig. 4.4 can be evaluated as

$$\begin{aligned} \chi(\vec{q}) &= -\int \frac{d^2k}{(2\pi)^2} \frac{1}{\beta} \sum_{i\omega_n} \mathrm{Tr}[S_z G(i\omega_n, \vec{k} + \vec{q}) V G(i\omega_n, \vec{k})] \\ &= \chi_0(iq_x + iq_y), \end{aligned} \tag{4.13}$$

in which within the limit $|\Delta_s|, |\Delta_p| \ll T$ (i.e., close to the superconducting transition temperature), χ_0 is calculated to be

$$\chi_0 \approx \frac{7\zeta(3)}{8\sqrt{2}\pi^2} N_F \frac{1}{T^2} \frac{|\Delta_p \Delta_s|}{k_f} \cos\frac{\varphi}{2}, \tag{4.14}$$

where ζ, N_F, and T are the Riemann zeta function, the density of states at Fermi level, and the temperature, respectively. In Eq. (4.13), the $\vec{q}$-independent terms vanish and only the terms linear in $\vec{q}$ are kept. Detailed calculations are included in Appendix 4.B.

The form of $\chi(\vec{q})$ in Eq. (4.13) implies the following response relation in real space,

$$S^z(\vec{r}) = \chi_0(\partial_x V + \partial_y V) = \sqrt{2}\chi_0 \hat{n}_0 \cdot \nabla V, \tag{4.15}$$

in which $\hat{n}_0 = \frac{1}{\sqrt{2}}(1, 1, 0)$. As is clear from Eq. (4.15), the response is anisotropic since there is a special direction $\hat{n}_0$, which is simply a consequence of the breaking of the C_4 symmetry. Also notice that the two sides of Eq. (4.15) are both invariant under the unbroken symmetry transformation TM_{x-y}. Indeed, the invariance under TM_{x-y} is able to completely determine $\hat{n}_0$ to

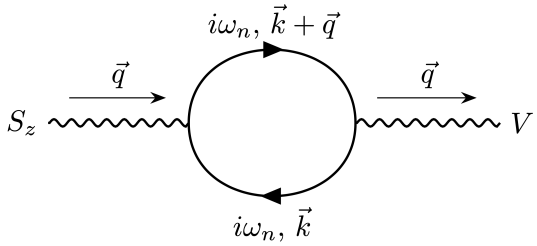

Figure 4.4: The Feynman diagram for the response of the spin magnetization S^z to an external static electric potential V.

be parallel with the (110)-direction.

Finally we note that the edge can be modeled by a change of the electric potential. The potential in the vacuum side is higher than the Fermi energy in the bulk so that the electrons in the vacuum are completely depleted. Consider a "soft" edge where the electric potential varies slowly. Since $\nabla V = |\vec{\nabla} V|(\cos\theta, \sin\theta, 0)$ is parallel to the normal direction of the edge, it is clear from Eq. (4.15) that a spin magnetization emerges on the edge. For a rough estimation, $|\vec{\nabla} V|$ can be approximated as $\sim \varepsilon_f/\xi_c$, where $\varepsilon_f = \frac{\hbar^2}{2m}k_f^2$ is the Fermi energy and ξ_c is the coherence length. Therefore the edge magnetization along the z-axis can be estimated as

$$S_z(\theta) \sim \sqrt{2}\chi_0 \frac{\varepsilon_f}{\xi_c}(\cos\theta + \sin\theta)\,, \tag{4.16}$$

which is highly dependent on the normal direction of the edge. Assuming the edge to be in a circular shape, the edge magnetization along the z-direction is illustrated in Fig. 4.5, where the height of the red arrows indicate the strength of the spin polarizations.

4.4 Edge state picture of the edge magnetization

In this section, we consider a "hard" edge which is assumed to be an infinite straight line. The system lies on one side of the edge, and the other side is the vacuum. The boundary condition is taken such that the wavefunction vanishes at the edge and in the vaccum. We show that the

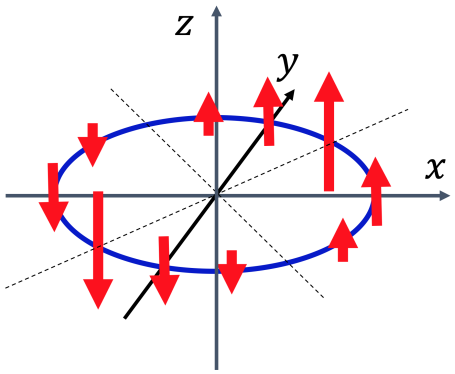

Figure 4.5: The anisotropic edge magnetization on a circular boundary of the junction. The edge is represented by the blue circle. The direction and magnitude of the edge magnetization are represented by the direction and height of the red arrows, respectively.

edge magnetization discussed in Sec. 4.3 with a "soft" edge can alternatively be understood in the edge state picture.

For simplification of discussions, we perform a rotation of the coordinate system defined as

$$\begin{pmatrix} x \\ y \end{pmatrix} = \begin{pmatrix} \cos\theta & -\sin\theta \\ \sin\theta & \cos\theta \end{pmatrix} \begin{pmatrix} x' \\ y' \end{pmatrix}. \tag{4.17}$$

In the rotated basis, $\hat{x}'$ is along the normal direction $\hat{n} = \hat{x}\cos\theta + \hat{y}\sin\theta$ of the edge, and k'_y is a good quantum number. After the rotation, the superconducting pairing gap function is transformed into

$$\hat{\Delta}' = \frac{1}{k_f}[\Delta'_{px}(-i\partial'_x) + \Delta'_{py}k'_y]\sigma^z i\sigma^y + \Delta_s i\sigma^y, \tag{4.18}$$

in which

$$\begin{aligned} \Delta'_{p\nu} &= |\Delta_p|[(\cos\theta + \sin\theta)\cos\frac{\varphi}{2} \\ &\quad + \varepsilon(\nu) i(\cos\theta - \sin\theta)\sin\frac{\varphi}{2}], \end{aligned} \tag{4.19}$$

where $\nu = x, y$, and $-\varepsilon(x) = \varepsilon(y) = 1$. To further simplify the problem, a gauge transformation

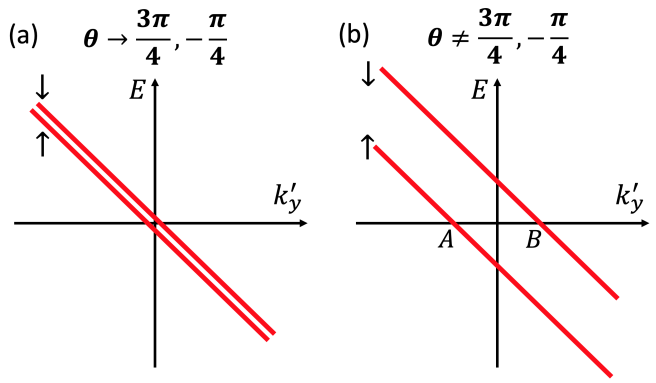

Figure 4.6: Dispersions of the chiral edge Majorana modes for (*a*) $\theta = \frac{3\pi}{4}, -\frac{\pi}{4}$ and (*b*) $\theta \neq \frac{3\pi}{4}, -\frac{\pi}{4}$, where $\theta \in [-\pi, \pi]$.

can be performed to absorb the phase of Δ'_{px}. Then the pairing acquires the form

$$\hat{\Delta}'' = \frac{1}{k_f}[\Delta''_{px}(-i\partial'_x) + \Delta''_{py}k'_y]\sigma^z i\sigma^y + \Delta''_s i\sigma^y, \tag{4.20}$$

in which

$$\begin{aligned} \Delta''_{px} &= |\Delta_p|\sqrt{1+\sin(2\theta)\cos\varphi}, \\ \Delta''_{py} &= |\Delta_p|\frac{\cos(2\theta)\cos\varphi + i\sin\varphi}{\sqrt{1+\sin(2\theta)\cos\varphi}}, \\ \Delta''_s &= i\Delta_s\frac{\cos\frac{\varphi}{2}(\cos\theta+\sin\theta) + i\sin\frac{\varphi}{2}(\cos\theta-\sin\theta)}{\sqrt{1+\sin(2\theta)\cos\varphi}}. \end{aligned} \tag{4.21}$$

In what follows, we assume that the junction occupies the $x' < 0$ region, whereas $x' > 0$ is the vacuum. The boundary condition is taken such that the wavefunction vanishes when $x' \geq 0$.

The general solutions of the edge states are rather complicated. To illustrate the essential physics, it is enough to consider the limit $|\Delta_s| \ll |\Delta_p|$. The strategy is first solving the edge states for $k'_y = 0$, and then a nonzero k'_y can be included using a $k \cdot p$ perturbation method. In the absence of the *s*-wave component, there are two Majorana zero modes localized around the boundary for $k'_y = 0$. In the weak pairing limit $|\Delta_p| \ll \varepsilon_f$, the wavefunctions of the two zero modes can be

solved as [147]

$$\begin{aligned}\Phi_{\uparrow}(x') &= (e^{-i\frac{\pi}{4}},0,0,e^{i\frac{\pi}{4}})^T u(x),\\ \Phi_{\downarrow}(x') &= (0,e^{-i\frac{\pi}{4}},e^{i\frac{\pi}{4}},0)^T u(x),\end{aligned} \tag{4.22}$$

in which $u(x)=\frac{1}{\sqrt{N}}\sin(k_f x)e^{\frac{m|\Delta_p|}{\hbar k_f}x}$, where N is a normalization factor. Since $|\Delta_s| \ll |\Delta_p|$, the s-wave pairing can be treated using a first order perturbation. It is straightforward to verify that the projection of $\hat{\Delta}_s$ (defined in Eq. (4.2)) to the basis $\{\Phi_{\uparrow},\Phi_{\downarrow}\}$ is $-(\mathrm{Im}\Delta_s'')s^z$, where s^{α} ($\alpha = x,y,z$) are the Pauli matrices in the space spanned by $\{\Phi_{\uparrow},\Phi_{\downarrow}\}$, and $\mathrm{Im}\Delta_s''$ can be read from Eq. (4.22). Therefore, while the Majorana modes remain at zero energy under the real part of Δ_s'', the imaginary part of Δ_s'' opens a gap on the edge.

Next we move to a nonzero k_y'. The $k\cdot p$ Hamiltonian can be obtained by projecting the pairing along the y'-direction to the basis $\{\Phi_{\uparrow},\Phi_{\downarrow}\}$, and the result is $-\frac{\mathrm{Im}\Delta_{py}''}{k_f}k_y's^0$ where s^0 is the 2×2 identity matrix. Combining with the contribution from the $\mathrm{Im}\Delta_s''$ term, the dispersions of the two chiral Majorana edge fermions can be derived as

$$E_{\eta}(k_y') = -\frac{\mathrm{Im}\Delta_{py}''}{k_f}k_y' - \eta\mathrm{Im}\Delta_s'', \tag{4.23}$$

in which $E_{\eta}(k_y')$ is the dispersion of the η-branch of the chiral modes, where $\eta = 1$ (-1) for $\uparrow$ $(\downarrow)$. Therefore, when an s-wave component is present in the pairing, the two edge modes split by an energy gap $\Delta E = 2\mathrm{Im}\Delta_s''$. Since $\mathrm{Im}\Delta_s''$ vanishes when $\theta = 3\pi/4, -\pi/4$, the spin up and down chiral branches coincide with each other as shown in Fig. 4.6. When $\theta \neq 3\pi/4, -\pi/4$, the two branches split due to the opening of the gap as shown in Fig. 4.6 (b).

The two branches of chiral Majorana edge modes are spin polarized. As can be seen from Eq. (4.23), within the approximation of a linear dispersion, the occupation range of k_y' for the λ-branch of the chiral mode is $\varepsilon_{\lambda}\frac{\mathrm{Im}\Delta_s''}{\mathrm{Im}\Delta_{py}''}k_f \leq k_y' \leq k_f$, in which $\varepsilon_{\lambda} = 1$ (-1) for $\lambda = \uparrow$ $(\downarrow)$. This leads to an imbalance in the occupation range between the up and down chiral edge modes

corresponding to the line segment between the points A and B in Fig. 4.6 (b). As a consequence, a spin polarization develops on the edge, which has a direction-dependence proportional to $\mathrm{Im}\Delta_s''/\mathrm{Im}\Delta_y'' \sim (\sin\theta + \cos\theta)$. In particular, this result is consistent with what have been obtained in Sec. 4.3 as shown in Fig. 4.5. Thus we see that the "soft" and "hard" edge pictures on the edge magnetization are fully consistent with each other.

Finally we also note that experiments on the anisotropic effect of the edge magnetization in the heterojunction could be potentially useful for testing the gap function symmetries of unconventional superconductors.

4.5 Conclusions

In conclusion, we have studied the heterjunction with one side possessing the chiral p-wave (i.e., $p_x \pm ip_y$) and the other side the conventional s-wave pairing gap functions, respectively. By employing a Ginzburg-Landau free energy analysis, the pairing gap function in the junction region is shown to exhibit a frustrated tri-component structure as $s + i\eta_1(e^{i\eta_2\varphi/2}p_x + \eta_3 e^{-i\eta_2\varphi/2}p_y)$, where φ is the phase difference between the p_x and p_y components, and $\eta_j = \pm 1$ $(j = 1,2,3)$. By solving the chiral Majorana edge modes with the tri-component pairing, we find that the edge of the junction carries an anisotropic spin magnetization, where the anisotropy originates from the breaking of the rotational symmetry. In addition, the edge magnetization is consistent with a novel type of anisotropic magnetoelectric effect, which is analyzed through the linear response calculation.

4.A The Ginzburg-Landau free energy

For simplicity, we will consider a system with isotropic Fermi surface. As a result, the β'_p term vanishes. Only keeping the spatially uniform parts, the free energy up to quartic orders is

$$\begin{aligned} f_{spp} =& \alpha_s|\Delta_s|^2 + \alpha_p(|\Delta_{px}|^2 + |\Delta_{py}|^2) + \beta_s|\Delta_s|^4 + \beta_p(|\Delta_{px}|^4 + |\Delta_{py}|^4) \\ &+ g_{pp}[(\Delta^*_{px}\Delta_{py})^2 + (\Delta^*_{py}\Delta_{px})^2] + \nu_p|\Delta_{px}|^2|\Delta_{py}|^2 \\ &+ \gamma_1(|\Delta_{px}|^2 + |\Delta_{py}|^2)|\Delta_s|^2 + g_{sp}[\Delta^{*2}_s(\Delta^2_{px} + \Delta^2_{py}) + \Delta^2_s(\Delta^{*2}_{px} + \Delta^{*2}_{py})]. \end{aligned} \tag{4.24}$$

While the coefficients of the quadratic terms depend on the interactions which rely on the details of the pairing mechanism, the coefficients of the quartic terms are not dependent on the interaction strength within a tree-level approximation and can be determined from the diagrams in Fig. 4.7, in which the the superconducting order parameters are given by

$$\begin{aligned} \hat{\Delta}_s &= \frac{\Delta_s}{2}\sum_k c^\dagger_k i\sigma^y (c^\dagger_{-k})^T, \\ \hat{\Delta}_{px} &= \frac{\Delta_{px}}{2k_f}\sum_k c^\dagger_k (k_x\sigma^z) i\sigma^y (c^\dagger_{-k})^T, \\ \hat{\Delta}_{py} &= \frac{\Delta_{py}}{2k_f}\sum_k c^\dagger_k (k_y\sigma^z) i\sigma^y (c^\dagger_{-k})^T, \end{aligned} \tag{4.25}$$

where $c^\dagger_k = (c^\dagger_{k\uparrow}\ c^\dagger_{k\downarrow})$ is a two-component row vector.

Keeping only the static and uniform terms (i.e., zero frequency and zero momentum), we

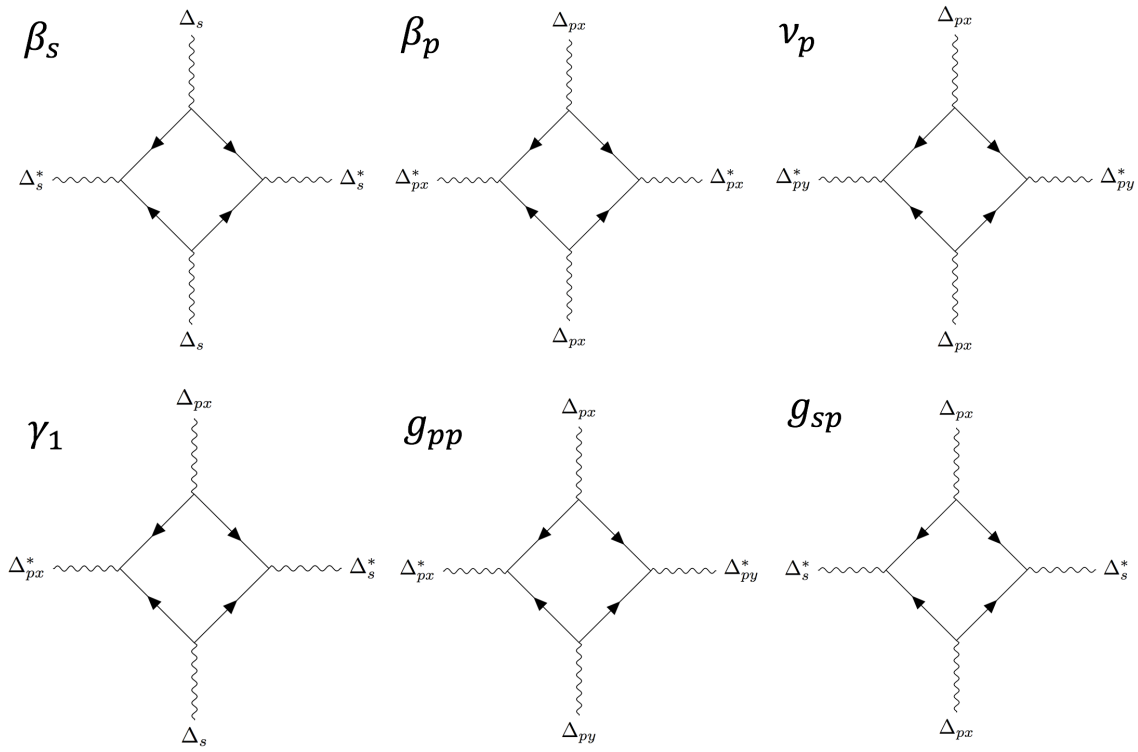

Figure 4.7: Diagrams determining the coefficients in the Ginzburg-Landau free energy.

obtain

$$
\begin{aligned}
\beta_s &= \frac{3}{2}\hat{\beta}_0 \mathrm{Tr}\{(i\sigma^y)^\dagger (i\sigma^y)(i\sigma^y)^\dagger (i\sigma^y)\}, \\
\beta_p &= \frac{3}{2}\hat{\beta}_0 \frac{1}{k_f^4} \mathrm{Tr}\{(ik_\alpha \sigma^z\sigma^y)^\dagger (ik_\alpha \sigma^z\sigma^y)(ik_\alpha \sigma^z\sigma^y)^\dagger (ik_\alpha \sigma^z\sigma^y), \\
\nu_p &= 6\hat{\beta}_0 \frac{1}{k_f^4} \mathrm{Tr}\{(ik_x \sigma^z\sigma^y)^\dagger (ik_x \sigma^z\sigma^y)(ik_y \sigma^z\sigma^y)^\dagger (ik_y \sigma^z\sigma^y), \\
\gamma_1 &= 6\hat{\beta}_0 \frac{1}{k_f^2} \mathrm{Tr}\{(ik_\alpha \sigma^z\sigma^y)^\dagger (ik_\alpha \sigma^z\sigma^y)(i\sigma^y)^\dagger (i\sigma^y)\}, \\
g_{pp} &= \frac{3}{2}\hat{\beta}_0 \frac{1}{k_f^4} \mathrm{Tr}\{(ik_x \sigma^z\sigma^y)^\dagger (ik_y \sigma^z\sigma^y)(ik_x \sigma^z\sigma^y)^\dagger (ik_y \sigma^z\sigma^y)\}, \\
g_{sp} &= 6\hat{\beta}_0 \frac{1}{k_f^2} \mathrm{Tr}\{(i\sigma^y)^\dagger (ik_\alpha \sigma^z\sigma^y)(i\sigma^y)^\dagger (ik_\alpha \sigma^z\sigma^y))\}, \qquad (4.26)
\end{aligned}
$$

in which k_α can be taken as either k_x or k_y, and the operation $\hat{\beta_0}$ acting on the expression to the

right of it is defined as

$$\hat{\beta}_0[\cdots] = \frac{1}{\beta}\frac{1}{L^3}\sum_{\omega_m,k}\frac{1}{(\omega_m^2+\xi_k^2)^2}[\cdots], \tag{4.27}$$

where $\xi_k = \hbar^2k^2/2m - \varepsilon_F$, and L^3 is the volume of the system. In the weak pairing limit, a linearization of the dispersion can be performed. Changing the integration over $\vec{k}$ to spherical coordinates, we have

$$\hat{\beta}_0[\cdots] = N_F\frac{1}{\beta}\sum_n\int_{-\infty}^{\infty}d\varepsilon\int_0^{\pi}\sin\theta d\theta\int_0^{2\pi}d\phi\frac{1}{\left([(2n+1)\pi/\beta]^2+\varepsilon^2\right)^2}[\cdots], \tag{4.28}$$

in which N_F is the density of states at Fermi energy.

Plugging Eq. (4.28) into Eq. (4.26), performing the integrations, and summing over the Matsubara frequencies, we obtain

$$\beta_s = \frac{3}{2}\beta,\ \beta_p = \frac{3}{10}\beta,\ \nu_p = \frac{2}{5}\beta,\ \gamma_1 = 2\beta,\ g_{pp} = \frac{1}{10}\beta,\ g_{sp} = 2\beta. \tag{4.29}$$

in which

$$\beta = \frac{7\zeta(3)N_F}{8\pi^2T^2}. \tag{4.30}$$

Notice that since $2(\beta_p - g_{pp}) = \nu_p$, the p-wave terms in Eq. (4.24) can be recombined into the form in Eq. (4.1).

Finally we note that the coefficients determined in this section are not accurate in real situations, since there are notable renormalization effects, particularly when T is close to T_c.

4.B The linear response of the anisotropic magnetoelectric effect

We work in the ordered phase and calculate the correlation function between S^z and ρ. In the following calculations, we take the pairing as $-is + e^{i\varphi/2}p_x + e^{-i\varphi/2}p_y$. The pairing is taken as

$$\frac{\Delta_p}{k_f}(e^{i\varphi/2}k_x + e^{-i\varphi/2}k_y)\sigma^z i\sigma^y - i\Delta_s i\sigma^y\,, \tag{4.31}$$

in which both Δ_p and Δ_s are real and positive. In the spin up sector, the BdG Hamiltonian is of the form

$$H_\uparrow(\vec{k}) = \xi(\vec{k})\iota^z + \frac{\Delta_p}{k_f}\cos(\frac{\varphi}{2})(k_x+k_y)\iota^x + \big[\frac{\Delta_p}{k_f}\sin(\frac{\varphi}{2})(k_y-k_x)) + \Delta_s\big]\iota^y\,. \tag{4.32}$$

Since the spin up and down sectors are related by a particle-hole transformation, it is enough to work in the spin up sector. We also note that the matrix kernels for S^z and ρ in the spin up sector are ι^z and $\frac{1}{2}\iota^0$, respectively, where ι^0 is the 2×2 identity matrix. In what follows, we write ι^α as σ^α ($\alpha = 0, x, y, z$) for simplicity.

In the imaginary time formalism with, the diagram in Fig. 4.4 can be evaluated as

$$\begin{aligned}
\chi(\vec{q}) =& -\int \frac{d^2\vec{k}}{(2\pi)^2}\frac{1}{\beta}\sum_{i\omega_n}\mathrm{tr}\big[\frac{1}{2}\sigma^0\frac{1}{i\omega_n - H_\uparrow(\vec{k}+\vec{q})}\sigma^3\frac{1}{i\Omega_n - H_\uparrow(\vec{k})}\big] \\
=& -\int \frac{d^2\vec{k}}{(2\pi)^2}\frac{1}{\beta}\sum_{i\omega_n}\frac{1}{D(\vec{k},\vec{q},\omega_n)} \\
& \times \frac{1}{\omega_n^2 + \xi^2(\vec{k}) + \frac{\Delta_p^2}{k_f^2}\cos^2(\frac{\varphi}{2})(k_x+k_y)^2 + \big[\frac{\Delta_p}{k_f}\sin(\frac{\varphi}{2})(-k_x+k_y)+\Delta_s\big]^2} \\
& \times \mathrm{tr}\Big[\frac{\sigma^0}{2}\big(i\omega_n + \xi(\vec{k}+\vec{q})\sigma^z + \frac{\Delta_p}{k_f}\cos(\frac{\varphi}{2})(k_x+q_x+k_y+q_y)\sigma^x + \\
& [\frac{\Delta_p}{k_f}\sin(\frac{\varphi}{2})(-k_x-q_x+k_y+q_y)+\Delta_s]\sigma^y\big) \\
& \cdot\sigma^z\big(i\omega_n + \xi(\vec{k}) + \frac{\Delta_p}{k_f}\cos(\frac{\varphi}{2})(k_x+k_y)\sigma^x \\
& + [\frac{\Delta_p}{k_f}\sin(\frac{\varphi}{2})(-k_x+k_y)+\Delta_s]\sigma^y\big)\Big],
\end{aligned} \tag{4.33}$$

with

$$\begin{aligned}
D(\vec{k},\vec{q},\omega_n) =& \omega_n^2 + \xi^2(\vec{k}+\vec{q}) + \frac{\Delta_p^2}{k_f^2}\cos^2(\frac{\varphi}{2})(k_x+q_x+k_y+q_y)^2 \\
& + \Big[\frac{\Delta_p}{k_f}\sin(\frac{\varphi}{2})(-k_x-q_x+k_y+q_y)+\Delta_s\Big]^2.
\end{aligned} \tag{4.34}$$

The trace term in Eq. (4.33) can be evaluated to be

$$\mathrm{tr}[\cdots] = -i\frac{\Delta_p}{k_f}\cos(\frac{\varphi}{2})\big[q_x(\frac{2\Delta_p}{k_f}\sin(\frac{\varphi}{2})k_y+\Delta_s) + q_y(-\frac{2\Delta_p}{k_f}\sin(\frac{\varphi}{2})k_x+\Delta_s)\big], \tag{4.35}$$

in which the linear in ω_n terms are neglected since they sum to zero after Matsubara frequency summation. Since the numerator of Eq. (4.33) is already linear in $\vec{q}$, the $\vec{q}$'s in the denominator can be set to be zero since we only need the results up to $O(\vec{q})$. Then we arrive at

$$\chi(\vec{q}) = iq_x\chi_x + iq_y\chi_y, \tag{4.36}$$

in which

$$\chi_x = \int \frac{d^2\vec{k}}{(2\pi)^2} \sum_{i\omega_n} \frac{\frac{1}{\beta}\frac{\Delta_p}{k_f}\cos(\frac{\varphi}{2})(\frac{2\Delta_p}{k_f}\sin(\frac{\varphi}{2})k_y + \Delta_s)}{\omega_n^2 + \xi_{\vec{k}}^2 + \frac{\Delta_p^2}{k_f^2}\cos^2(\frac{\varphi}{2})(k_x+k_y)^2 + \left[\frac{\Delta_p}{k_f}\sin(\frac{\varphi}{2})(k_y-k_x) + \Delta_s\right]^2},$$
$$\chi_y = \int \frac{d^2\vec{k}}{(2\pi)^2} \sum_{i\omega_n} \frac{-\frac{1}{\beta}\frac{\Delta_p}{k_f}\cos(\frac{\varphi}{2})(\frac{2\Delta_p}{k_f}\sin(\frac{\varphi}{2})k_x + \Delta_s)}{\omega_n^2 + \xi_{\vec{k}}^2 + \frac{\Delta_p^2}{k_f^2}\cos^2(\frac{\varphi}{2})(k_x+k_y)^2 + \left[\frac{\Delta_p}{k_f}\sin(\frac{\varphi}{2})(k_y-k_x) + \Delta_s\right]^2}. \tag{4.37}$$

Next to simplify the expressions of χ_x and χ_y, we perform a change of variable

$$k'_x = \frac{1}{\sqrt{2}}(k_x + k_y),\ k'_y = \frac{1}{\sqrt{2}}(-k_x + k_y). \tag{4.38}$$

Then we have

$$\chi_x = A_x + A_y + A_s,\ \chi_y = -A_x + A_y + A_s, \tag{4.39}$$

in which

$$A_\alpha = \int \frac{d^2\vec{k}'}{(2\pi)^2} \sum_{i\omega_n} \frac{\frac{1}{\beta}\frac{\Delta_p}{k_f}\cos(\frac{\varphi}{2})\frac{\sqrt{2}\Delta_p}{k_f}\sin(\frac{\varphi}{2})k'_\alpha}{\omega_n^2 + \xi^2(\vec{k}') + \frac{2\Delta_p^2}{k_f^2}\cos^2(\frac{\varphi}{2})k_x'^2 + \left[\frac{\sqrt{2}\Delta_p}{k_f}\sin(\frac{\varphi}{2})k'_y + \Delta_s\right]^2},$$
$$A_s = \int \frac{d^2\vec{k}'}{(2\pi)^2} \sum_{i\omega_n} \frac{\frac{1}{\beta}\frac{\Delta_p}{k_f}\cos(\frac{\varphi}{2})\Delta_s}{\omega_n^2 + \xi^2(\vec{k}') + \frac{2\Delta_p^2}{k_f^2}\cos^2(\frac{\varphi}{2})k_x'^2 + \left[\frac{\sqrt{2}\Delta_p}{k_f}\sin(\frac{\varphi}{2})k'_y + \Delta_s\right]^2}, \tag{4.40}$$

in which $\alpha = x, y$. Clearly, A_α ($\alpha = x, y$) vanishes since the numerator is odd under the integration over $\int dk'_\alpha$.

In the limit $\Delta_s, \Delta_p \ll T$, the dependence on the order parameters in the denominators of A_s can be neglected, and we have

$$\chi_x = \chi_y \approx \frac{\Delta_p \Delta_s}{\sqrt{2}k_f}\cos(\frac{\varphi}{2})\int \frac{d^2\vec{k}}{(2\pi)^2}\frac{1}{\beta}\sum_{i\omega_n}\frac{1}{(\omega_n^2 + \xi^2(\vec{k}))^2}. \tag{4.41}$$

The integral can be evaluated as

$$\begin{aligned}\int \frac{d^2\vec{k}}{(2\pi)^2}\frac{1}{\beta}\sum_{i\omega_n}\frac{1}{(\omega_n^2+\xi^2(\vec{k}))^2} =& N_0\frac{1}{\beta}\sum_{i\omega_n}\int d\varepsilon\frac{1}{(\omega_n^2+\varepsilon^2)^2}\\ =& N_0\frac{1}{\beta}\sum_{n\in\mathbb{Z}}\frac{\pi}{2}\frac{1}{|2\pi n/T|^3} = \frac{7\zeta(3)}{8\pi^2}N_0\frac{1}{T^2}\,,\end{aligned} \tag{4.42}$$

in which ζ is the Riemann zeta function.

In summary, in the limit $\Delta_s, \Delta_p \ll T$, the response is

$$S^z = \chi_0(\partial_x V + \partial_y V), \tag{4.43}$$

in which

$$\chi_0 = \frac{7\zeta(3)}{8\sqrt{2}\pi^2}N_0\frac{1}{T^2}\frac{\Delta_p\Delta_s}{k_f}\cos(\frac{\varphi}{2}). \tag{4.44}$$

This chapter is a reprint of the following preprint being prepared for submission for publication: 'C. Xu, W. Yang, and C. Wu, **Superconducting junction with tri-component pairing gap functions**. *arXiv:2010.05362*' [166]. The dissertation author was the primary investigator and author of this paper.

Chapter 5

Axion Dynamics in $p + is$ Superconductor

5.1 Introduction

Spin triplet superconductivity and paired superfluidity have a complex spin-orbit entangled structure in the Cooper pair wavefunctions [167, 168, 169, 102, 170], leading to exotic behaviors like topological properties [171, 172, 173, 174, 175, 176]. Another interesting type of Cooper pairing is the one with spontaneous time reversal symmetry breaking, which arises when two or more channels of pairing instabilities compete and coexist [121, 122, 124, 123, 98, 125, 126, 90, 127, 128, 145, 146, 147, 148, 177, 150, 151, 152, 153, 154, 156, 157, 158, 159, 160, 161, 162, 129, 130, 131, 132, 133, 134, 135, 136, 137, 138, 139, 144]. A mixture of triplet and singlet Cooper pairings which breaks time reversal symmetry has been theoretically studied in different contexts, showing exotic properties including nontrivial bulk electromagnetic and gravitational responses [178, 179], quantized surface thermal Hall effects [88, 180, 178, 181], chiral Majorana fermions propagating along the magnetic domain wall on the surface [147], and high order topology [182]. Recently, there has been experimental evidence of triplet pairing gap functions with spontaneous time reversal symmetry breaking in real materials [183, 184].

Axion as an elementary particle was proposed in the high energy context more than four

decades ago [185, 186, 187], which has been considered as a candidate for dark matter and dark energy, thought its existence still remains inconclusive. On the other hand, the dynamical axion field has been proposed to exist in topological systems as a condensed matter realization of axions [188, 180, 179]. The coupling between the axion angle θ and the electromagnetic field is of the form $\int d^4x\theta\vec{E}\cdot\vec{B}$ (up to an overall numerical constant factor), resulting in various magnetoelectric effects, where $\vec{E}$ and $\vec{B}$ are the electric and magnetic fields, respectively. In particular, the three-dimensional (3D) $p+is$ superconductor has been considered as a superconducting platform which hosts axion field [179, 189], where the triplet pairing component is invariant under spin-orbit coupled rotations analogous to the pairing of the ^{3}He-B superfluid.

In this work, we perform a systematic derivation of the coupling between the axion angle and the electromagnetic field in $p+is$ superconductors, including the contributions from both the orbital and spin channels. The axion electrodynamics has been already studied in superconducting 3D Dirac and Weyl systems with mixed-parity pairing which breaks time reversal symmetry [179, 190]. On the other hand, we find that there are several differences between the $p+is$ superconductors and the superconducting Dirac/Weyl case. Firstly, the electromagnetic part of the action is not of the $\vec{E}\cdot\vec{B}$ form, but is $\nabla(\phi-\hbar\partial_t\Phi/e)\cdot\vec{B}$, where ϕ and Φ are the electric potential and the superfluid phase, respectively. In particular, the induced electric field $\partial_t\vec{A}/c$ does not appear in the action. The second difference is that the axion angle $\Theta_{\rm ax}$ in the $p+is$ superconductors is not just $\theta_{\rm ax}$, defined as the phase difference between the superconducting phases on the two Fermi surfaces of different helicities. In addition to $\theta_{\rm ax}$, $\Theta_{\rm ax}$ also acquires a sinusoidal term $\sin(\theta_{\rm ax})$. These differences arise from a lack of Lorentz symmetry in $p+is$ superconductors.

5.2 Model hamiltonian

We consider a superconducting 3D centrosymmetric electronic system which exhibits a mixture of singlet and triplet pairing symmetries. The band dispersion is

$$\xi_\alpha(\vec{k}) = \frac{\hbar^2}{2m}k^2 - \varepsilon_F, \tag{5.1}$$

in which $\varepsilon_F = \frac{\hbar^2}{2m}k_f^2$ is the Fermi energy where k_f is the Fermi wavevector, and $\alpha = \uparrow, \downarrow$ is the spin index. The pairing Hamiltonians $\hat{P}_s(\vec{k})$ and $\hat{P}_p(\vec{k})$ for the s-wave and ^{3}He-B like p-wave pairing gap functions are defined as

$$\begin{aligned} \hat{P}_s^\dagger(\vec{k}) &= (i\sigma_2)_{\alpha\beta} c_\alpha^\dagger(\vec{k}) c_\beta^\dagger(-\vec{k}), \\ \hat{P}_p^\dagger(\vec{k}) &= \frac{1}{k_f} k_j (i\sigma_j\sigma_2)_{\alpha\beta} c_\alpha^\dagger(\vec{k}) c_\beta^\dagger(-\vec{k}), \end{aligned} \tag{5.2}$$

respectively, in which: α, β are spin indices; $c_\alpha^\dagger(\vec{k})$ is the electron creation operator with momentum $\vec{k}$ and spin α; σ_j's ($j = 1,2,3$) are the three Pauli matrices in spin space; and repeated indices imply summations. We note that $\hat{P}_p(\vec{k})$ is invariant under spin-orbit coupled SO(3) rotations, which has the same form as the pairing in the ^{3}He-B superfluid [167].

The pattern of the mixed-parity pairing gap function can be determined by a Ginzburg-Landau free energy analysis. Keeping up to quartic terms and neglecting terms involving temporal and spatial derivatives, the most general form of the free energy invariant under both time reversal ($\mathcal{T}$) and inversion ($\mathcal{P}$) symmetries is given by

$$\begin{aligned} F &= -\alpha_s \Delta_s^* \Delta_s - \alpha_p \Delta_p^* \Delta_p + \beta_s |\Delta_s|^4 + \beta_p |\Delta_p|^4 \\ &\quad + \gamma_1 |\Delta_p|^2 |\Delta_s|^2 + \gamma_2 (\Delta_p^* \Delta_p^* \Delta_s \Delta_s + c.c), \end{aligned} \tag{5.3}$$

in which Δ_λ ($\lambda = s, p$) are the pairing gap functions in the λ-channel. When the instabilities in the s-

and p-wave channels coexist, both α_s and α_p are negative. At tree level, the coefficients β_λ, γ_j ($\lambda = s, p,\ j = 1,2$) are all determined by the electronic band structure, independent of the interactions. In particular, close to the superconducting transition point, $\gamma_2 = \frac{5\zeta(3)}{8\pi^2 T_c^2} N_F$ is generically positive [146], where $\zeta(z)$ ($z \in \mathbb{C}$) is the Riemann zeta function; T_c is the superconducting transition temperature (where for simplicity, a degenerate transition temperature for both s- and p-wave channels is assumed); and $N_F = \frac{mk_f}{2\pi^2\hbar^2}$ is the density of states at the Fermi level for a single spin component. An important implication of a positive γ_2 is that a relative $\pi/2$ phase difference between Δ_s and Δ_p is energetically favorable as can be readily seen from Eq. (5.3), leading to a superconducting pairing of the $p \pm is$ form. Notice that the $p \pm is$ pairing spontaneously breaks both time reversal and inversion symmetries, but remains invariant under the combined $\mathcal{PT}$-operation up to an overall gauge transformation [147]. We note that in addition to the intrinsic $p \pm is$ superconductors, the $p \pm is$ pairing symmetry can also be realized via proximity effects, as discussed in Ref. [147].

In the remaining parts of this article, $|\Delta_\lambda|$ is denoted as Δ_λ for short, and the $\pi/2$ superconducting phase difference will be explicitly displayed by considering the $p + is$ pairing Hamiltonian $\Delta_p \hat{P}_p^\dagger(\vec{k}) + i\Delta_s \hat{P}_s^\dagger$. In the Bogoliubov-de-Gennes (BdG) formalism, the mean field Hamiltonian acquires the form

$$H_{\mathrm{BdG}} = \frac{1}{2} \sum_{\vec{k}} \Psi^\dagger(\vec{k}) H(\vec{k}) \Psi(\vec{k}), \tag{5.4}$$

in which

$$\Psi^\dagger(\vec{k}) = (c_\uparrow^\dagger(\vec{k})\ c_\downarrow^\dagger(\vec{k})\ c_\uparrow(-\vec{k})\ c_\downarrow(-\vec{k})), \tag{5.5}$$

and the matrix kernel $H(\vec{k})$ is

$$H(\vec{k}) = (\frac{\hbar^2}{2m}k^2 - \varepsilon_F)\gamma^0 + \frac{\Delta_p}{k_f}\vec{k}\cdot\vec{\gamma} + \Delta_s\gamma^4, \tag{5.6}$$

in which $\vec{\gamma} = (\gamma^1, \gamma^2, \gamma^3)$, and the matrices γ^μ ($\mu = 0,1,2,3,4$) are defined as

$$\gamma^0 = \sigma_0\tau_3, \gamma^1 = -\sigma_3\tau_1, \gamma^2 = -\sigma_0\tau_2, \gamma^3 = \sigma_1\tau_1, \gamma^4 = \sigma_2\tau_1, \tag{5.7}$$

where τ^i ($i = 1,2,3$) are the Pauli matrices in the Nambu space, and σ_0 and τ_0 denote the 2×2 identity matrices in the spin and Nambu spaces, respectively. It can be straightforwardly verified that the five gamma-matrices γ^μ ($\mu = 0,1,2,3,4$) satisfy the anticommutation relations

$$\{\gamma^\mu, \gamma^\nu\} = 2\delta_{\mu\nu}. \tag{5.8}$$

Later we will also consider spatially and temporally varying pairing gap functions $\Delta_\lambda(\vec{r},t)$ ($\lambda = s,p$). Including the minimal coupling to electromagnetic potentials $\{A^\mu\}_{\mu=0,1,2,3}$, the Hamiltonian in real space becomes

$$H_{\rm BdG} = \frac{1}{2}\int d^3r \sum_{\vec{r}} \Psi^\dagger(\vec{r})\hat{T}^\rho\gamma^\rho\Psi(\vec{r}), \tag{5.9}$$

in which the summation is over $\rho = 0,1,2,3,4$; $\Psi^\dagger(\vec{r})$ is the Fourier transform of $\Psi^\dagger(\vec{k})$; and

$$\begin{aligned}
\hat{T}^0 &= \frac{\hbar^2}{2m}(-i\nabla + \frac{e}{c}\vec{A})^2 - \mu(\vec{r}), \\
\hat{T}^j &= \frac{1}{2k_f}\{\Delta_p(\vec{r},t), -i\partial_j\}\gamma^j, \ (j = 1,2,3), \\
\hat{T}^4 &= \Delta_s(\vec{r},t).
\end{aligned} \tag{5.10}$$

In addition to Eq. (5.9), there is also a Zeeman term in the presence of a magnetic field, i.e.,

$$H_{\mathrm{ZM}} = \frac{1}{2} g\mu_B \int d^3r \sum_{\vec{r}} \Psi^\dagger(\vec{r})[-\frac{i}{2}\varepsilon_{ijk} B_i \gamma^j \gamma^k]\Psi(\vec{r}), \tag{5.11}$$

in which g is the Landé factor, μ_B is the Bohr magneton, $\vec{B} = \frac{1}{c}\nabla \times \vec{A}$ is the magnetic field, and the $1/2$ factor in the front comes from the spin-$1/2$ nature of the electrons.

5.3 Transverse supercurrent in the presence of spatial inhomogeneities

In this section, we perform a quick real space calculation of the transverse supercurrent induced by static electric field and spatial inhomogeneity of Δ_s. The corresponding term in the axion action S_{ax} can then be determined from the relation $j_i = -c\frac{\delta S_{ax}}{\delta A_i}$ $(i = 1,2,3)$ where c is the light velocity. Later in Sec. 5.4, we will carry out a systematic path integral calculation. In addition to the supercurrent discussed in this section, there is also bound current originating from the spin magnetic moment which is not related to electron transport, as will be discussed in detail in Sec. 5.6.

In BdG form, the matrix kernel of the operator of the electric current density $j_i(\vec{x})$ $(i = 1,2,3)$ at position $\vec{x}$ is

$$\hat{j}_i(\vec{x}) = -\frac{e\hbar}{4m}\left[\delta(\hat{\vec{r}} - \vec{x})(-i\nabla_{\vec{x}}) + (-i\nabla_{\vec{x}})\delta(\hat{\vec{r}} - \vec{x})\right]\sigma_0\tau_0, \tag{5.12}$$

in which $\hat{\vec{r}}$ is the coordinate operator. The expectation value of $\hat{j}_i(\vec{x})$ is

$$\left\langle \hat{j}_i(\vec{x}) \right\rangle = \mathrm{Tr}(\hat{j}_i(\vec{x})\hat{G}), \tag{5.13}$$

in which the Green's function $\hat{G}$ is

$$\hat{G} = \frac{1}{-\partial_\tau - H}, \tag{5.14}$$

where τ is the imaginary time, and H is the matrix kernel of the Hamiltonian H_{BdG} in the presence of a spatially varying electric potential $\phi(\vec{r})$ and s-wave pairing gap function $\Delta_s(\vec{r})$. We emphasize that the symbol "Tr" denotes the trace operation of an operator, which, in addition to the trace of the matrix structure in the spin and Nambu spaces, also involves the integral over spatial coordinates. In what follows, we use "tr" to indicate the trace which is only taken over the 4×4 matrix structure.

The Green's function $\hat{G}$ can be rewritten as

$$\hat{G} = (-)\frac{1}{-\partial_\tau^2 + H^2}(-\partial_\tau + H). \tag{5.15}$$

The Hamiltonian squared H^2 can be separated as

$$H^2 = H_0^2 + Q, \tag{5.16}$$

in which

$$\begin{aligned} H_0^2 &= \hat{T}^\rho \hat{T}^\rho, \\ Q &= \sum_{0 \le \rho < \sigma \le 4} [\hat{T}^\rho, \hat{T}^\sigma] \gamma^\rho \gamma^\sigma, \end{aligned} \tag{5.17}$$

where $\hat{T}^\rho$ is defined in Eq. (5.10) and the anticommutation relations Eq. (5.8) is used. Straightfor-

ward calculations show that

$$\begin{aligned}
\hat{T}^{\rho}\hat{T}^{\rho} &= [-\frac{\hbar^2}{2m}\nabla^2-\mu(\vec{r})]^2+\frac{\Delta_p^2}{k_f^2}(-\nabla^2)+[\Delta_s(\vec{r})]^2,\\
[\hat{T}^0,\hat{T}^i] &= -i\frac{\Delta_p}{k_f}\partial_i\mu,\\
[\hat{T}^0,\hat{T}^4] &= -\frac{\hbar^2}{2m}(\nabla^2\Delta_s+2\nabla\Delta_s\cdot\nabla),\\
[\hat{T}^i,\hat{T}^4] &= -i\frac{\Delta_p}{k_f}\partial_i\Delta_s,
\end{aligned} \tag{5.18}$$

in which $\mu(\vec{r})=\varepsilon_F+e\phi(\vec{r})$, where $\phi(\vec{r})$ is the electric potential.

Expanding $\left\langle \hat{j}_i(\vec{x})\right\rangle$ in powers of Q, we obtain

$$\begin{aligned}
\left\langle \hat{j}_i(\vec{x})\right\rangle &= \sum_{n=0}^{\infty}(-)^{n+1}\mathrm{Tr}\big[\hat{j}_i(\vec{x})(\frac{1}{-\partial_\tau^2+H_0^2}Q)^n\\
&\quad\times\frac{1}{-\partial_\tau^2+H_0^2}(-\partial_\tau+H)\big].
\end{aligned} \tag{5.19}$$

In what follows, we will only keep terms up to $n=2$.

The $n=0$ term in Eq. (5.19) vanishes: The odd-in-∂_τ term vanishes after Matsubara frequency summation; and the other terms contain a trace of a single γ-matrix, hence are also zero.

The $n=1$ term also vanishes. Removing the odd-in-∂_τ term, the $n=1$ term contains one Δ_H and one H under the trace operation. However, Δ_H and H are products of two and one γ-matrices, respectively. Hence the result vanishes since the trace of a product of three γ-matrices is zero.

Finally we consider the $n=2$ term

$$\begin{aligned}
&\left\langle \hat{j}_i^{(2)}(\vec{x})\right\rangle =\\
&-\mathrm{Tr}\big[\hat{j}_i(\vec{x})\frac{1}{-\partial_\tau^2+H_0^2}Q\frac{1}{-\partial_\tau^2+H_0^2}Q\frac{1}{-\partial_\tau^2+H_0^2}H\big].
\end{aligned} \tag{5.20}$$

To lowest order in the gradient expansion [191], $\mu(\vec{r})$ and $\Delta_s(\vec{r})$ can be taken as constants in H_0 [191]. The only way to have a nonzero trace is a multiplication of all the five γ-matrices. Since the electric current operator $\hat{j}_i(\vec{x})$ contains a $-i\partial_i$, the H term must contribute $\frac{\Delta_p}{k_f}(-i\partial_i)\gamma^i$ so that the trace is nonzero. Therefore,

$$\begin{aligned}\left\langle \hat{j}_i^{(2)}(\vec{x})\right\rangle = 2(\tfrac{\Delta_p}{k_f})^3 \mathrm{Tr}\big[\hat{j}_i(\vec{x})\tfrac{1}{-\partial_\tau^2+H_0^2}\partial_j\mu\tfrac{1}{-\partial_\tau^2+H_0^2}\partial_k\Delta_s \\ \times\tfrac{1}{-\partial_\tau^2+H_0^2}(-i\partial_i)\big]\mathrm{tr}(\gamma^0\gamma^j\gamma^k\gamma^4\gamma^i),\end{aligned} \tag{5.21}$$

in which the trace of the product of five γ-matrices can be easily evaluated using

$$\mathrm{tr}(\gamma^0\gamma^i\gamma^j\gamma^k\gamma^4) = -4\varepsilon_{ijk}. \tag{5.22}$$

Using Eq. (5.12), $\left\langle \hat{j}_i^{(2)}(\vec{x})\right\rangle$ can be evaluated as

$$\begin{aligned}\left\langle \hat{j}_i^{(2)}(\vec{x})\right\rangle &= -\varepsilon_{ijk}\frac{2e\hbar}{m}(\frac{\Delta_p}{k_f})^3\int d\vec{y}d\vec{z} \\ &\big\{\langle\vec{x}|(-i\partial_i)\frac{1}{-\partial_\tau^2+H_0^2}|\vec{y}\rangle\partial_j\mu(\vec{y})\langle\vec{y}|(-i\partial_i)\frac{1}{-\partial_\tau^2+H_0^2}|\vec{z}\rangle \\ &\quad\times\partial_k\Delta_s(\vec{z})\langle\vec{z}|\frac{1}{-\partial_\tau^2+H_0^2}(-i\partial_i)|\vec{x}\rangle \\ &+\langle\vec{x}|\frac{1}{-\partial_\tau^2+H_0^2}|\vec{y}\rangle\partial_j\mu(\vec{y})\langle\vec{y}|\frac{1}{-\partial_\tau^2+H_0^2}|\vec{z}\rangle\partial_k\Delta_s(\vec{z}) \\ &\quad\times\langle\vec{z}|\frac{1}{-\partial_\tau^2+H_0^2}(-i\partial_i)^2|\vec{x}\rangle\big\}.\end{aligned} \tag{5.23}$$

In momentum space, Eq. (5.23) becomes

$$\begin{aligned}\left\langle \hat{j}_i^{(2)}(\vec{x})\right\rangle &= -\varepsilon_{ijk}\frac{2e\hbar}{m}(\frac{\Delta_p}{k_f})^3 \\ &\times \frac{1}{\beta}\sum_{\omega_n}\int d\vec{y}d\vec{z}\partial_j\mu(y)\partial_k\Delta_s(z)\left[\Pi_{\alpha=1}^3\int\frac{d\vec{k}_\alpha}{(2\pi)^3}\right] \\ &\times (k_{1i}k_{3i}+k_{3i}^2)\left[\Pi_{\alpha=1}^3\frac{1}{\omega_n^2+[H_0(\vec{k}_\alpha)]^2}e^{ik_\alpha\cdot(\vec{r}_\alpha-\vec{r}_{\alpha+1})}\right],\end{aligned} \tag{5.24}$$

in which β is the inverse temperature; $\omega_n=(2n+1)\pi/\beta$ is the fermionic Matsubara frequency; $\vec{r}_{1,2,3}=\vec{x},\vec{y},\vec{z}$; and $\vec{r}_4=\vec{r}_1$.

To lowest order in the gradient expansion, we can set $\vec{y}=\vec{z}$ in $\partial_j\mu(\vec{y})\partial_k\Delta_s(\vec{z})$ within Eq. (5.24), then integrating over $\vec{z}$ gives a momentum delta function $\delta^{(3)}(\vec{k}_2-\vec{k}_3)$. Furthermore, if the higher order terms in the gradient expansion are neglected, then $\vec{y}$ can be set as $\vec{x}$ in $\partial_j\mu(\vec{y})\partial_k\Delta_s(\vec{y})$, and the integration over $\vec{y}$ gives $\delta^{(3)}(\vec{k}_1-\vec{k}_2)$. As a result, we obtain $j_i(\vec{x})=\sum_{n=0}^2\left\langle\hat{j}_i^{(n)}(\vec{x})\right\rangle$ as

$$j_i(\vec{x})=e^2D(\Delta_s,\Delta_p)\varepsilon_{ijk}\partial_j\phi(\vec{x})\partial_k\Delta_s(\vec{x}), \tag{5.25}$$

in which $\partial_j\mu=-e\partial_j\phi$ is used, and the coefficient D is

$$\begin{aligned}D(\Delta_s,\Delta_p) &= \frac{4\hbar}{m}(\frac{\Delta_p}{k_f})^3\times \\ &\frac{1}{\beta}\int\frac{d^3k}{(2\pi)^3}\frac{k^2/3}{[\omega_n^2+\xi^2(\vec{k})+(\frac{\Delta_p}{k_f})^2k^2+\Delta_s^2]^3},\end{aligned} \tag{5.26}$$

where the replacement $k_i^2\to k^2/3$ is used which holds under integration. For simplicity, we consider zero temperature such that $\frac{1}{\beta}\sum_n$ can be replaced by $\int\frac{d\omega}{2\pi}$. In the weak pairing limit $\Delta_s,\Delta_p\ll\varepsilon_F$, k can be simply taken as k_f in $(\frac{\Delta_p}{k_f}k)^2$ in the denominator, and $\int dk=\int d\xi/(\hbar v_f)$

where $v_f = \hbar k_f/m$ is the Fermi velocity. Eq. (5.26) can then be evaluated, yielding

$$D(\Delta_s,\Delta_p) = \frac{1}{6\pi^2\hbar}\frac{\Delta_p^3}{(\Delta_p^2+\Delta_s^2)^2}. \tag{5.27}$$

The expression of j_i can be obtained from $j_i = -c\delta S_{\rm ax}/\delta A_i$, where

$$S_{\rm ax} = -\frac{e^2}{c}\int d^4x D(\Delta_s,\Delta_p)\varepsilon_{ijk}A_i\partial_j\phi\partial_k\Delta_s. \tag{5.28}$$

Writing $D(\Delta_s,\Delta_p)$ as a derivative of $\Theta_{\rm ax}$, i.e.,

$$D(\Delta_s,\Delta_p) = -\frac{1}{24\pi^2\hbar}\frac{\partial\Theta_{\rm ax}}{\partial\Delta_s}, \tag{5.29}$$

and performing an integration by part, we arrive at

$$S_{\rm ax} = -\frac{\alpha}{24\pi^2}\int d^4x\Theta_{\rm ax}\varepsilon_{ijk}\partial_i\phi\partial_j A_k, \tag{5.30}$$

where $\alpha = \frac{e^2}{\hbar c}$ is the fine structure constant, and $\int d^4x = \int d^3\vec{r}dt$. Imposing the boundary condition $\Theta_{\rm ax} = 0$ for a pure s-wave superconductor (i.e., $\Delta_s \gg \Delta_p$), $\Theta_{\rm ax}$ is determined to be

$$\begin{aligned}\Theta_{\rm ax}(\Delta_s,\Delta_p) &= 24\pi^2\int_{\Delta_s}^{\infty} dx D(x,\Delta_p)\\ &= \pi - \frac{2\Delta_s\Delta_p}{\Delta_s^2+\Delta_p^2} - 2\arctan(\frac{\Delta_s}{\Delta_p}).\end{aligned} \tag{5.31}$$

Therefore, defining

$$\theta_{\rm ax} = \pi - 2\arctan(\frac{\Delta_s}{\Delta_p}), \tag{5.32}$$

Θ_{ax} can be written as

$$\Theta_{\text{ax}} = \theta_{\text{ax}} - \sin(\theta_{\text{ax}}). \tag{5.33}$$

Here we have two comments regarding the axion angle in Eq. (5.33) and the action in Eq. (5.30). First note that the pairings on the two degenerate Fermi surfaces of different helicities (i.e., $\vec{k}\cdot\vec{\sigma} = \pm 1$) are $|\Delta|e^{\pm i\theta_{\text{ax}}}$ where $|\Delta| = \sqrt{\Delta_s^2 + \Delta_p^2}$. However, the axion angle Θ_{ax} is not just θ_{ax} ,which is the difference between the superconducting phases on the two Fermi surfaces, but acquires an additional $\sin(\theta_{\text{ax}})$ term. Secondly, the conventional axion term in a relativistic system is of the form $\sim \vec{E}\cdot\vec{B}$ where $\vec{E} = -\nabla\phi - \partial_t\vec{A}$. On the other hand, Eq. (5.30) only contains the $\nabla\phi\cdot\vec{B}$ term, which is reasonable since in this section we did not include a time-dependent vector potential. However, we will see in Sec. 5.4 that in fact, the $\partial_t\vec{A}\cdot\vec{B}$ term is missing even in the general situation. Therefore, replacing ϕ by $\phi - \frac{\hbar}{e}\partial_t\Phi$ to keep gauge invariance, Eq. (5.30) is already the full axion action, where Φ is the U(1)-breaking superconducting phase mode. As will be discussed in Sec. 5.4, the difference between the $p+is$ and the relativistic cases is the result of a lack of Lorentz invariance in $p+is$ superconductors.

5.4 Path integral formulation

In this section, we formulate the systematic path integral approach to the axion action in $p+is$ superconductors. We assume the four-fermion interaction to be of the form

$$H_{\text{int}} = -g_s\frac{1}{L^3}\sum_{\vec{k}} P_s^\dagger(\vec{k})P_s(\vec{k}) - g_p\frac{1}{L^3}\sum_{\vec{k}} P_p^\dagger(\vec{k})P_p(\vec{k}), \tag{5.34}$$

in which L is the linear size of the system in space and $g_\lambda > 0$ ($\lambda = s, p$) are coupling constants, and $P_\lambda^\dagger(\vec{k})$'s ($\lambda = s, p$) are defined in Eq. (5.2). After performing a Hubbard-Stratonovich

transformation, the partition function in the imaginary time formalism can be written as

$$\mathcal{Z} = \int D[c^\dagger, c] D[\Delta_s^*, \Delta_s] D[\Delta_p^*, \Delta_p] e^{-\mathcal{S}}, \tag{5.35}$$

in which

$$\mathcal{S} = S_\Delta + S_f, \tag{5.36}$$

where

$$S_\Delta = \sum_{\lambda=s,p} \frac{1}{g_\lambda} \int d\tau d^3 r |\Delta_\lambda|^2, \tag{5.37}$$

and the fermionic part S_f is

$$S_f = \frac{1}{2} \int d\tau d^3 r \Psi^\dagger(\tau, \vec{r}) (\partial_\tau + H_f) \Psi(\tau, \vec{r}), \tag{5.38}$$

in which $\Psi^\dagger(\tau, \vec{r})$ is a set of Grassmann numbers defined through the Fourier transform of $\Psi^\dagger(\vec{k})$ in Eq. (5.5), and H_f is given by

$$\begin{aligned}
H_f^{11} &= \frac{1}{2m}(-i\hbar\nabla + \frac{e}{c}\vec{A})^2 - \varepsilon_F - ie\phi + g\mu_B \vec{B}\cdot\vec{\sigma}, \\
H_f^{12} &= [\frac{1}{2k_f} e^{-i\Phi}\{\Delta_p, -i\nabla\} e^{-i\Phi} \cdot \vec{\sigma} + i\Delta_s e^{-i(2\Phi+\Phi_l)}] i\sigma_2, \\
H_f^{21} &= H_{f(1,2)}^\dagger, \\
H_f^{22} &= -[\frac{1}{2m}(-i\hbar\nabla - \frac{e}{c}\vec{A})^2 - \varepsilon_F - ie\phi + g\mu_B \vec{B}\cdot\vec{\sigma}^T],
\end{aligned} \tag{5.39}$$

in which H_f^{ij} $(i,j=1,2)$ is the (i,j)-block of H_f; $i\phi$ is the electric potential in imaginary time; $\{A,B\} = AB + BA$ denotes the anticommutator of the operators A and B; and Φ and Φ_l are the

superconducting phase mode and the Leggett mode, respectively.

The phase mode Φ can be absorbed into electromagnetic potentials by performing a gauge transformation [] through the following replacements:

$$\begin{aligned} -ie\phi &\rightarrow \phi' = -ie\phi + \partial_\tau \Phi, \\ \frac{e}{c}\vec{A} &\rightarrow \vec{A}' = \frac{e}{c}\vec{A} + \hbar\nabla\Phi. \end{aligned} \tag{5.40}$$

Assuming a background Δ_λ ($\lambda = s, p$) and including small fluctuations of the different modes, H_f becomes

$$H_f = H_{f0} + \Delta H_f,$$

in which H_{f0} is simply Eq. 5.6, and

$$\begin{aligned} \Delta H_f &= \Delta H_A^{(1)} + \Delta H_A^{(2)} + \Delta H_\phi + \Delta H_Z \\ &\quad + \Delta H_p + \Delta H_s + \Delta H_l, \end{aligned} \tag{5.41}$$

where

$$\begin{aligned} \Delta H_A^{(1)} &= \frac{\hbar}{2m}\{\vec{A}'(\tau,\vec{r}), -i\nabla\}\sigma_0\tau_0, \\ \Delta H_A^{(2)} &= \frac{1}{2m}[\vec{A}'(\tau,\vec{r})]^2\gamma^0, \\ \Delta H_\phi &= \phi'(\tau,\vec{r})\gamma^0, \\ \Delta H_Z &= -\frac{i}{4}g\mu_B\varepsilon_{ijk}B_i\gamma^j\gamma^k, \\ \Delta H_p &= \frac{1}{2k_f}\{\delta\Delta_p(\tau,\vec{r}), -i\nabla\}\cdot\vec{\gamma}, \\ \Delta H_s &= \delta\Delta_s(\tau,\vec{r})\gamma^4, \\ \Delta H_l &= \Delta_s\delta\Phi_l(\tau,\vec{r})\sigma_2\tau_2. \end{aligned} \tag{5.42}$$

We note that in momentum space, $\Delta H_A^{(1)}(\vec{q}) = \frac{\hbar}{2m}(2\vec{k}+\vec{q})\cdot\vec{A}'(\vec{q})$ and $\Delta H_p(\vec{q}) = \frac{1}{k_f}(\vec{k}+\vec{q}/2)\cdot \delta\Delta_p(\vec{q})$.

Since the fermionic quasiparticles are fully gapped, the action for the collective bosonic degrees of freedom can be obtained by integrating over the fermions, resulting in $\frac{1}{2}\mathrm{Trln}(-\partial_\tau - H_f)$. In what follows, we will only consider the axion terms. They arise in the third order terms in the Trln-expansion, i.e.,

$$S_f^{(3)} = -\frac{1}{6}\mathrm{Tr}[(\mathcal{G}_0\Delta H_f)^3], \tag{5.43}$$

in which $\mathcal{G}_0 = (\partial_\tau + H_0)^{-1}$. Here we note that as discussed in Sec. 5.5 and Sec. 5.6, in addition to the axion terms, there are other nonvanishing terms in $S_f^{(3)}$ which involve two spacetime derivatives, as a consequence of a lack of Lorentz symmetry. We do not explicitly calculate these additional terms since the calculations are very cumbersome. A list of such terms based on a symmetry analysis is included in Appendix 5.A.

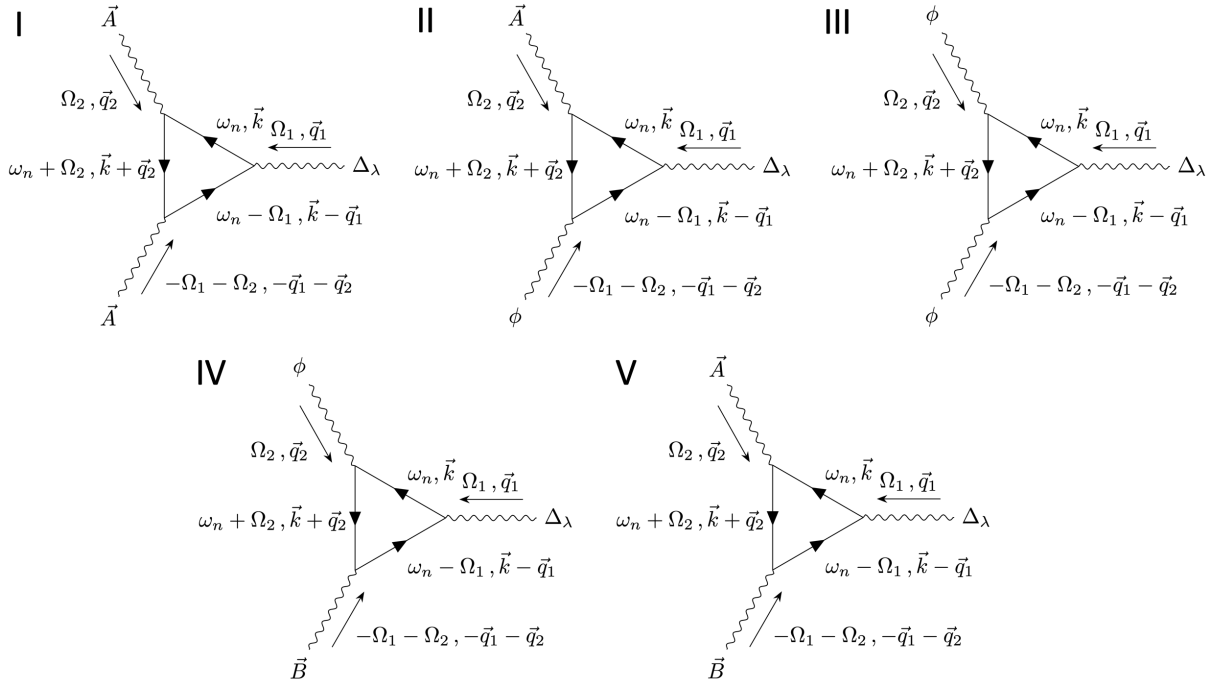

Figure 5.1: Diagrams potentially contributing to axion electrodynamics where $\lambda = s, p$ in Δ_λ.

5.5 Orbital contribution to axion electrodynamics

In this section, we calculate the orbital contribution to the axion action based on the path integral approach. There are three diagrams which contain two A^μ's ($\mu = 0,1,2,3$ where A^0 is ϕ) and one $\delta\Delta_\lambda$ ($\lambda = s, p$), as shown in Fig. 5.1 (I, II, III). Diagram III – though not zero – does not contribute to the axion action, hence we neglect. We will only calculate the terms involving two spacetime derivatives in diagrams I, II in Fig. 5.1.

5.5.1 Diagram I

This diagram potentially can contribute to $\int d^4x \partial_t \vec{A}' \cdot \vec{B}$ in the axion action. However, we demonstrate that in fact, this contribution vanishes.

$\lambda = s$

One term contributing to the $\lambda = s$ case is $-\frac{1}{6}\mathrm{Tr}[\mathcal{G}_0 \Delta H_A^{(1)} \mathcal{G}_0 \Delta H_A^{(1)} \mathcal{G}_0 \Delta H_s]$. Including the combinatoric factor of 3, we obtain

$$
\begin{aligned}
D_s^{\mathrm{I}} = \frac{1}{2}\frac{1}{\beta}\sum_{\omega_n}\int \frac{d^3\vec{k}}{(2\pi)^3}\mathrm{tr}\big[\\
&\mathcal{G}_0(\omega_n,\vec{k})\frac{\hbar}{2m}(2\vec{k}+\vec{q}_2)\cdot\vec{A}'(\Omega_2,\vec{q}_2)\,\mathcal{G}_0(\omega_n+\Omega_2,\vec{k}+\vec{q}_2) \\
&\times \frac{\hbar}{2m}(2\vec{k}-\vec{q}_1)\cdot\vec{A}'(-\Omega_1-\Omega_2,-\vec{q}_1-\vec{q}_2) \\
&\times \mathcal{G}_0(\omega_n-\Omega_1,\vec{k}-\vec{q}_1)\delta\Delta_s(\Omega_1,\vec{q}_1)\gamma^4\big],
\end{aligned}
\tag{5.44}
$$

in which the minus sign coming from the fermion loop cancels with the sign in Eq. (5.43), and

$$
\mathcal{G}_0(\omega_n,\vec{k}) = \frac{a_\chi(\omega_n,\vec{k})\gamma^\chi}{a_\chi(\omega_n,\vec{k})a_\chi(\omega_n,\vec{k})},
\tag{5.45}
$$

where the summation of χ is over $\chi = 0,1,2,3,4,5$; $\gamma^5 = \sigma_0\tau_0$; and

$$a_0 = \xi_{\vec{k}},\ a_i = \frac{\Delta_p}{k_f}k_i\ (i = 1,2,3),\ a_4 = \Delta_s,\ a_5 = i\omega_n. \tag{5.46}$$

Plugging Eq. (5.45) into Eq. (5.44), the trace of the numerators of $\mathcal{G}_0$ gives

$$\begin{aligned}&\mathrm{tr}\big[a_{\chi_1}(\omega_n,\vec{k})\gamma^{\chi_1}a_{\chi_2}(\omega_n+\Omega_2,\vec{k}+\vec{q}_2)\gamma^{\chi_2}\\&a_{\chi_3}(\omega_n-\Omega_1,\vec{k}-\vec{q}_1)\gamma^{\chi_3}\gamma^4\big]\end{aligned} \tag{5.47}$$

We note that the $O(\Omega_j)$ $(j = 1,2)$ term in Eq. (5.47) is $8\omega_n\Delta_s(\Omega_1 - \Omega_2)$.

To generate $\int d^4x\partial_t\vec{A}\cdot\nabla\times\vec{A}$, we must consider terms in Eq. (5.44) which involve one Ω_j and one $\vec{q}_j$ $(j = 1,2)$. It is straightforward to see that the $O(\Omega_j)$ term in $1/\sum_{i=0}^{5}[a_i(\omega_n+\Omega,\vec{k}+\vec{q})]^2$ ($\Omega = -\Omega_1,\Omega_2$ and $\vec{q} = -\vec{q}_1,\vec{q}_2$) is proportional to $\omega_n\Omega$, similar as the $O(\Omega_j)$ term in the trace in Eq. (5.47). Since the Matsubara summation of terms involving odd powers of ω_n vanishes, we conclude that there is no contribution to $\int d^4x\partial_t\vec{A}\cdot\nabla\times\vec{A}$ from Diagram I for $\lambda = s$.

$\lambda = p$

The analysis for $\lambda = p$ in Diagram I is exactly similarly and the contribution again vanishes.

5.5.2 Diagram II

This diagram potentially can contribute to $\int d^4x\nabla\phi'\cdot\vec{B}$ in the axion action. We show that it gives exactly the axion action derived in Sec. 5.3.

$\lambda = s$

One term contributing to the $\lambda = s$ case is $-\frac{1}{6}\mathrm{Tr}[\mathcal{G}_0 \Delta H_A^{(1)} \mathcal{G}_0 \Delta H_\phi \mathcal{G}_0 \Delta H_s]$. Including the combinatoric factor of 6 and using Eq. (5.45), we obtain

$$
\begin{aligned}
D_s^{\mathrm{II}} &= \frac{1}{\beta}\sum_{\omega_n}\int \frac{d^3\vec{k}}{(2\pi)^3}\frac{\hbar}{2m}(2\vec{k}+\vec{q}_2)\cdot\vec{A}'(\Omega_2,\vec{q}_2) \\
&\times \phi'(-\Omega_1-\Omega_2,-\vec{q}_1-\vec{q}_2)\delta\Delta_s(\Omega_1,\vec{q}_1) \\
&\times \mathrm{tr}\big[a_{\chi_1}(\omega_n,\vec{k})\gamma^{\chi_1}a_{\chi_2}(\omega_n+\Omega_2,\vec{k}+\vec{q}_2)\gamma^{\chi_2}\gamma^0 \\
&\qquad \cdot a_{\chi_3}(\omega_n-\Omega_1,\vec{k}-\vec{q}_1)\gamma^{\chi_3}\gamma^4\big], \\
&\times \Pi_{\nu=1}^{3}\frac{1}{a_\chi(\omega_n+\Omega'_\nu,\vec{k}+\vec{q}'_\nu)a_\chi(\omega_n+\Omega'_\nu,\vec{k}+\vec{q}'_\nu)},
\end{aligned}
\tag{5.48}
$$

in which $\Omega'_1=0$, $\Omega'_2=\Omega_2$, $\Omega'_3=-\Omega_1$, and $\vec{q}'_1=0$, $\vec{q}'_2=\vec{q}_2$, $\vec{q}'_3=-\vec{q}_1$. Recall that we want a term $\sim \varepsilon_{ijk}\partial_i\phi\partial_j A_k$ in the action. Such term can be generated from the trace of a multiplication of the product of five γ-matrices as shown in Eq. (5.22). Then the ε_{ijk} term within the trace in Eq. (5.48) can be evaluated as

$$
\begin{aligned}
\mathrm{tr}[...] &= -4(\frac{\Delta_p}{k_f})^3\varepsilon_{ijk}k_i(k_j+q_{2j})(k_k-q_{1k}) \\
&= 4(\frac{\Delta_p}{k_f})^3\varepsilon_{ijk}k_i q_{2j}q_{1k}.
\end{aligned}
\tag{5.49}
$$

Since Eq. (5.49) already contains a product of two wavevector q's, we can set $\vec{q}_j,\Omega_j$ to be zero in the remaining parts of Eq. (5.48). This gives

$$
\begin{aligned}
&D_s^{\mathrm{II}} = D(\Delta_s,\Delta_p)\varepsilon_{ijk}q_{2j}q_{1k}\times \\
&A'_i(\Omega_2,\vec{q}_2)\delta\Delta_s(\omega_1,\vec{q}_1)\phi'(-\Omega_1-\Omega_2,\vec{q}_1-\vec{q}_2),
\end{aligned}
\tag{5.50}
$$

in which $D(\Delta_s, \Delta_p)$ is given exactly by Eq. (5.26). Integration by part and transforming to the real space, the corresponding term in the action is

$$\int d^4x D(\Delta_s, \Delta_p) \vec{A}' \cdot (\nabla\phi' \times \nabla\delta\Delta_s). \tag{5.51}$$

$\lambda = p$

When $\lambda = p$, D_p^{II} can be obtained from D_s^{II} by replacing $\delta\Delta_s$ in Eq. (5.48) with $\delta\Delta_p$, and changing the trace to

$$\begin{aligned} &\mathrm{tr}\big[a_{\chi_1}(\omega_n, \vec{k})\gamma^{\chi_1} a_{\chi_2}(\omega_n + \Omega_2, \vec{k} + \vec{q}_2)\gamma^{\chi_2}\gamma^0 \\ &\cdot a_{\chi_3}(\omega_n - \Omega_1, \vec{k} - \vec{q}_1)\gamma^{\chi_3} \frac{1}{k_f}(\vec{k} - \frac{\vec{q}_1}{2}) \cdot \vec{\gamma}\big]. \end{aligned} \tag{5.52}$$

The ε_{ijk} term in Eq. (5.52) can be straightforwardly evaluated as

$$-4\frac{\Delta_s(\Delta_p)^2}{k_f^3}\varepsilon_{ijk} q_{2i} q_{1j} k_k. \tag{5.53}$$

As a result, the corresponding term in the axion action in real space is

$$-D'(\Delta_s, \Delta_p)\vec{A}' \cdot (\nabla\phi' \times \nabla\delta\Delta_p), \tag{5.54}$$

in which

$$D'(\Delta_s, \Delta_p) = \frac{\Delta_s}{\Delta_p} D(\Delta_s, \Delta_p). \tag{5.55}$$

5.5.3 Diagram III

This diagram does not contribute to the axion action as explained at the beginning of this section, though it does contribute to non-axion terms as discussed in Appendix 5.A.

5.5.4 Orbital contribution to the axion action

Combining Eq. (5.51,5.54) together and using $\nabla\delta\Delta_\lambda = \nabla\Delta_\lambda$, we obtain

$$S^o_{\rm ax} = \int d^4x\vec{A}' \cdot [\nabla\phi' \times (D\nabla\Delta_s - D'\nabla\Delta_p)], \tag{5.56}$$

in which D (D') is $D(\Delta_s,\Delta_p)$ ($D(\Delta_s,\Delta_p)$) for short. Plugging in the expression of D given in Eq. (5.27), we have

$$D\nabla\Delta_s - D'\nabla\Delta_p = \frac{1}{6\pi^2\hbar}\frac{1}{[1+(\frac{\Delta_s}{\Delta_p})^2]^2}\nabla(\frac{\Delta_s}{\Delta_p}). \tag{5.57}$$

Using the integral

$$\int_{\frac{\Delta_s}{\Delta_p}}^{\infty}\frac{dx}{(1+x^2)^2} = \frac{1}{4}[\pi - 2\arctan(\frac{\Delta_s}{\Delta_p}) - 2\frac{\Delta_s/\Delta_p}{1+(\Delta_s/\Delta_p)^2}], \tag{5.58}$$

$S^o_{\rm ax}$ becomes

$$S^o_{\rm ax} = -\frac{\alpha}{24\pi^2}\int d^4x\vec{A}' \cdot [\nabla\phi' \times \nabla\Theta^o_{\rm ax}], \tag{5.59}$$

where $\Theta^o_{\rm ax}$ coincides exactly with the expression in Eq. (5.33). Integrating by parts, employing Eq. (5.40), and transforming to the real time (i.e., $i\phi \to \phi$), we obtain

$$S^o_{\rm ax} = -\frac{\alpha}{24\pi^2}\int d^4x\Theta^o_{\rm ax}\nabla(\phi - \frac{\hbar}{e}\partial_t\Phi)\cdot\vec{B}, \tag{5.60}$$

where $\nabla\times\nabla\Phi = 0$ is used. This is exactly what we have obtained in Eq. (5.30).

The differences between Eq. (5.60) and the axion action in the relativistic case have been discussed by the end of Sec. 5.3. The essential reason is a lack of Lorentz symmetry in the $p+is$ case. Here we note that on a technical level, the band dispersion in the normal metal

phase of $p+is$ superconductor does not contain negative energy states. Therefore, unlike the relativistic case, there is no inter-band transition (from negative to positive energy bands) in the $p+is$ superconducting case, which leads to the different behaviors between the two situations.

5.6 Zeeman contribution to axion electrodynamics

In this section, we calculate the Zeeman contribution to the axion action based on the path integral approach.

5.6.1 Diagram IV

This diagram potentially can contribute to $\int d^4x \nabla\phi' \cdot \vec{B}$ in the axion action. We will derive its explicit expression.

$\lambda = s$

One term contributing to the $\lambda = s$ case is $-\frac{1}{6}\mathrm{Tr}[\mathcal{G}_0 \Delta H_Z \mathcal{G}_0 \Delta H_\phi \mathcal{G}_0 \Delta H_s]$. Including the combinatoric factor of 6, we obtain

$$
\begin{aligned}
D_s^{\mathrm{IV}} = & \frac{1}{\beta}\sum_{\omega_n}\int \frac{d^3\vec{k}}{(2\pi)^3}\mathrm{tr}\big[\\
& \mathcal{G}_0(\omega_n,\vec{k})\phi'(\Omega_2,\vec{q}_2)\gamma^0\mathcal{G}_0(\omega_n+\Omega_2,\vec{k}+\vec{q}_2) \\
& \times(-)\frac{1}{4}ig\mu_B\varepsilon_{ijk}\gamma^j\gamma^k B_i(-\Omega_1-\Omega_2,-\vec{q}_1-\vec{q}_2) \\
& \times \mathcal{G}_0(\omega_n-\Omega_1,\vec{k}-\vec{q}_1)\delta\Delta_s(\Omega_1,\vec{q}_1)\gamma^4\big].
\end{aligned}
\tag{5.61}
$$

Only considering the axion term $\int d^4x \nabla\phi' \cdot \vec{B}$, we can set $\Omega_1 = \Omega_2 = 0$, and it is enough to expand D_s^{IV} up to linear order in $\vec{q}_\alpha$ ($\alpha = 1,2$). Calculations show that ($\alpha,\beta = 1,2$; $i,j,k = x,y,z$;

$k_i \neq k_j \neq k_k$)

$$D_s^{\rm IV} = E_{1si} i q_{1i} B_i + E_{2si} i q_{2i} B_i + O(q_{\alpha j} q_{\beta k}), \tag{5.62}$$

in which

$$E_{\alpha si} = -2 g \mu_B \frac{\Delta_p}{k_f} \frac{1}{\beta} \sum_{\omega_n} \int \frac{d^3\vec{k}}{(2\pi)^3} M_{\alpha si}, \tag{5.63}$$

where

$$\begin{aligned} M_{1si} &= \frac{-\omega_n^2 + \xi_{\vec{k}}^2 + (k_i^2 - k_j^2 - k_k^2)\frac{\Delta_p^2}{k_f^2} - \Delta_s^2}{[\omega_n^2 + \xi_{\vec{k}}^2 + (\frac{\Delta_p}{k_f})^2 k^2 + \Delta_s^2]^3}, \\ M_{2si} &= \frac{\omega_n^2 - \frac{\hbar^2}{2m}(k_f^2 - k^2 + 4k_i^2)\xi_{\vec{k}} + \frac{\Delta_p^2}{k_f^2}(k^2 - 2k_i^2) - \Delta_s^2}{[\omega_n^2 + \xi_{\vec{k}}^2 + (\frac{\Delta_p}{k_f})^2 k^2 + \Delta_s^2]^3}. \end{aligned} \tag{5.64}$$

We note that: the $q_{1i}B_j$ ($i \neq j$) terms vanish in $D_s^{\rm IV}$ after the integration over the solid angle of $\vec{k}$; and k_i^2 can be replaced by $k^2/3$ in the integration. Therefore,

$$M_{\alpha si} \equiv M_{\alpha s},\ E_{\alpha si} \equiv E_{\alpha s}, \tag{5.65}$$

where $i = x, y, z$.

We will only keep the leading order terms in an expansion over $\Delta_\lambda/\varepsilon_f$ ($\lambda = s, p$). Then in E_{1s}, all k^2 can be replaced by k_f^2 in the integrand M_{1s}, and $\int d^3\vec{k}/(2\pi)^3$ can be set as $N_f \int d\xi$, where $N_f = \frac{m k_f}{2\pi^2\hbar^2}$. On the other hand, M_{2si} contains a term $-\frac{\hbar^2}{2m}(k_f^2 + \frac{k^2}{3})\xi_{\vec{k}}$, which is one order less than the other terms in the numerator. Therefore, in this case, $\int d^3\vec{k}/(2\pi)^3$ should be set as

$N_f \int (1+\frac{\xi}{2\varepsilon_f})d\xi$, and

$$M_{2s} \to -\frac{\frac{4}{3}\xi_{\vec{k}}\varepsilon_f}{[\omega_n^2+\xi_{\vec{k}}^2+(\frac{\Delta_p}{k_f})^2k^2+\Delta_s^2]^3}+ \\ \frac{\omega_n^2-\frac{1}{3}\xi_{\vec{k}}^2+\frac{1}{3}\Delta_p^2-\Delta_s^2}{[\omega_n^2+\xi_{\vec{k}}^2+(\frac{\Delta_p}{k_f})^2k^2+\Delta_s^2]^3}+\frac{4\Delta_p^2\xi_{\vec{k}}^2}{[\omega_n^2+\xi_{\vec{k}}^2+(\frac{\Delta_p}{k_f})^2k^2+\Delta_s^2]^4}, \tag{5.66}$$

where the first term can combine with $N_f \int \frac{\xi}{2\varepsilon_f} d\xi$ within $\int d^3\vec{k}/(2\pi)^3$ giving a nonzero contribution, and the third term in Eq. (5.66) comes from expanding the denominator using $\Delta_p^2 k^2/k_f^2 = \Delta_p^2(1+\xi_{\vec{k}}/\varepsilon_f)$. Again at zero temperature, $\frac{1}{\beta}\sum\omega_n = \int \frac{d\omega}{2\pi}$. Performing the integrations $\int d\omega \int d\xi$, we obtain

$$\begin{aligned} E_{1s}(\Delta_s,\Delta_p) &= \frac{g\mu_B m}{12\pi^2\hbar^2}\frac{\Delta_p(3\Delta_s^2+\Delta_p^2)}{(\Delta_p^2+\Delta_s^2)^2}, \\ E_{2s}(\Delta_s,\Delta_p) &= \frac{g\mu_B m}{4\pi^2\hbar^2}\frac{\Delta_p(\Delta_s^2-\Delta_p^2)}{(\Delta_p^2+\Delta_s^2)^2}. \end{aligned} \tag{5.67}$$

Transforming back to the real space, the action becomes

$$S_{\rm ax}^Z = \int d^4x \left[E_{1s}\nabla\delta\Delta_s\cdot\vec{B}\phi' + E_{2s}\delta\Delta_s\vec{B}\cdot\nabla\phi'\right]. \tag{5.68}$$

Integrating by parts, dropping total derivative terms, and using $\nabla\cdot\vec{B}=0$, we obtain the axion action

$$\int d^4x (E_{1s}-E_{2s})\phi'\nabla\delta\Delta_s\cdot\vec{B}. \tag{5.69}$$

$\lambda = p$

Similar as the $\lambda = s$ case, the expression with a spatially varying $\delta\Delta_p$ is

$$
\begin{aligned}
D_p^{\mathrm{IV}} = & \frac{1}{\beta}\sum_{\omega_n}\int\frac{d^3\vec{k}}{(2\pi)^3}\mathrm{tr}\big[\\
& \mathcal{G}_0(\omega_n,\vec{k})\phi'(\Omega_2,\vec{q}_2)\gamma^0\mathcal{G}_0(\omega_n+\Omega_2,\vec{k}+\vec{q}_2) \\
& \times(-)\frac{1}{4}ig\mu_B\varepsilon_{ijk}\gamma^i\gamma^k B_i(-\Omega_1-\Omega_2,-\vec{q}_1-\vec{q}_2) \\
& \times\mathcal{G}_0(\omega_n-\Omega_1,\vec{k}-\vec{q}_1)\frac{1}{k_f}\delta\Delta_p(\Omega_1,\vec{q}_1)(\vec{k}-\frac{\vec{q}_1}{2})\cdot\vec{\gamma}\big].
\end{aligned}
\tag{5.70}
$$

Again setting $\Omega_1 = \Omega_2 = 0$, and keeping the linear in $\vec{q}_\alpha$ ($\alpha = 1,2$), we obtain

$$
D_p^{\mathrm{IV}} = E_{1p}iq_{1i}B_i + E_{2p}iq_{2i}B_i + O(q_{\alpha j}q_{\beta k}),
\tag{5.71}
$$

in which

$$
E_{\alpha p} = -g\mu_B\frac{\Delta_s}{k_f}\frac{1}{\beta}\sum_{\omega_n}\int\frac{d^3\vec{k}}{(2\pi)^3}M_{\alpha p},
\tag{5.72}
$$

where ($k_i \neq k_j \neq k_k$)

$$
\begin{aligned}
M_{1p} &= \frac{\omega_n^2+\xi_{\vec{k}}^2+(\frac{\Delta_p}{k_f})^2(k^2-4k_i^2)+\Delta_s^2}{[\omega_n^2+\xi_{\vec{k}}^2+(\frac{\Delta_p}{k_f})^2k^2+\Delta_s^2]^3}, \\
M_{2p} &= \frac{4[-(\frac{\Delta_p}{k_f})^2(k_j^2+k_k^2)+\frac{\hbar^2}{m}k_i^2\xi_{\vec{k}}]}{[\omega_n^2+\xi_{\vec{k}}^2+(\frac{\Delta_p}{k_f})^2k^2+\Delta_s^2]^3}.
\end{aligned}
\tag{5.73}
$$

We note that again, the values of Eq. (5.73) do not depend on $i = x,y,z$. Calculations show that (up to leading order in $\Delta_\lambda/\varepsilon_f$, where $\lambda = s,p$)

$$
E_{\alpha p} = -\frac{\Delta_s}{\Delta_p}E_{\alpha s}.
\tag{5.74}
$$

Correspondingly, the contribution to the axion action is

$$\int d^4x(E_{1p}-E_{2p})\phi'\nabla\delta\Delta_p\cdot\vec{B}. \tag{5.75}$$

5.6.2 Diagram V

This diagram potentially can contribute to $\int d^4x\partial_t\vec{A}'\cdot\vec{B}$ in the axion action. However, in a way similar with the discussions in Sec. 5.5.1, it can be seen that the axion contribution from this diagram vanishes, since the integrand is odd with respect to the fermionic Matsubara frequency.

5.6.3 Zeeman contribution to the axion action

Combining Eqs. (5.69,5.75) and using Eq. (5.74), we obtain

$$S^Z_{\rm ax}=\int d^4x\phi' E^Z(\Delta_s,\Delta_p)\nabla(\frac{\Delta_s}{\Delta_p})\cdot\vec{B}, \tag{5.76}$$

in which

$$\begin{aligned} E^Z &= \Delta_p(E_{1s}-E_{2s}) \\ &= \frac{g\mu_B m}{3\pi^2\hbar^2}\frac{1}{[1+(\Delta_s/\Delta_p)^2]^2}. \end{aligned} \tag{5.77}$$

Using

$$\int_0^{\frac{\Delta_s}{\Delta_p}}\frac{dx}{(1+x^2)^2}=\frac{1}{2}\big[\arctan(\Delta_s/\Delta_p)+\frac{\Delta_s/\Delta_p}{1+(\Delta_s/\Delta_p)^2}\big], \tag{5.78}$$

and plugging in $\mu_B=\frac{e\hbar}{2mc}$, $S^Z_{\rm ax}$ becomes

$$S^Z_{\rm ax}=\frac{ge}{24\pi^2\hbar c}\int d^4x\phi'\nabla\Theta^Z_{\rm ax}\cdot\vec{B}, \tag{5.79}$$

in which α is again the fine structure constant, and

$$\Theta_{\rm ax}^{Z} = 2\arctan(\frac{\Delta_s}{\Delta_p}) + \frac{2\Delta_s\Delta_p}{\Delta_s^2+\Delta_p^2}. \tag{5.80}$$

Further performing an integration by part and transforming to real time, we obtain

$$S_{\rm ax}^{Z} = \frac{g\alpha}{24\pi^2}\int d^4x\Theta_{\rm ax}^{Z}\nabla(\phi - \frac{\hbar}{e}\partial_t\Phi)\cdot\vec{B}, \tag{5.81}$$

in which $g = 2$ in vacuum, but can be somewhat arbitrary in solid state materials. The action $S_{\rm ax}^{Z}$ in Eq. (5.81) can also contribute to transverse supercurrent, similar to its orbital counterpart as discussed in Sec. 5.3. However, we note that unlike the orbital case, the current arising from Eq. (5.81) are bound currents, which are not related to wavepacket transport of electrons.

Here we note that $\Theta_{\rm ax}^{Z} = \pi - \Theta_{\rm ax}^{o}$, where the expression of $\Theta_{\rm ax}^{o}$ is given in Eq. (5.33). This difference comes from the integral $\int_0^{\Delta_s/\Delta_p} dx$ in Eq. (5.78), unlike the one in Eq. (5.58) which is $\int_{\Delta_s/\Delta_p}^{\infty} dx$. The choice of the lower and upper bounds of the integration in Eq. (5.78) is consistent with Ref. [147], where the free energy describing the magnetoelectric effect in the spin channel is calculated in the vicinity of T_c. It is shown in Ref. [147] that for a pure p-wave superconductor, the spin magnetoelectric effect vanishes. Therefore, in the current situation, $\Theta_{\rm ax}^{Z}$ should be zero for a pure p-wave superconductor in the absence of Δ_s.

5.7 Conclusions

In conclusion, we have studied the coupling between the axion angle and the electromagnetic field in $p+is$ superconductors. Including both the orbital and Zeeman contributions, the axion action is derived as

$$S_{\rm ax} = -\frac{\alpha}{24\pi^2}\int d^4x\Theta_{\rm ax}\nabla(\phi - \frac{\hbar}{e}\partial_t\Phi)\cdot\vec{B}, \tag{5.82}$$

in which α is the fine structure constant, and the axion angle is

$$\begin{aligned}\Theta_{\rm ax} &= \Theta^{o}_{\rm ax} - \Theta^{Z}_{\rm ax} \\ &= -g\pi + (1+g)(\theta_{\rm ax} - \sin\theta_{\rm ax}),\end{aligned} \tag{5.83}$$

where g is the Landé factor and $\theta_{\rm ax} = \pi - 2\arctan(\Delta_s/\Delta_p)$. The axion action in Eq. (5.82) has two differences compared with the relativistic case. The induced electric field does not appear, therefore $S_{\rm ax}$ does not have Lorentz symmetry. In addition, the axion angle $\Theta_{\rm ax}$ also contains a sinusoidal term $\sin(\theta_{\rm ax})$, not just $\theta_{\rm ax}$. Our work reveals the crucial difference for axion electrodynamics between the $p+is$ superconductors and the superconducting Dirac/Weyl systems.

Acknowledgments CX is supported by The Office of Naval Research under grant N00014-18-1-2722. WY is supported by the postdoctoral fellowship at Stewart Blusson Quantum Matter Institute, University of British Columbia.

5.A Symmetry allowed non-axion terms

In this appendix we examine all the symmetry allowed terms which contain one Δ_λ ($\lambda = s, p$), two A^μ's ($\mu = t, x, y, z$), and two spacetime derivatives. Up to an overall factor $F(\Delta_s^2, \Delta_s/\Delta_p)\Delta_\lambda$ (where F is a function which can be determined by calculating the corresponding diagram), the terms invariant under 3D rotations and $\mathcal{PT}$-operation are

$$\begin{aligned}&\partial_t \vec{A}' \cdot \partial_t \vec{A}' \; \delta\Delta_\lambda \\ &\partial_t^2 \vec{A}' \cdot \vec{A}' \; \delta\Delta_\lambda \\ &\partial_t \phi' \partial_t \phi' \; \delta\Delta_\lambda \\ &\partial_t^2 \phi' \; \phi' \; \delta\Delta_\lambda\end{aligned} \tag{5.84}$$

$$(\nabla\cdot\vec{A}')(\nabla\cdot\vec{A}')\ \delta\Delta_\lambda$$
$$\nabla^2\vec{A}'\cdot\vec{A}'\ \delta\Delta_\lambda$$
$$\nabla\phi'\cdot\nabla\phi'\ \delta\Delta_\lambda$$
$$\nabla^2\phi'\ \phi'\ \delta\Delta_\lambda \tag{5.85}$$

$$\partial_t\vec{A}'\cdot(\nabla\times\vec{A}')\ \delta\Delta_\lambda$$
$$\vec{A}'\cdot(\nabla\times\partial_t\vec{A}')\ \delta\Delta_\lambda \tag{5.86}$$

$$(\nabla\cdot\vec{A}')\partial_t\phi'\ \delta\Delta_\lambda \tag{5.87}$$

$$(\nabla\times\vec{A}')\cdot(\nabla\phi')\ \delta\Delta_\lambda\,, \tag{5.88}$$

in which $\lambda = s, p$. The terms in Eq. (5.86) vanish as discussed in Sec. 5.5.1, and Eq. (5.88) is the axion term which has been calculated and discussed in the main text.

Here we make a comment on the order of the coefficients of the non-axion terms. In superconductors, the leading term in the action for the phase mode is

$$\int d^4x\big[N_f(\hbar\partial_t\Phi - e\phi)^2 + \frac{n_s}{2m}(\hbar\nabla\Phi + \frac{e\vec{A}}{c})^2\big], \tag{5.89}$$

in which n_s is the superfluid density. Notice that in the long wavelength limit, additional spacetime gradient terms are suppressed by factor of $(q\xi_c)^n \sim (\hbar v_f q/\Delta)^n$ [192], where ξ_c is the coherence length, and q can be either $|\vec{q}|$ or $|\Omega|/v_f$. For simplicity, consider the term $\partial_t\vec{A}\cdot\nabla\times\vec{A}$ (although this term vanishes as discussed in Eq. (5.86), it works as an illustration for the other non-axion terms, regarding the order of the coefficients). The coefficient C of this term should be on order of

$\sim \frac{1}{\Delta}(\frac{v_f}{\Delta})\frac{n_s}{2m}$. Using $n_s \sim k_f^3$, it is straightforward to obtain $C \sim (\varepsilon_f/\Delta)^2$. Other other hand, recall that the coefficients of the axion terms are of $O[(\Delta/\varepsilon_f)^0]$. Therefore, generically, the non-axion terms can be much larger, i.e., enhanced by a factor of $(\varepsilon_f/\Delta)^2$ compared with the axion terms. However, we note that none of the non-axion terms can contribute to the effects like transverse supercurrent as discussed in Sec. 5.3, and in fact, they do not exhibit magnetoelectric effects.

This chapter is a reprint of the following preprint being prepared for submission for publication: 'C. Xu and W. Yang, **Axion electrodynamics in p+is superconductors**. *arXiv: 2009.12998*'. The dissertation author was the primary investigator and author of this paper.

Bibliography

[1] Yu. E. Lozovik and V. I. Yudson. A new mechanism for superconductivity: pairing between spatially separated electrons and holes. *Journal of Experimental and Theoretical Physics*, 44:389–397, 1976.

[2] M. Hagn, A. Zrenner, G. Böhm, and G. Weimann. Electric-field-induced exciton transport in coupled quantum well structures. *Applied Physics Letters*, 67(2):232–234, 1995.

[3] Andreas Gärtner, A. W. Holleitner, J. P. Kotthaus, and D. Schuh. Drift mobility of long-living excitons in coupled GaAs quantum wells. *Applied Physics Letters*, 89(5):052108, 2006.

[4] A. T. Hammack, L. V. Butov, Joe Wilkes, Leonidas Mouchliadis, Egor A. Muljarov, A. L. Ivanov, and A. C. Gossard. Kinetics of the inner ring in the exciton emission pattern in coupled GaAs quantum wells. *Physical Review B*, 80(15):155331, 2009.

[5] J. R. Leonard, Y. Y. Kuznetsova, Sen Yang, L. V. Butov, T. Ostatnicky, A. Kavokin, and A. C. Gossard. Spin transport of excitons. *Nano Letters*, 9(12):4204–4208, 2009.

[6] S Lazić, PV Santos, and R Hey. Exciton transport by moving strain dots in gaas quantum wells. *Physica E: Low-dimensional Systems and Nanostructures*, 42(10):2640–2643, 2010.

[7] Mathieu Alloing, Aristide Lemaître, Elisabeth Galopin, and François Dubin. Nonlinear dynamics and inner-ring photoluminescence pattern of indirect excitons. *Physical Review B*, 85(24):245106, 2012.

[8] S Lazić, A Violante, K Cohen, R Hey, Ronen Rapaport, and PV Santos. Scalable interconnections for remote indirect exciton systems based on acoustic transport. *Physical Review B*, 89(8):085313, 2014.

[9] Ran Finkelstein, Kobi Cohen, Benoit Jouault, Ken West, Loren N Pfeiffer, Masha Vladimirova, and Ronen Rapaport. Transition from spin-orbit to hyperfine interaction dominated spin relaxation in a cold fluid of dipolar excitons. *Physical Review B*, 96(8):085404, 2017.

[10] Alexander A. High, Jason R. Leonard, Aaron T. Hammack, Michael M. Fogler, Leonid V. Butov, Alexey V. Kavokin, Kenneth L. Campman, and Arthur C. Gossard. Spontaneous coherence in a cold exciton gas. *Nature*, 483(7391):584, 2012.

[11] CJ Dorow, JR Leonard, MM Fogler, LV Butov, KW West, and LN Pfeiffer. Split-gate device for indirect excitons. *Applied Physics Letters*, 112(18):183501, 2018.

[12] D. A. Wharam, Trevor John Thornton, R. Newbury, M. Pepper, H. Ahmed, J. E. F. Frost, D. G. Hasko, D. C. Peacock, D. A. Ritchie, and G. A. C. Jones. One-dimensional transport and the quantisation of the ballistic resistance. *Journal of Physics C: Solid State Physics*, 21(8):L209, 1988.

[13] BJ Van Wees, H Van Houten, CWJ Beenakker, J Gr Williamson, LP Kouwenhoven, D Van der Marel, and CT Foxon. Quantized conductance of point contacts in a two-dimensional electron gas. *Physical Review Letters*, 60(9):848, 1988.

[14] Adam Micolich. Double or nothing? *Nature Physics*, 9:530–531, 2013.

[15] MA Topinka, BJ LeRoy, SEJ Shaw, EJ Heller, RM Westervelt, KD Maranowski, and AC Gossard. Imaging coherent electron flow from a quantum point contact. *Science*, 289(5488):2323–2326, 2000.

[16] Sebastian Krinner, David Stadler, Dominik Husmann, Jean-Philippe Brantut, and Tilman Esslinger. Observation of quantized conductance in neutral matter. *Nature*, 517(7532):64, 2015.

[17] Keith Schwab, EA Henriksen, JM Worlock, and Michael L Roukes. Measurement of the quantum of thermal conductance. *Nature*, 404(6781):974, 2000.

[18] B. Gotsmann and M. A. Lantz. Quantized thermal transport across contacts of rough surfaces. *Nature Materials*, 12(1):59, 2013.

[19] Longji Cui, Wonho Jeong, Sunghoon Hur, Manuel Matt, Jan C Klöckner, Fabian Pauly, Peter Nielaba, Juan Carlos Cuevas, Edgar Meyhofer, and Pramod Reddy. Quantized thermal transport in single-atom junctions. *Science*, 355(6330):1192–1195, 2017.

[20] M. Büttiker, Y. Imry, R. Landauer, and S. Pinhas. Generalized many-channel conductance formula with application to small rings. *Physical Review B*, 31:6207–6215, 1985.

[21] DJ Papoular, LP Pitaevskii, and S Stringari. Quantized conductance through the quantum evaporation of bosonic atoms. *Physical Review A*, 94(2):023622, 2016.

[22] Sebastian Krinner, Martin Lebrat, Dominik Husmann, Charles Grenier, Jean-Philippe Brantut, and Tilman Esslinger. Mapping out spin and particle conductances in a quantum point contact. *Proceedings of the National Academy of Sciences*, 113(29):8144–8149, 2016.

[23] M. Kanász-Nagy, L. Glazman, T. Esslinger, and E. A. Demler. Anomalous conductances in an ultracold quantum wire. *Phys. Rev. Lett.*, 117:255302, Dec 2016.

[24] Shun Uchino and Masahito Ueda. Anomalous transport in the superfluid fluctuation regime. *Phys. Rev. Lett.*, 118:105303, Mar 2017.

[25] Boyang Liu, Hui Zhai, and Shizhong Zhang. Anomalous conductance of a strongly interacting fermi gas through a quantum point contact. *Phys. Rev. A*, 95:013623, Jan 2017.

[26] Simone Latini, Kirsten T. Winther, Thomas Olsen, and Kristian S. Thygesen. Interlayer excitons and band alignment in MoS_2/hBN/WSe_2 van der Waals heterostructures. *Nano Letters*, 17:938–945, 2017.

[27] M. H. Szymanska and P. B. Littlewood. Excitonic binding in coupled quantum wells. *Physical Review B*, 67:193305, 2003.

[28] K. Sivalertporn, L. Mouchliadis, A. L. Ivanov, R. Philp, and E. A. Muljarov. Direct and indirect excitons in semiconductor coupled quantum wells in an applied electric field. *Physical Review B*, 85:045207, 2012.

[29] Federico Grasselli, Andrea Bertoni, and Guido Goldoni. Exact two-body quantum dynamics of an electron-hole pair in semiconductor coupled quantum wells: A time-dependent approach. *Physical Review B*, 93:195310, 2016.

[30] Maxim Yu. Kharitonov and Konstantin B. Efetov. Electron screening and excitonic condensation in double-layer graphene systems. *Phys. Rev. B*, 78:241401, Dec 2008.

[31] M. Remeika, J. R. Leonard, C. J. Dorow, M. M. Fogler, L. V. Butov, M. Hanson, and A. C. Gossard. Measurement of exciton correlations using electrostatic lattices. *Phys. Rev. B*, 92:115311, Sep 2015.

[32] A. L. Ivanov, P. B. Littlewood, and H. Haug. Bose-einstein statistics in thermalization and photoluminescence of quantum-well excitons. *Phys. Rev. B*, 59:5032–5048, Feb 1999.

[33] T. Usuki, M. Saito, M. Takatsu, R. A. Kiehl, and N. Yokoyama. Numerical analysis of ballistic-electron transport in magnetic fields by using a quantum point contact and a quantum wire. *Physical Review B*, 52:8244–8255, 1995.

[34] Yu. Kagan, E. L. Surkov, and G. V. Shlyapnikov. Evolution of a bose-condensed gas under variations of the confining potential. *Physical Review A*, 54(3):R1753, 1996.

[35] Y Castin and R Dum. Bose-einstein condensates in time dependent traps. *Physical Review Letters*, 77(27):5315, 1996.

[36] L. Rayleigh. XXV. On copying diffraction gratings and some phenomena connected therewith. *Phil. Mag.*, 11:196–205, 1881.

[37] Thomas Juffmann, Hendrik Ulbricht, and Markus Arndt. Experimental methods of molecular matter-wave optics. *Rep. Prog. Phys.*, 76(8):086402, 2013.

[38] C. Kohstall, S. Riedl, E. R. Sánchez Guajardo, L. A. Sidorenkov, J. H. Denschlag, and R. Grimm. Observation of interference between two molecular bose-einstein condensates. *New J. Phys.*, 13:065027, 2011.

[39] Florian Meier and Daniel Loss. Magnetization transport and quantized spin conductance. *Physical Review Letters*, 90:167204, 2003.

[40] Chao Xu, Jason R Leonard, Chelsey J Dorow, Leonid V Butov, Michael M Fogler, Dmitri E Nikonov, and Ian A Young. Exciton gas transport through nanoconstrictions. *Nano letters*, 19(8):5373–5379, 2019.

[41] T. Usuki, M. Takatsu, R. A. Kiehl, and N. Yokoyama. Numerical analysis of electron-wave detection by a wedge-shaped point contact. *Physical Review B*, 50(11):7615, 1994.

[42] Mike H Anderson, Jason R Ensher, Michael R Matthews, Carl E Wieman, and Eric A Cornell. Observation of bose-einstein condensation in a dilute atomic vapor. *science*, pages 198–201, 1995.

[43] Cl C Bradley, CA Sackett, JJ Tollett, and Randall G Hulet. Evidence of bose-einstein condensation in an atomic gas with attractive interactions. *Physical review letters*, 75(9):1687, 1995.

[44] Kendall B Davis, M-O Mewes, Michael R Andrews, Nicolaas J van Druten, Dallin S Durfee, DM Kurn, and Wolfgang Ketterle. Bose-einstein condensation in a gas of sodium atoms. *Physical review letters*, 75(22):3969, 1995.

[45] Eugene P Gross. Structure of a quantized vortex in boson systems. *Il Nuovo Cimento (1955-1965)*, 20(3):454–477, 1961.

[46] LP Pitaevskii. Vortex lines in an imperfect bose gas. *Sov. Phys. JETP*, 13(2):451–454, 1961.

[47] F Dalfovo, C Minniti, and LP Pitaevskii. Frequency shift and mode coupling in the nonlinear dynamics of a bose-condensed gas. *Physical Review A*, 56(6):4855, 1997.

[48] Franco Dalfovo, Stefano Giorgini, Lev P Pitaevskii, and Sandro Stringari. Theory of bose-einstein condensation in trapped gases. *Reviews of Modern Physics*, 71(3):463, 1999.

[49] A Shabat and V Zakharov. Exact theory of two-dimensional self-focusing and one-dimensional self-modulation of waves in nonlinear media. *Soviet physics JETP*, 34(1):62, 1972.

[50] VE Zakharov and AB Shabat. Interaction between solitons in a stable medium. *Sov. Phys. JETP*, 37(5):823–828, 1973.

[51] SV Manakov. Nonlinear fraunhofer diffraction. *Zh. Eksp. Teor. Fiz*, 65(4):10, 1973.

[52] VE Zakharov and SV Manakov. Asymptotic behavior of non-linear wave systems integrated by the inverse scattering method. *Soviet Journal of Experimental and Theoretical Physics*, 44:106, 1976.

[53] Harvey Segur and Mark J Ablowitz. Asymptotic solutions and conservation laws for the nonlinear schrödinger equation. i. *Journal of Mathematical Physics*, 17(5):710–713, 1976.

[54] Harvey Segur. Asymptotic solutions and conservation laws for the nonlinear schrödinger equation. ii. *Journal of Mathematical Physics*, 17(5):714–716, 1976.

[55] PA Deift and Xin Zhou. Long-time asymptotics for integrable systems. higher order theory. *Communications in Mathematical Physics*, 165(1):175–191, 1994.

[56] Wu-Ming Liu, Biao Wu, and Qian Niu. Nonlinear effects in interference of bose-einstein condensates. *Physical review letters*, 84(11):2294, 2000.

[57] Stefan Burger, Kai Bongs, Stefanie Dettmer, Wolfgang Ertmer, Klaus Sengstock, Anna Sanpera, Gora V Shlyapnikov, and Maciej Lewenstein. Dark solitons in bose-einstein condensates. *Physical Review Letters*, 83(25):5198, 1999.

[58] LV Butov, AL Ivanov, A Imamoglu, PB Littlewood, AA Shashkin, VT Dolgopolov, KL Campman, and AC Gossard. Stimulated scattering of indirect excitons in coupled quantum wells: Signature of a degenerate bose-gas of excitons. *Physical Review Letters*, 86(24):5608, 2001.

[59] CJ Dorow, MW Hasling, DJ Choksy, JR Leonard, LV Butov, KW West, and LN Pfeiffer. High-mobility indirect excitons in wide single quantum well. *arXiv preprint arXiv:1810.01057*, 2018.

[60] GE Astrakharchik, J Boronat, IL Kurbakov, and Yu E Lozovik. Quantum phase transition in a two-dimensional system of dipoles. *Physical review letters*, 98(6):060405, 2007.

[61] H. P. Büchler, E. Demler, M. Lukin, A. Micheli, N. Prokof'ev, G. Pupillo, and P. Zoller. Strongly correlated 2d quantum phases with cold polar molecules: Controlling the shape of the interaction potential. *Phys. Rev. Lett.*, 98:060404, Feb 2007.

[62] Christophe Mora, Olivier Parcollet, and Xavier Waintal. Quantum melting of a crystal of dipolar bosons. *Phys. Rev. B*, 76:064511, Aug 2007.

[63] DCE Bortolotti, S Ronen, JL Bohn, and D Blume. Scattering length instability in dipolar bose-einstein condensates. *Physical review letters*, 97(16):160402, 2006.

[64] GE Astrakharchik, J Boronat, J Casulleras, IL Kurbakov, and Yu E Lozovik. Equation of state of a weakly interacting two-dimensional bose gas studied at zero temperature by means of quantum monte carlo methods. *Physical Review A*, 79(5):051602, 2009.

[65] Diana Hufnagl, R Kaltseis, Vesa Apaja, and RE Zillich. Roton-roton crossover in strongly correlated dipolar bose-einstein condensates. *Physical review letters*, 107(6):065303, 2011.

[66] Saeed H Abedinpour, Reza Asgari, and Marco Polini. Theory of correlations in strongly interacting fluids of two-dimensional dipolar bosons. *Physical Review A*, 86(4):043601, 2012.

[67] A Macia, D Hufnagl, F Mazzanti, J Boronat, and RE Zillich. Excitations and stripe phase formation in a two-dimensional dipolar bose gas with tilted polarization. *Physical review letters*, 109(23):235307, 2012.

[68] A Macia, J Boronat, and F Mazzanti. Phase diagram of dipolar bosons in two dimensions with tilted polarization. *Physical Review A*, 90(6):061601, 2014.

[69] S De Palo, F Rapisarda, and Gaetano Senatore. Excitonic condensation in a symmetric electron-hole bilayer. *Physical review letters*, 88(20):206401, 2002.

[70] MYJ Tan, ND Drummond, and RJ Needs. Exciton and biexciton energies in bilayer systems. *Physical Review B*, 71(3):033303, 2005.

[71] R. M. Lee, N. D. Drummond, and R. J. Needs. Exciton-exciton interaction and biexciton formation in bilayer systems. *Phys. Rev. B*, 79:125308, Mar 2009.

[72] Ryo Maezono, Pablo López Ríos, Tetsuo Ogawa, and Richard J Needs. Excitons and biexcitons in symmetric electron-hole bilayers. *Physical review letters*, 110(21):216407, 2013.

[73] Colin Hubert, Yifat Baruchi, Yotam Mazuz-Harpaz, Kobi Cohen, Klaus Biermann, Mikhail Lemeshko, Ken West, Loren Pfeiffer, Ronen Rapaport, and Paulo Santos. Attractive dipolar coupling between stacked exciton fluids. *Physical Review X*, 9(2):021026, 2019.

[74] DJ Choksy, Chao Xu, MM Fogler, LV Butov, Justin Norman, and AC Gossard. Attractive and repulsive dipolar interaction in bilayers of indirect excitons. *Physical Review B*, 103(4):045126, 2021.

[75] A Macia, GE Astrakharchik, F Mazzanti, Stefano Giorgini, and J Boronat. Single-particle versus pair superfluidity in a bilayer system of dipolar bosons. *Physical Review A*, 90(4):043623, 2014.

[76] Alexey Filinov. Correlation effects and collective excitations in bosonic bilayers: Role of quantum statistics, superfluidity, and the dimerization transition. *Physical Review A*, 94(1):013603, 2016.

[77] Fabio Cinti, Daw-Wei Wang, and Massimo Boninsegni. Phases of dipolar bosons in a bilayer geometry. *Physical Review A*, 95(2):023622, 2017.

[78] E Akaturk, Saeed H Abedinpour, and Bilal Tanatar. Density-wave instability and collective modes in a bilayer system of antiparallel dipoles. *Journal of Physics Communications*, 2(1):015018, 2018.

[79] Diana Hufnagl and Robert E Zillich. Stability and excitations of a bilayer of strongly correlated dipolar bosons. *Physical Review A*, 87(3):033624, 2013.

[80] Piyush Jain and Massimo Boninsegni. Quantum demixing in binary mixtures of dipolar bosons. *Physical Review A*, 83(2):023602, 2011.

[81] G Guijarro, GE Astrakharchik, J Boronat, B Bazak, and DS Petrov. Few-body bound states of two-dimensional bosons. *Physical Review A*, 101(4):041602, 2020.

[82] S Utsunomiya, L Tian, G Roumpos, CW Lai, N Kumada, T Fujisawa, M Kuwata-Gonokami, A Löffler, S Höfling, A Forchel, et al. Observation of bogoliubov excitations in exciton-polariton condensates. *Nature Physics*, 4(9):700–705, 2008.

[83] AA High, AT Hammack, LV Butov, L Mouchliadis, AL Ivanov, M Hanson, and AC Gossard. Indirect excitons in elevated traps. *Nano letters*, 9(5):2094–2098, 2009.

[84] AA High, AK Thomas, G Grosso, M Remeika, AT Hammack, AD Meyertholen, MM Fogler, LV Butov, M Hanson, and AC Gossard. Trapping indirect excitons in a gaas quantum-well structure with a diamond-shaped electrostatic trap. *Physical review letters*, 103(8):087403, 2009.

[85] YY Kuznetsova, AA High, and LV Butov. Control of excitons by laterally modulated electrode density. *Applied Physics Letters*, 97(20):201106, 2010.

[86] Tapash Chakraborty. Structure of binary boson mixtures at t= 0 k. *Physical Review B*, 26(11):6131, 1982.

[87] Catherine Kallin and John Berlinsky. Chiral superconductors. *Reports on Progress in Physics*, 79(5):054502, 2016.

[88] Nicholas Read and Dmitry Green. Paired states of fermions in two dimensions with breaking of parity and time-reversal symmetries and the fractional quantum hall effect. *Physical Review B*, 61(15):10267, 2000.

[89] Sankar Das Sarma, Chetan Nayak, and Sumanta Tewari. Proposal to stabilize and detect half-quantum vortices in strontium ruthenate thin films: Non-abelian braiding statistics of vortices in a p x+ i p y superconductor. *Physical Review B*, 73(22):220502, 2006.

[90] Liang Fu and C. L. Kane. Superconducting proximity effect and majorana fermions at the surface of a topological insulator. *Phys. Rev. Lett.*, 100:096407, Mar 2008.

[91] Jay D Sau, Roman M Lutchyn, Sumanta Tewari, and S Das Sarma. Generic new platform for topological quantum computation using semiconductor heterostructures. *Physical review letters*, 104(4):040502, 2010.

[92] Jeffrey CY Teo and Charles L Kane. Majorana fermions and non-abelian statistics in three dimensions. *Physical review letters*, 104(4):046401, 2010.

[93] Rui Yu, Wei Zhang, Hai-Jun Zhang, Shou-Cheng Zhang, Xi Dai, and Zhong Fang. Quantized anomalous hall effect in magnetic topological insulators. *Science*, 329(5987):61–64, 2010.

[94] Xiao-Liang Qi, Taylor L Hughes, and Shou-Cheng Zhang. Chiral topological superconductor from the quantum hall state. *Physical Review B*, 82(18):184516, 2010.

[95] Suk Bum Chung, Xiao-Liang Qi, Joseph Maciejko, and Shou-Cheng Zhang. Conductance and noise signatures of majorana backscattering. *Physical Review B*, 83(10):100512, 2011.

[96] A Yu Kitaev. Fault-tolerant quantum computation by anyons. *Annals of Physics*, 303(1):2–30, 2003.

[97] Alexei Kitaev. Anyons in an exactly solved model and beyond. *Annals of Physics*, 321(1):2–111, 2006.

[98] Michael Stone and Suk-Bum Chung. Fusion rules and vortices in $p_x + ip_y$ superconductors. *Phys. Rev. B*, 73:014505, Jan 2006.

[99] Jason Alicea, Yuval Oreg, Gil Refael, Felix Von Oppen, and Matthew PA Fisher. Non-abelian statistics and topological quantum information processing in 1d wire networks. *Nature Physics*, 7(5):412–417, 2011.

[100] Bertrand I Halperin, Yuval Oreg, Ady Stern, Gil Refael, Jason Alicea, and Felix von Oppen. Adiabatic manipulations of majorana fermions in a three-dimensional network of quantum wires. *Physical Review B*, 85(14):144501, 2012.

[101] Y. Maeno, H. Hashimoto, K. Yoshida, S. Nishizaki, T. Fujita, J. G. Bednorz, and F. Lichtenberg. Superconductivity in a layered perovskite without copper. *Nature*, 372:532 EP –, 12 1994.

[102] Andrew Peter Mackenzie and Yoshiteru Maeno. The superconductivity of sr_2ruo_4 and the physics of spin-triplet pairing. *Rev. Mod. Phys.*, 75:657–712, May 2003.

[103] Yoshiteru Maeno, Shunichiro Kittaka, Takuji Nomura, Shingo Yonezawa, and Kenji Ishida. Evaluation of spin-triplet superconductivity in sr2ruo4. *Journal of the Physical Society of Japan*, 81(1):011009, 2012.

[104] Ying Liu and Zhi-Qiang Mao. Unconventional superconductivity in sr 2 ruo 4. *Physica C: Superconductivity and its applications*, 514:339–353, 2015.

[105] Robert Joynt and Louis Taillefer. The superconducting phases of upt 3. *Reviews of Modern Physics*, 74(1):235, 2002.

[106] ER Schemm, WJ Gannon, CM Wishne, WP Halperin, and Aharon Kapitulnik. Observation of broken time-reversal symmetry in the heavy-fermion superconductor upt3. *Science*, 345(6193):190–193, 2014.

[107] JD Strand, Dale J Van Harlingen, JB Kycia, and William P Halperin. Evidence for complex superconducting order parameter symmetry in the low-temperature phase of upt 3 from josephson interferometry. *Physical review letters*, 103(19):197002, 2009.

[108] Keenan E Avers, William J Gannon, Stephen J Kuhn, William P Halperin, JA Sauls, L DeBeer-Schmitt, CD Dewhurst, Jorge Gavilano, Gergely Nagy, U Gasser, et al. Broken time-reversal symmetry in the topological superconductor upt 3. *Nature Physics*, 16(5):531–535, 2020.

[109] C Kallin and AJ Berlinsky. Is sr2ruo4 a chiral p-wave superconductor? *Journal of Physics: Condensed Matter*, 21(16):164210, 2009.

[110] Catherine Kallin. Chiral p-wave order in sr2ruo4. *Reports on Progress in Physics*, 75(4):042501, 2012.

[111] Andrew P Mackenzie, Thomas Scaffidi, Clifford W Hicks, and Yoshiteru Maeno. Even odder after twenty-three years: The superconducting order parameter puzzle of sr 2 ruo 4. *npj Quantum Materials*, 2(1):1–9, 2017.

[112] K. Ishida, H. Mukuda, Y. Kitaoka, K. Asayama, Z. Q. Mao, Y. Mori, and Y. Maeno. Spin-triplet superconductivity in sr2ruo4 identified by 17o knight shift. *Nature*, 396:658 EP –, 12 1998.

[113] J. A. Duffy, S. M. Hayden, Y. Maeno, Z. Mao, J. Kulda, and G. J. McIntyre. Polarized-neutron scattering study of the cooper-pair moment in sr_2ruo_4. *Phys. Rev. Lett.*, 85:5412–5415, Dec 2000.

[114] F. Laube, G. Goll, H. v. Löhneysen, M. Fogelström, and F. Lichtenberg. Spin-triplet superconductivity in sr_2ruo_4 probed by andreev reflection. *Phys. Rev. Lett.*, 84:1595–1598, Feb 2000.

[115] A. P. Mackenzie, R. K. W. Haselwimmer, A. W. Tyler, G. G. Lonzarich, Y. Mori, S. Nishizaki, and Y. Maeno. Extremely strong dependence of superconductivity on disorder in sr_2ruo_4. *Phys. Rev. Lett.*, 80:161–164, Jan 1998.

[116] G. M. Luke, Y. Fudamoto, K. M. Kojima, M. I. Larkin, J. Merrin, B. Nachumi, Y. J. Uemura, Y. Maeno, Z. Q. Mao, Y. Mori, H. Nakamura, and M. Sigrist. Time-reversal symmetry-breaking superconductivity in sr2ruo4. *Nature*, 394:558 EP –, 08 1998.

[117] KD Nelson, ZQ Mao, Y Maeno, and Y Liu. Odd-parity superconductivity in sr2ruo4. *Science*, 306(5699):1151–1154, 2004.

[118] Jing Xia, Yoshiteru Maeno, Peter T. Beyersdorf, M. M. Fejer, and Aharon Kapitulnik. High resolution polar kerr effect measurements of sr_2ruo_4: Evidence for broken time-reversal symmetry in the superconducting state. *Phys. Rev. Lett.*, 97:167002, Oct 2006.

[119] Francoise Kidwingira, JD Strand, DJ Van Harlingen, and Yoshiteru Maeno. Dynamical superconducting order parameter domains in sr2ruo4. *Science*, 314(5803):1267–1271, 2006.

[120] Andrej Pustogow, Yongkang Luo, Aaron Chronister, Y-S Su, DA Sokolov, Fabian Jerzembeck, Andrew Peter Mackenzie, Clifford William Hicks, Naoki Kikugawa, Srinivas Raghu, et al. Constraints on the superconducting order parameter in sr 2 ruo 4 from oxygen-17 nuclear magnetic resonance. *Nature*, 574(7776):72–75, 2019.

[121] GE Volovik. Quantized hall effect in superfluid helium-3 film. *Physics Letters A*, 128(5):277–279, 1988.

[122] GE Volovik and VM Yakovenko. Fractional charge, spin and statistics of solitons in superfluid 3he film. *Journal of Physics: Condensed Matter*, 1(31):5263, 1989.

[123] N. B. Kopnin and M. M. Salomaa. Mutual friction in superfluid ^{3}He: Effects of bound states in the vortex core. *Phys. Rev. B*, 44:9667–9677, Nov 1991.

[124] D. A. Ivanov. Non-abelian statistics of half-quantum vortices in p-wave superconductors. *Phys. Rev. Lett.*, 86:268–271, Jan 2001.

[125] Sumanta Tewari, S. Das Sarma, Chetan Nayak, Chuanwei Zhang, and P. Zoller. Quantum computation using vortices and majorana zero modes of a $p_x + ip_y$ superfluid of fermionic cold atoms. *Phys. Rev. Lett.*, 98:010506, Jan 2007.

[126] Chuanwei Zhang, Sumanta Tewari, Roman M. Lutchyn, and S. Das Sarma. $p_x + ip_y$ superfluid from s-wave interactions of fermionic cold atoms. *Phys. Rev. Lett.*, 101:160401, Oct 2008.

[127] Meng Cheng, Kai Sun, Victor Galitski, and S. Das Sarma. Stable topological superconductivity in a family of two-dimensional fermion models. *Phys. Rev. B*, 81:024504, Jan 2010.

[128] Xiao-Liang Qi, Taylor L. Hughes, S. Raghu, and Shou-Cheng Zhang. Time-reversal-invariant topological superconductors and superfluids in two and three dimensions. *Phys. Rev. Lett.*, 102:187001, May 2009.

[129] R. B. Laughlin. Magnetic induction of $d_{x^2-y^2} + \mathrm{id}_{\mathrm{xy}}$ order in high- T_c superconductors. *Phys. Rev. Lett.*, 80:5188–5191, Jun 1998.

[130] T. Senthil, J. B. Marston, and Matthew P. A. Fisher. Spin quantum hall effect in unconventional superconductors. *Phys. Rev. B*, 60:4245–4254, Aug 1999.

[131] Baruch Horovitz and Anatoly Golub. Superconductors with broken time-reversal symmetry: Spontaneous magnetization and quantum hall effects. *Phys. Rev. B*, 68:214503, Dec 2003.

[132] Yongjin Jiang, Dao-Xin Yao, Erica W. Carlson, Han-Dong Chen, and JiangPing Hu. Andreev conductance in the $d+id^{'}$-wave superconducting states of graphene. *Phys. Rev. B*, 77:235420, Jun 2008.

[133] Masatoshi Sato, Yoshiro Takahashi, and Satoshi Fujimoto. Non-abelian topological orders and majorana fermions in spin-singlet superconductors. *Phys. Rev. B*, 82:134521, Oct 2010.

[134] Annica M. Black-Schaffer. Edge properties and majorana fermions in the proposed chiral d-wave superconducting state of doped graphene. *Phys. Rev. Lett.*, 109:197001, Nov 2012.

[135] Rahul Nandkishore, L. S. Levitov, and A. V. Chubukov. Chiral superconductivity from repulsive interactions in doped graphene. *Nature Physics*, 8:158 EP –, 01 2012.

[136] Wan-Sheng Wang, Yuan-Yuan Xiang, Qiang-Hua Wang, Fa Wang, Fan Yang, and Dung-Hai Lee. Functional renormalization group and variational monte carlo studies of the electronic instabilities in graphene near $\frac{1}{4}$ doping. *Phys. Rev. B*, 85:035414, Jan 2012.

[137] Maximilian L. Kiesel, Christian Platt, Werner Hanke, and Ronny Thomale. Model evidence of an anisotropic chiral $d+id$-wave pairing state for the water-intercalated $\mathrm{na}_x\mathrm{coo}_2 \cdot y\mathbf{h}_2\mathbf{O}$ superconductor. *Phys. Rev. Lett.*, 111:097001, Aug 2013.

[138] Feng Liu, Cheng-Cheng Liu, Kehui Wu, Fan Yang, and Yugui Yao. $d+id^{'}$ chiral superconductivity in bilayer silicene. *Phys. Rev. Lett.*, 111:066804, Aug 2013.

[139] Annica M Black-Schaffer and Carsten Honerkamp. Chiral d-wave superconductivity in doped graphene. *Journal of Physics: Condensed Matter*, 26(42):423201, 2014.

[140] Cheng-Cheng Liu, Li-Da Zhang, Wei-Qiang Chen, and Fan Yang. Chiral spin density wave and d+ i d superconductivity in the magic-angle-twisted bilayer graphene. *Physical review letters*, 121(21):217001, 2018.

[141] Dante M Kennes, Johannes Lischner, and Christoph Karrasch. Strong correlations and d+ id superconductivity in twisted bilayer graphene. *Physical Review B*, 98(24):241407, 2018.

[142] Zhesen Yang, Shengshan Qin, Qiang Zhang, Chen Fang, and Jiangping Hu. π/2-josephson junction as a topological superconductor. *Physical Review B*, 98(10):104515, 2018.

[143] Tongyun Huang, Lufeng Zhang, and Tianxing Ma. Antiferromagnetically ordered mott insulator and d+ id superconductivity in twisted bilayer graphene: A quantum monte carlo study. *Science Bulletin*, 64(5):310–314, 2019.

[144] Congjun Wu and JE Hirsch. Mixed triplet and singlet pairing in ultracold multicomponent fermion systems with dipolar interactions. *Physical Review B*, 81(2):020508, 2010.

[145] Yuxuan Wang and Andrey Chubukov. Charge-density-wave order with momentum $(2q,0)$ and $(0,2q)$ within the spin-fermion model: Continuous and discrete symmetry breaking, preemptive composite order, and relation to pseudogap in hole-doped cuprates. *Phys. Rev. B*, 90:035149, Jul 2014.

[146] Yuxuan Wang and Liang Fu. Topological phase transitions in multicomponent superconductors. *Phys. Rev. Lett.*, 119:187003, Nov 2017.

[147] Wang Yang, Chao Xu, and Congjun Wu. Single branch of chiral majorana modes from doubly degenerate fermi surfaces. *Physical Review Research*, 2(4):042047, 2020.

[148] Wei-Cheng Lee, Shou-Cheng Zhang, and Congjun Wu. Pairing state with a time-reversal symmetry breaking in feas-based superconductors. *Phys. Rev. Lett.*, 102:217002, May 2009.

[149] Lun-Hui Hu, PD Johnson, and Congjun Wu. Pairing symmetry and topological surface state in iron-chalcogenide superconductors. *Physical Review Research*, 2(2):022021, 2020.

[150] Ronny Thomale, Christian Platt, Werner Hanke, and B. Andrei Bernevig. Mechanism for explaining differences in the order parameters of feas-based and fep-based pnictide superconductors. *Phys. Rev. Lett.*, 106:187003, May 2011.

[151] Christian Platt, Ronny Thomale, Carsten Honerkamp, Shou-Cheng Zhang, and Werner Hanke. Mechanism for a pairing state with time-reversal symmetry breaking in iron-based superconductors. *Phys. Rev. B*, 85:180502, May 2012.

[152] M. Khodas and A. V. Chubukov. Interpocket pairing and gap symmetry in fe-based superconductors with only electron pockets. *Phys. Rev. Lett.*, 108:247003, Jun 2012.

[153] Rafael M. Fernandes and Andrew J. Millis. Nematicity as a probe of superconducting pairing in iron-based superconductors. *Phys. Rev. Lett.*, 111:127001, Sep 2013.

[154] Alberto Hinojosa, Rafael M. Fernandes, and Andrey V. Chubukov. Time-reversal symmetry breaking superconductivity in the coexistence phase with magnetism in fe pnictides. *Phys. Rev. Lett.*, 113:167001, Oct 2014.

[155] Shi-Zeng Lin, Saurabh Maiti, and Andrey Chubukov. Distinguishing between $s+id$ and $s+is$ pairing symmetries in multiband superconductors through spontaneous magnetization pattern induced by a defect. *Phys. Rev. B*, 94:064519, Aug 2016.

[156] Valentin Stanev and Zlatko Tešanović. Three-band superconductivity and the order parameter that breaks time-reversal symmetry. *Phys. Rev. B*, 81:134522, Apr 2010.

[157] Shi-Zeng Lin and Xiao Hu. Massless leggett mode in three-band superconductors with time-reversal-symmetry breaking. *Phys. Rev. Lett.*, 108:177005, Apr 2012.

[158] M. Marciani, L. Fanfarillo, C. Castellani, and L. Benfatto. Leggett modes in iron-based superconductors as a probe of time-reversal symmetry breaking. *Phys. Rev. B*, 88:214508, Dec 2013.

[159] Saurabh Maiti and Andrey V. Chubukov. $s+is$ state with broken time-reversal symmetry in fe-based superconductors. *Phys. Rev. B*, 87:144511, Apr 2013.

[160] F. Ahn, I. Eremin, J. Knolle, V. B. Zabolotnyy, S. V. Borisenko, B. Büchner, and A. V. Chubukov. Superconductivity from repulsion in lifeas: Novel s-wave symmetry and potential time-reversal symmetry breaking. *Phys. Rev. B*, 89:144513, Apr 2014.

[161] Julien Garaud and Egor Babaev. Domain walls and their experimental signatures in $s+is$ superconductors. *Phys. Rev. Lett.*, 112:017003, Jan 2014.

[162] Saurabh Maiti, Manfred Sigrist, and Andrey Chubukov. Spontaneous currents in a superconductor with $s+is$ symmetry. *Phys. Rev. B*, 91:161102, Apr 2015.

[163] Julien Garaud, Johan Carlström, and Egor Babaev. Topological solitons in three-band superconductors with broken time reversal symmetry. *Physical review letters*, 107(19):197001, 2011.

[164] Julien Garaud, Johan Carlström, Egor Babaev, and Martin Speight. Chiral c p 2 skyrmions in three-band superconductors. *Physical Review B*, 87(1):014507, 2013.

[165] Shi-Zeng Lin. Ground state, collective mode, phase soliton and vortex in multiband superconductors. *Journal of Physics: Condensed Matter*, 26(49):493202, 2014.

[166] Chao Xu, Wang Yang, and Congjun Wu. Superconducting junction with tri-component gap functions. *arXiv preprint arXiv:2010.05362*, 2020.

[167] Anthony J Leggett. A theoretical description of the new phases of liquid he 3. *Reviews of Modern Physics*, 47(2):331, 1975.

[168] Dieter Vollhardt and Peter Wolfle. *The superfluid phases of helium 3*. Courier Corporation, 2013.

[169] Grigory E Volovik. *The universe in a helium droplet*, volume 117. Oxford University Press on Demand, 2003.

[170] Anthony James Leggett et al. *Quantum liquids: Bose condensation and Cooper pairing in condensed-matter systems*. Oxford university press, 2006.

[171] M Zahid Hasan and Charles L Kane. Colloquium: topological insulators. *Reviews of modern physics*, 82(4):3045, 2010.

[172] Xiao-Liang Qi and Shou-Cheng Zhang. Topological insulators and superconductors. *Reviews of Modern Physics*, 83(4):1057, 2011.

[173] Yoichi Ando and Liang Fu. Topological crystalline insulators and topological superconductors: From concepts to materials. *Annu. Rev. Condens. Matter Phys.*, 6(1):361–381, 2015.

[174] Masatoshi Sato and Satoshi Fujimoto. Majorana fermions and topology in superconductors. *Journal of the Physical Society of Japan*, 85(7):072001, 2016.

[175] Ching-Kai Chiu, Jeffrey CY Teo, Andreas P Schnyder, and Shinsei Ryu. Classification of topological quantum matter with symmetries. *Reviews of Modern Physics*, 88(3):035005, 2016.

[176] Masatoshi Sato and Yoichi Ando. Topological superconductors: a review. *Reports on Progress in Physics*, 80(7):076501, 2017.

[177] Yi Li, Da Wang, and Congjun Wu. Spontaneous breaking of time-reversal symmetry in the orbital channel for the boundary majorana flat bands. *New Journal of Physics*, 15(8):085002, 2013.

[178] Shinsei Ryu, Joel E Moore, and Andreas WW Ludwig. Electromagnetic and gravitational responses and anomalies in topological insulators and superconductors. *Physical Review B*, 85(4):045104, 2012.

[179] Xiao-Liang Qi, Edward Witten, and Shou-Cheng Zhang. Axion topological field theory of topological superconductors. *Physical Review B*, 87(13):134519, 2013.

[180] Zhong Wang, Xiao-Liang Qi, and Shou-Cheng Zhang. Topological field theory and thermal responses of interacting topological superconductors. *Physical Review B*, 84(1):014527, 2011.

[181] Michael Stone. Gravitational anomalies and thermal hall effect in topological insulators. *Physical Review B*, 85(18):184503, 2012.

[182] Bitan Roy. Higher-order topological superconductors in p-, t-odd quadrupolar dirac materials. *Physical Review B*, 101(22):220506, 2020.

[183] Tian Shang, Michael Smidman, Saikat K Ghosh, Christopher Baines, Lieh-Jeng Chang, DJ Gawryluk, Joel AT Barker, Ravi P Singh, D McK Paul, Geetha Balakrishnan, et al. Time-reversal symmetry breaking in re-based superconductors. *Physical review letters*, 121(25):257002, 2018.

[184] Shyam Sundar, S Salem-Sugui, MK Chattopadhyay, SB Roy, LS Sharath Chandra, LF Cohen, and L Ghivelder. Study of nb0. 18re0. 82 non-centrosymmetric superconductor in the normal and superconducting states. *Superconductor Science and Technology*, 32(5):055003, 2019.

[185] Roberto D Peccei and Helen R Quinn. Cp conservation in the presence of pseudoparticles. *Physical Review Letters*, 38(25):1440, 1977.

[186] Steven Weinberg. A new light boson? *Physical Review Letters*, 40(4):223, 1978.

[187] Frank Wilczek. Problem of strong p and t invariance in the presence of instantons. *Physical Review Letters*, 40(5):279, 1978.

[188] Rundong Li, Jing Wang, Xiao-Liang Qi, and Shou-Cheng Zhang. Dynamical axion field in topological magnetic insulators. *Nature Physics*, 6(4):284–288, 2010.

[189] Pallab Goswami and Bitan Roy. Axionic superconductivity in three-dimensional doped narrow-gap semiconductors. *Physical Review B*, 90(4):041301, 2014.

[190] Michael Stone et al. Effective action and electromagnetic response of topological superconductors and majorana-mass weyl fermions. *Physical Review B*, 93(17):174501, 2016.

[191] Antti Juhani Niemi and Gordon W Semenoff. Fermion number fractionization in quantum field theory. *Physics Reports*, 135(3):99–193, 1986.

[192] Alexander Altland and Ben D Simons. *Condensed matter field theory*. Cambridge university press, 2010.